METHANE ENVIRONMENT AROUND COLD SEEPS –

EXAMPLES FROM ANTARCTICA AND THE MEDITERRANEAN

Dissertation

zur Erlangung des

Doktorgrades der Naturwissenschaften

-Dr. rer. nat.-

am Fachbereich Geowissenschaften

der Universität Bremen

Vorgelegt von

Patrizia Geprägs

Bremen, Februar 2016

Gutachter/Reviewer

Prof. Dr. Gerhard Bohrmann

University of Bremen

MARUM - Centre for Marine Environmental Sciences

Klagenfurter Str.

28359 Bremen, Germany

Prof. Dr. Marta Torres

Oregon State University

College of Earth, Ocean, and Atmospheric Sciences

104 CEOAS Administration Building

Corvallis, OR 97331-5503

Weitere Mitglieder der Prüfungskommision/
Additional members of the examination board

Prof. Dr. Wolfgang Bach

PD. Dr. Sabine Kasten

Dr. Florence Schubotz

Nils Brückner

Tag des öffentlichen Kolloquiums/Day of public colloquium

01 June 2016

PREFACE

The present PhD thesis and the related research were conducted at the MARUM – Center for Marine Environmental Sciences and the University of Bremen, Germany. The work was financed through the DFG-Research Center/Cluster of Excellence "The Ocean in the Earth System" and further supported by a DAAD grant (57044996) "Kurzstipendium für Doktoranden".

Samples were collected during three research cruises. The thesis started in March 2013 with a research cruise on RV POLARSTERN (ANTXXIX-4) around South Georgia. After that cruise we decided to develop a new method to analyze methane in water samples. After two research stays in the USA at the Oregon State University (OSU) in Corvallis and at the School of Ocean and Earth Science and Technology (SOEST) in Hawaii and after a long phase of literature research, we finally opted for an instrument. It is a laser-based analyzer using Off-Axis Integrated Cavity Output Spectroscopy (ICOS) for methane analysis. Prof. Dr. Marta Torres (OSU) bought this instrument from Los Gatos Research Inc. financed by the U.S. Department of Energy Grant #DE-FE00135331. The instrument was shipped to Germany in April 2014 by the usage of a Carnet ATA, and thus, was available for one year. The method was developed and tested in the following six months and applied on two expeditions. The first expedition took place in November/December 2014 in the Mediterranean on RV METEOR (M112) and the next cruise in February/March 2015 on the same vessel in the Gulf of Mexico (M114). During both cruises (M112 and M114) the new method was successfully used and compared to the previous method. Another research stay at the OSU in Corvallis during November/December 2015 was used to perform final analyses for the thesis and to write a manuscript in cooperation with Marta Torres. This research stay was supported by the DAAD. Results of M112 and M114 were used for data collection with the new method reported in chapter 3. Chapter 4 includes the first case study about methane seepage in Antarctica and chapter 5 comprises the results from the second case study in the Mediterranean (M112) about methane distribution in the water column above an active mud volcano.

ABSTRACT

Marine cold seeps occur globally and represent unique pathways for material transport from depth. Methane is one of the major components which can be released at the seafloor into the overlying water column. The sediment-water methane flux can be described by two different transport mechanisms, diffusive flux and advective flux, the latter being mostly associated with gas bubbles. In sediments, diffusive fluxes of methane are often hampered by microbial anaerobic oxidation of methane (AOM), also termed the benthic filter. But if this benthic filter is limited or if stronger fluxes exceed the capacity of this filter, methane is released into the hydrosphere. Once methane reaches the hydrosphere it can be either transported by currents or diffusion, or it can be microbially oxidized. It is indeed known that methane released at cold seeps does not often reach the atmosphere. Yet, the processes in the water column that control the sink of methane are still poorly constrained. The goals of this thesis were multifold: 1) to develop a novel and enhanced method for rapid and accurate methane detection in water samples, 2) to investigate methane seepage at two sites. In South Georgia (Antarctica) the impact of methane seepage on the carbon cycle was investigated, while in the Mediterranean methane seepage was studied around an active mud volcano with a focus on comparatively evaluating advective versus diffusive methane input into the water column.

The need for a new method became apparent after the first case study in South Georgia. The currently used Vacuum-Extraction method revealed to be highly time-consuming and allowed only for a limited number of water samples to be processed. New laser-based instrumentation utilizing *Off-Axis Integrated Cavity Output Spectroscopy* (OA-ICOS) technology has been increasingly utilized for the continuous measurement of methane in air and surface seawater during the last years. We also decided to use this technology; however, our method was specially developed for the analysis of discrete water samples instead of continuous flow analysis. This extends the applicability of this method to deep-water samples. In comparison to conventional approaches the novel method provides faster results with almost no preparation time, a simple sampling technique and a rapid and accurate analysis of methane. Long-term storage of samples is not required, thereby eliminates the need for preservative chemicals.

The case study in South Georgia represents one of the first studies that geochemically investigate methane seepage at cold seeps in the Southern Ocean, Antarctica. This thesis reports on methane sources and potential sinks associated with methane seeps in Cumberland Bay, South Georgia's largest fjord system. Here, the biogenic methane most likely originated from peat-bearing sediments that are located several tens of meters below the seafloor. Although bubble emission sites were observed within the bay, only one of the sampled cores indicated upward advection; instead most of the methane was transported via diffusion. Sulfate and methane flux estimates in these sediments suggest that a large fraction of methane is consumed by AOM. Analyzed methane concentrations in pore water

were high, especially close to the seepage sites (~40 mM); but concentrations in the water column are relatively low (max. 58 nM) and have been observed only close to the seafloor. Methane thus appears to be trapped in the lowermost water mass, where measured microbial oxidation rates only revealed a very low activity. It is therefore inferred that methane must be transported out of the bay in the bottom water layer.

Methane concentrations in the second case study were successfully determined by the new method, thereby corroborating the utility and necessity of prior method development. At the Venere mud volcano (MV) in the Mediterranean hydroacoustic mapping was combined with bottom water sampling and the collection of gases at the seafloor in two contrasting settings: at gas seeps and above fresh extruded mud. The Venere MV is an active mud volcano in the Ionian Sea on the Calabrian Arc with a relatively recent mud flow on its southeastern flank. Active gas discharge was observed on repeated surveys for 31 days at five flare locations and most of them indicated a strong variability in intensity. Four of these flare sites were arranged along a circular structure around the mud volcano, with one weak bubble emission site located in the vicinity of the summit. In particular bottom water samples collected 0.5–2.0 meters above the seafloor were strongly enriched in methane with concentrations up to 566 µM. Yet 100 meters above the gas emissions sites most of the methane was gone; above the mud flow the concentrations decreased even faster. Since horizontal transportation of methane in the water column was not observed, methane oxidation seemed to be the major sink for methane. The advective input, estimated by direct gas collection at the most active flare site was clearly smaller than the vertical diffusive methane input from the mud flow. Compared to the case study in South Georgia, methane fluxes at Venere MV are much higher. However, high methane concentrations are also only observed close to the seafloor and methane did not reach surface waters.

This thesis provides insights into the behavior of methane around seep sites. Although the terminal sink of methane in both case studies was not explicitly determined, the available data showed how methane is distributed in the water column. Furthermore, new findings were made at the mud volcano about the impact of degassing mud, enabled by the new sampling method.

ZUSAMMENFASSUNG

Kalte Quelle treten weltweit am Meeresboden auf und stellen einzigartige Transportwege für unterschiedlichste Materialien aus der Tiefe dar. Methan ist dabei eines der wichtigsten und häufigsten Komponenten, die am Meeresboden freigesetzt werden können. Zwei unterschiedliche Transportmechanismen beschreiben diesen Methanfluss: advektiver Fluss, der oft mit Gasblasenaustritten verbunden wird, und diffusiver Fluss. Diffusive Flüsse werden in Sedimenten oft durch die anaerobe Methan Oxidation (AOM) behindert, deshalb wird dieser Prozess auch als benthischer Filter in den Sedimenten bezeichnet. Falls dieses Filtersystem nicht vorhanden ist, oder stärkere Methanflüsse die Kapazität des Filters überschreiten, dann gelangt Methan in die darüber liegende Wassersäule. Wenn es die Hydrosphäre erreicht hat kann es durch Strömungen oder Diffusion fort transportiert und/oder auch mikrobiell oxidiert werden. Zwar ist bekannt, dass Methan in den meisten Fällen nicht in die Atmosphäre gelangt, jedoch sind die Prozesse in der Wassersäule, welche den Verbleib von Methan beschreiben, immer noch spärlich beschrieben. Die Ziele dieser Doktorarbeit bestehen darin, die Verteilung und das Verhalten von Methan in der Wassersäule besser zu verstehen, indem: 1) eine neue Methode entwickelt wurde um Methan in Wasserproben schnell und genau zu analysieren, 2) Methanemissionen in Südgeorgien untersucht wurden und der dortige Einfluss von Methan auf den Kohlenstoffkreislauf und 3), indem Methanemissionen an einem Schlammvulkan im Mittelmeer untersucht wurden, mit einem Vergleich von diffusivem und advektivem Transport in die Wassersäule.

Dass eine neue Methode benötigt wird, wurde insbesondere nach der ersten Fallstudie in Südgeorgien deutlich. Die zurzeit gängige „Vakuum-Extraktions Methode“ ist sehr zeitaufwendig und ermöglicht deshalb nur die Analyse einer geringen Anzahl von Proben. Neue, auf Laser basierende Instrumente, welche die „*Off-Axis Integrated Cavitiy Output Spectroscopy (OA-ICOS) -Technologie*“ verwenden, werden zurzeit häufig angewendet um kontinuierliche Messungen von Luft oder Oberflächenwasser durchzuführen. Auch wir verwendeten diese Technologie, allerdings wurde die Methode so entwickelt, dass die Probe nicht im kontinuierlichen Durchfluss gemessen wird, sondern dass Einzelproben gemessen werden können. Dies erweitert das Anwendungsgebiet auf Tiefseeproben. Im Vergleich zu den konventionellen Methoden ermöglicht die neue Methode schnellere Ergebnisse mit sehr geringer Vorbereitungszeit und einer einfachen Beprobungsstrategie, sowie eine schnelle aber genaue Methananalytik. Eine Langzeitaufbewahrung der Proben ist bei dieser Methode nicht vorgesehen, was den Vorteil bringt, dass auf Konservierungsstoffe verzichtet werden kann.

Die erste Fallstudie der Doktorarbeit, durchgeführt in Südgeorgien, ist eine der ersten Arbeiten, die Methanemissionen an kalten Quellen in der Antarktis geochemisch untersucht. In dieser Arbeit wird von dem Ursprung und dem möglichen Verbleib von Methan im Zusammenhang mit Methanquellen in der Cumberland Bay, die größte Bucht in Südgeorgien, berichtet. Das biogene Methan stammt vermutlich aus torfhaltigen Sedimenten, welche in größerer Tiefe (mehrere 10er Meter) abgelagert wurden. Obwohl

Blasenaustritte innerhalb der Bucht beobachtet wurden, hat nur eine der untersuchten Stellen einen advektiven Methanfluss aufgewiesen. Ein Großteil des Methans wurde diffusiv transportiert. Berechnete Sulfat- und Methanflüsse wiesen darauf hin, dass das meiste Methan durch AOM in den Sedimenten gezehrt wurde. Im Porenwasser gemessene Methankonzentrationen sind hoch, insbesondere nahe den Gasaustrittstellen (~40 mM). Die gemessenen Konzentrationen in der Wassersäule sind dagegen relative gering (max. 58 nM) und wurden nur nah am Meeresgrund beobachtet. In dieser Bucht ist das Methan in der untersten von insgesamt drei Wasserschichten eingeschlossen, in der Methanoxidationsraten nur sehr geringe Aktivitäten aufzeigten. Deshalb nehmen wir an, dass das Methan in dem Bodenwasser aus der Bucht hinaus transportiert und verdünnt wurde.

Die Methankonzentrationen in der zweiten Fallstudie wurden erfolgreich anhand der neuen Methode bestimmt. Am Schlammvulkan „Venere“ wurden hydroakustischen Messungen mit der Beprobung von Bodenwasser und aufgefangenem Gas an zwei unterschiedlichen Stellen kombiniert: an Gasaustrittstellen und direkt über einem Schlammfluss. Der Venere Schlammvulkan befindet sich im Ionischen Meer am Kalabrischen Kontinentalrand; er ist aktiv und weist einen relativ jungen Schlammfluss auf. Aktive Gasaustritte wurden über 31 Tage beobachtet und zeigten eine hohe Variabilität in der Emissionsintensität. Vier von den fünf Gasaustritten sind entlang einer Kreisstruktur um den Schlammvulkan angeordnet, mit einer zusätzlichen Austrittstelle im Zentrum des Vulkans, in der Nähe des Gipfels. Zusätzlich dazu wurden mehrere Wasserproben über dem Schlamm genommen um den Methanaustritt des Schlammflusses zu bestimmen. Besonders die bodennahen Proben zeigten sehr hohe Methankonzentrationen mit bis zu 566 µM. Diese Methanwerte gingen jedoch in den ersten 100 m über dem Meeresboden stark zurück, über dem Schlammfluss reduzierten sich die Konzentrationen noch schneller. Die mikrobielle Oxidation von Methan war vermutlich der Grund für den starken Rückgang der Konzentrationen, da keine Anzeichen für einen Forttransport der Methananreicherungen zu finden waren. Der advektive Methaneintrag, gemessen an der aktivsten Gasaustrittstelle, ist deutlich geringer als der vertikale diffusive Eintrag durch den Schlammfluss. Trotz der viel höheren Gasflüsse im Vergleich zu Südgeorgien, ob diffusiv oder advektiv, bilden die Methankonzentrationen nur bodennah Anreicherungen aus und an beiden Lokationen erreicht das Methan kein Oberflächenwasser.

Diese Doktorarbeit gibt Einblicke in das Verhalten von Methan im Umfeld von Kalten Quellen. Die gewonnenen Daten zeigen, wie sich Methan in der Wassersäule verteilt, auch wenn nicht eindeutig geklärt werden konnte, wo genau der Verbleib von Methan war. Außerdem wurden neue Erkenntnisse über Schlammvulkane gewonnen und der Einfluss von entgasenden Schlammflüssen auf die umliegende Wassersäule wurde erkannt. Dies wurde zu einem großen Teil durch die neu entwickelte Methode zur schnelleren Bestimmung von Methan ermöglicht.

TABLE OF CONTENTS

OUTLINE AND CONTRIBUTION TO MANUSCRIPTS

This cumulative dissertation is structured in five main chapters, excluding the Preface, Abstract, Acknowledgements, References and Appendices. Chapter 1 gives an introduction into the main topics. The first part is about fluid discharge in general, the occurrence of cold seeps, the origin of the fluids and their way through the sediment and about the seepage at the seafloor. This is followed by a general description of mud volcanism and an introduction in mud volcanism in the Calabrian Arc. The second part of this chapter is about methane, its transport mechanism and biogeochemical processes in the sediment and the water column and, finally, about methane and its effects on the atmosphere. The first chapter is completed with the motivation for this work.

Chapter 2: New developed method: Rapid analysis of methane concentration in water samples using headspace equilibration and Off-Axis Integrated Cavity Output Spectroscopy (ICOS).

Patrizia Geprägs, Marta E. Torres, Timo Fleischmann, Susan Mau, Thomas Pape, Gerhard Bohrmann

Submitted in Limnology and Oceanography: Methods

The need for a new method turned out after case study 1 in Antarctica, where sampling was very limited due to the current time-consuming “Vacuum-Extraction” method. This chapter describes the new developed method to detect methane in discrete water samples. Furthermore, the previous method is explained and compared to the novel method, therefore, no separate methodology chapter was required.

P. Geprägs designed the project together with G. Bohrmann and M.E. Torres. P. Geprägs developed the method together with M.E. Torres with help from T. Fleischmann, data evaluation was supported by S. Mau and T. Pape. P.Geprägs wrote the manuscript with contributions from all co-authors.

Chapter 3: *Case study 1:* Carbon cycling fed by methane seepage at the shallow Cumberland Bay, South Georgia, Subantarctic.

Patrizia Geprägs, Marta E. Torres, Susan Mau, Sabine Kasten, Miriam Römer, Gerhard Bohrmann

Submitted in Geochemistry, Geophysics, Geosystems

This chapter includes the manuscript about seepage in the Cumberland Bay in South Georgia. Pore water and water column samples were geochemically analyzed to understand the carbon cycling in that region and to determine how much methane is transported into the water column and into the atmosphere. The water column samples are detected by the Vacuum-Extraction method.

P. Geprägs, M.E. Torres and G. Bohrmann designed the project. P. Geprägs sampled, analyzed and evaluated the data with contributions from S. Kasten, S. Mau, and M.E. Torres. The map and hydroacoustic data was provided by M. Römer. P. Geprägs wrote the manuscript with contributions from all co-authors.

Chapter 4: *Case study 2:* Methane in the water column above an active mud volcano in the Calabrian margin.

Patrizia Geprägs, Marta E. Torres, Miriam Römer, Thomas Pape, Paul Wintersteller, Gerhard Bohrmann

In preparation for Journal of Geophysical Research

This chapter includes the manuscript about methane distributions above the Venere mud volcano in the Calabrian Arc. Water column samples were collected in high resolution above flare locations and fresh extruded mud. The input of methane from both settings was investigated, as well as the fate of methane in the water column.

The project was designed by P. Geprägs, M.E. Torres and G. Bohrmann. P. Geprägs sampled the data with help from P. Wintersteller. Analyses were performed by P.G. with contributions from T. Pape and P. Wintersteller. The map and hydroacoustic data was provided by M. Römer. P. Geprägs wrote the manuscript with contributions from M.E.Torres.

Chapter 5 summarizes the main conclusions and remaining limitations of this work and provides suggestions for future studies. Figures and Tables are continuously numbered in this thesis. Equations are separately numbered in each chapter, because some of the equations are mentioned several times.

CHAPTER 1: INTRODUCTION

1.1 FLUID DISCHARGE AT THE SEAFLOOR: COLD SEEPS AND MUD VOLCANOES

1.1.1 General

Cold seeps display a unique pathway of material transfer by migration of liquids, gases and sediment material through the seabed into the water column [*Linke et al.*, 2010; *Suess*, 2014]. Marine cold seeps occur globally along continental margins; at active, passive and transform margins (Figure 1) [*Judd and Hovland*, 2007; *Suess*, 2014]. The main component in discharging fluids at cold seeps and mud volcanoes is methane, and thus, these features occur in areas with high organic matter input.

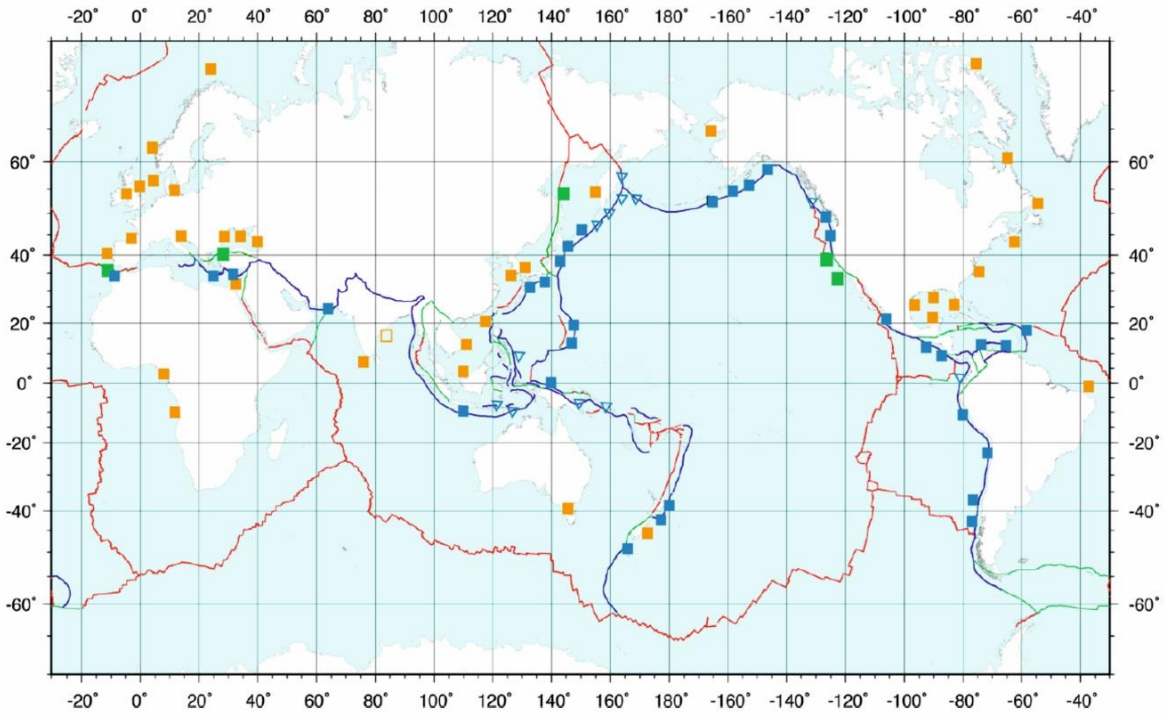

Figure 1: Global cold seeps. Seep locations with hydrocarbon–metazoan–microbe–carbonate characteristics; active margins sites (blue), passive margin sites (orange); sites at transform margins (green) [from *Suess*, 2014].

Primary productivity, as one of the main provider of organic matter in marine sediments, is mainly controlled by light, temperature and mineral nutrients, such as phosphate and nitrate, whereas productivity in coastal waters is on the average about twice as high as that in the open ocean [*Tissot and Welte*, 2013].

While high productivity rates are also found in intercontinental basins, upwelling areas in particular are amongst the most productive areas, which is where nutrient-rich water masses reach surface waters and primary productivity takes place [*Judd and Hovland*, 2007; *Tissot and Welte*, 2013].

The geologic setting plays an essential role on the seeps and affects characteristic such as lifespan, impact of surrounding sediments and biogeochemical environment [*Suess*, 2014]. At convergent margins, the oceanic plate loaded with sediments subducts underneath the less dense plate. Depending on whether sediments are accreted or eroded either an accretionary margin or erosive margin is formed, respectively. Sediment accretion forms ridges, which strike parallel to the trench axis and include faulted and folded sediments and thrust faults. Along margins with a steep subduction angle and an oceanic plate with a rough surface, the top-loaded sediments are not accreted, instead, the base of the overriding plate can be eroded [*von Huene and Scholl*, 1991; *Suess*, 2014]. These non-accretionary margins represent about 75% of the global active margin settings [*Scholl and Huene*, 2007]. At erosive margins only a small accretionary prism is formed and the margin of the overlying plate is heavily fractured or even destroyed (Figure 2). At both convergent settings, accretionary and erosive margin, subducted sediments dewater first due to temperature and pressure increase. Subsequently, at higher temperatures, between 60 and 150 °C, dehydration reactions such as opal A-CT or smectite to illite, lead to hydrofacturing and migration of fluids into the overlying plate (Figure 2) [*Ranero et al.*, 2008]. Hydrocarbon emissions are also reported where oceanic crust is subducted below oceanic crust, while abiotic synthesis occurs in presence of ultramafic rocks, water and moderate temperatures [*Mottl et al.*, 2004; *Proskurowski et al.*, 2008]. Furthermore, seepage occurs at transform plate boundaries where movement of plates is only horizontal but with deep-reaching plate margins and is often accompanied by earthquakes, which may trigger migration of deep fluids [*Suess*, 2014]. A high number of seepage systems within a variety of geologic settings also occur along passive margins [*Berndt*, 2005; *Suess*, 2014].

Three major elements have to be regarded to describe cold seeps systems: the hydrocarbon formation in depth, the plumbing system which transports fluids through geologic formations and, finally, the seepage system and morphology of cold seeps at the sediment surface [*Talukder*, 2012]. All three elements are described in the following sections.

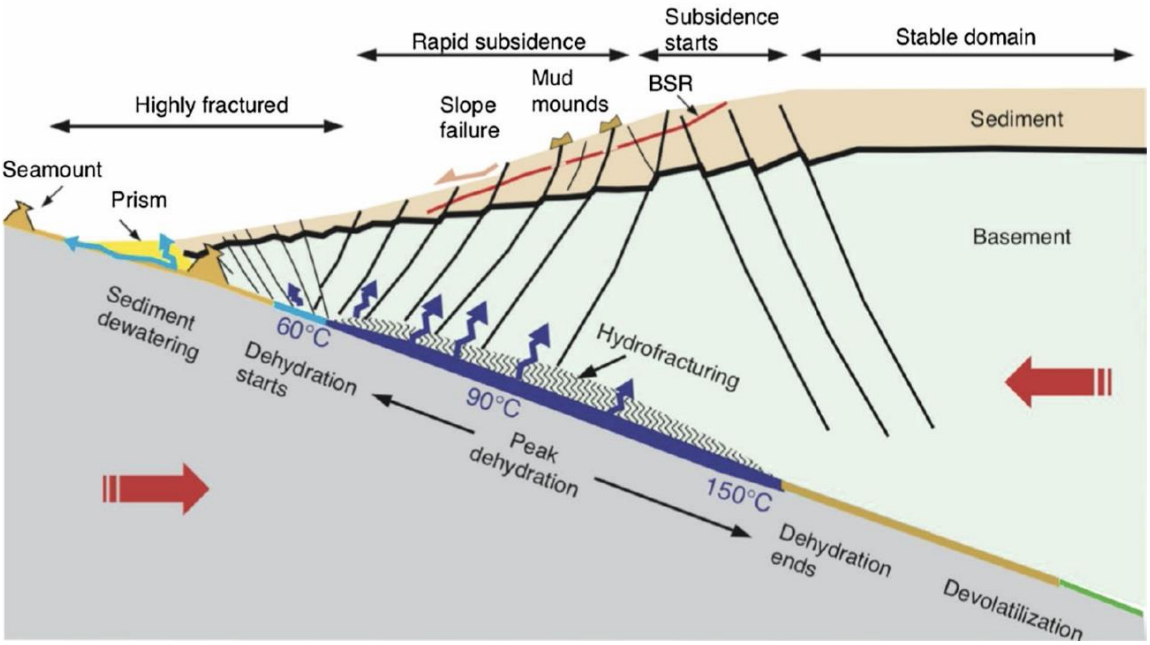

Figure 2: Erosive margin. Convergent margin off Costa Rica with small accretionary prisms, highly fractured edge of continental plate, region of pronounced subsidence due to removal (erosion) of material from plate underside, and stable continental framework rock; all features covered by seaward prograding hemipelagic sediments with well- developed bottom simulating reflector (BSR). Fluid escape features on lower-middle slope are mud volcanoes situated above temperature–pressure regime of mineral dehydration from top of down-going plate. Fluids and muds are forced upward through deep-reaching fractures. Subducted volcanic seamounts contribute to destruction of overriding plate edge leaving scars, scarps, faults and bulges that facilitate fluid escape [from *Suess*, 2014].

1.1.2 Hydrocarbon formation

Emitted hydrocarbons are formed in sediments by two major processes: thermogenic or biogenic. The base for both reactions is buried organic matter (CH_2O) produced mainly by marine primary productivity.

Thermogenic formation requires temperatures between 60 and 200 °C, which induce thermocatalytic cracking of organic material and the formation of hydrocarbon gases and oil [*Hunt*, 1979]. The relative amount of higher hydrocarbons is proportional to temperature, age, and organic matter content in the sediments [*Rice and Claypool*, 1981],

but also depends on the source material [*Floodgate and Judd*, 1992] and on the hydrogen content relative to available carbon [*Hunt*, 1991]. In high hydrogen to carbon systems oil formation dominates and in lower hydrogen to carbon natural gas dominates [*Hunt*, 1991]. At temperatures higher than 200°C, methane formation is most prominent, whereas oil and higher hydrocarbons are produced at lower temperatures [*Floodgate and Judd*, 1992]. Microbial degradation of organic matter produces mainly methane as part of the exogenic carbon cycle. Methanogenesis, the last step in the metabolic carbon pathway, is performed by anaerobic archaea via three main processes: hydrogenotrophic (Eq.1), acetate fermentation (Eq. 2) and methylotrophic pathways. The first two pathways are more common [*Whiticar*, 1999]:

Hydrogenotrophic pathway $CO_2 - 8H^+ + 8e^- \rightarrow CH_4 + 2H_2O$, (Eq.1)

Aceteate fermentation pathway $CH_3COOH \rightarrow CH_4 + CO_2$, (Eq.2)

Hydrogen (H^+) and acetate (CH_3COOH) are transformed into methane (CH_4) and carbon dioxide (CO_2). Hydrogen and acetate are also required for sulfate reduction and, therefore, are not available for methanogens in the zone where sulfate is present. Therefore, the two described pathways by Equations 1 and 2 are restricted to the methanic zone, where sulfate is limited [*Whiticar*, 1999]. In-situ formation of hydrocarbons leads to an increase in pore pressure in the sediments, which drives upward advection of the produced hydrocarbons towards the overlying lower pressured sediments. The hydrocarbons accumulate in the nearest structural and stratigraphic trap [*Hunt*, 1990] or will be released at the seafloor.

The molecular and isotopic composition of the hydrocarbons can be used to infer their origin. When emitted as bubbles at the seafloor, the gas can be collected using devices designed for this purpose and operated by an ROV. Dissolved gases in the sediment can be sampled using a headspace technique [*Pape et al.*, 2010b]. Thermogenic formation produces not only methane but other hydrocarbons, thus if the ratio between methane (C_1) and the higher hydrocarbons (C_{2+}), which includes ethane, propane, butane, pentane and hexane, its origin is most likely thermogenic. [*Claypool and Kvenvolden*, 1983]. The higher the methane content of the gas ($C_1/C_{2+} > 1000$), the more likely it is biogenic, formed by methanogens, which produce pure methane.

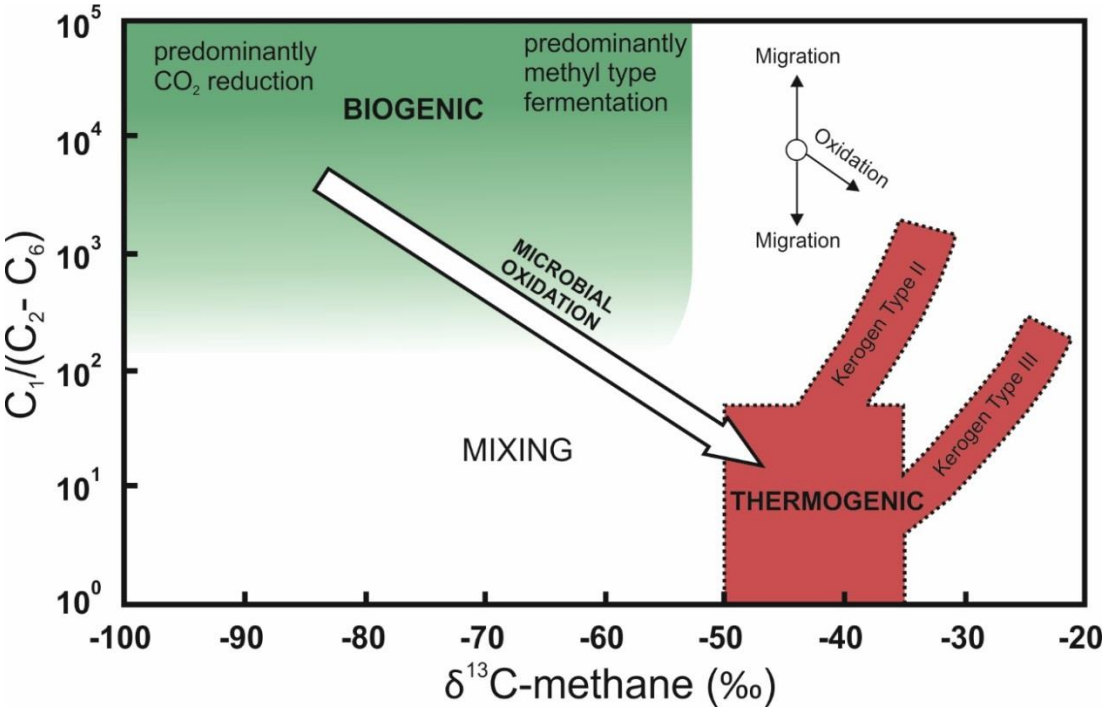

Figure 3: Bernard diagram. Molecular and isotopic composition of gas is combined to distinguish between thermogenic and biogenic gas formation [modified after *Whiticar*, 1999].

For a more detailed analysis C_1/C_{2+} values can be plotted against the isotopic carbon composition of CH_4 [*Claypool and Kvenvolden*, 1983; *Whiticar*, 1999], reported in delta-notation ($\delta^{13}C$) and expressed in ‰:

$$\delta_x = \left[\frac{(R_a)_{sample}}{(R_a)_{standard}} - 1\right] 10^3 \qquad \text{(Eq.3)}$$

Where R_a is the $^{13}C/^{12}C$ ratio of the sample relative to the Vienna Pee Dee Belemnite (V-PDB) standard [*Whiticar*, 1999]. This plot is also known as the "Bernard diagram" [*Bernard et al.*, 1978]. Gases enriched in ^{13}C, with $\delta^{13}C$ values higher -50‰ are of thermogenic origin (Figure 3). A biogenic source is indicated when $\delta^{13}C$ values are lower than -50‰ and can easily reach values around -100‰ depending on the methane reduction process [*Rice and Claypool*, 1981; *Whiticar*, 1999]. However, thermogenic gas that migrates upwards from its source depth can mix with shallow formed biogenic gas and thus, the hydrocarbons sampled at or near the seafloor commonly represents a mixture of both sources. Furthermore, fractionation processes due to microbial consumption of methane influence its isotopic composition and may hamper a clear classification of its source [e.g. *Prinzhofer and Huc*, 1995] (see chapter 1.2.1. Methane in sediments).

1.1.3 Plumbing systems

Plumbing systems, which transport fluids from depth towards the seafloor, are complex and only fairly constrained. This short introduction of possible plumbing systems is based on the review of *Talukder* [2012], the publications mentioned therein and include mud volcanism as additional trigger for fluid flow [*Kopf*, 2002].

Several mechanisms are described, which trigger fluid flow from the deep sediments to the seafloor:

1) Tectonic (faulting and fracturing)
2) Overburden erosion
3) Subducted seamounts
4) Seismic loading and earthquakes
5) Tidal cycle and sea level changes
6) Mud volcanoes

Tectonically triggered fluids follow faults and fractures, which were created by tectonic stress in rock formations mainly at active continental margins. When an overburden erosion reduces lithospheric pressure, sediment and over-pressured fluids from below migrate upwards, leading to seafloor seepage such as those observed at the headscarp of a landslide. As seamounts subduct they generate a localized uplift of the margin wedge above the subducted seamount and the resulting scars and faults in the overlying plate open numerous pathways for fluid migration. Sediment loading and earthquakes can trigger seepage at passive margins, along transform faults earthquakes are also an important trigger for fluid flow. Tidal cycles and long periods of sea level lowstand result in hydraulic pressure changes in the sediments and can trigger elevated fluid flow activities. Mud volcanoes are an important, and perhaps less studied system where deep-source fluids discharge at the seafloor, in some cases influenced by moderate to strong earthquake activities. (Mud volcanoes are discussed in more detail in chapter 1.1.5)

1.1.4 Seepage systems at the seafloor

Regionally, the geologic setting on active or passive margins and the plumbing system control the morphology and appearance of the seepage system. Near seep sites the most

important factors are physical properties and flux rates and composition of the advecting fluids. Pockmarks are created by strong fluxes of liquids and gas, the smaller features called unit-pockmarks by pore water seepage [*Hovland et al.*, 2005, 2010; *Cathles et al.*, 2010]. Episodic flow can lead to the build-up and collapse of seafloor structures. Mud volcanoes with rapid and voluminous fluxes with a high amount of plastic sediments will build mud domes and ridges at the seafloor [*Talukder*, 2012]. If the material is more liquid due to a higher water content mud volcanoes with a flat top or a conical top are built [*Barber et al.*, 1986; *Kopf*, 2002; *Feseker et al.*, 2009].

Benthic chemosynthetic seep communities, including microbial mats and macrofauna are excellent indicators of fluid seepage. Cold seeps, including those associated with mud volcanoes are ecosystems that host distinct biogeochemical processes. Upward migrating methane is commonly degraded by a process called anaerobic oxidation of methane (AOM, more detailed description in chapter 1.2.1 Methane in sediments). Products of this reaction are dissolved inorganic carbon (HCO_3^-) and sulfide (HS^-). The sulfide is used by sulfur-oxidizing bacteria, clams, mussels and tube worms [*Barry et al.*, 1996; *Sahling et al.*, 2002, 2003], and leads to precipitation of iron-sulfide minerals. The distribution of the fauna indicates the seepage intensities, methane/sulfide fluxes below microbial mats are stronger than fluxes below clams, and mussels appear in lower flux environments (Figure 4) [*Sahling et al.*, 2002; *Torres et al.*, 2002; *Suess*, 2014]. Another consequence of AOM is authigenic precipitation of carbonates [*Bohrmann et al.*, 1998; *Teichert et al.*, 2005; *Han et al.*, 2008]. Carbonates in various shapes are formed by precipitation of dissolved inorganic carbon (HCO_3^-) with available calcium. Authigenic carbonates and seep fauna can further be used as indicators for past seepage sites [*Suess*, 2014].

Along continental slopes, cold seeps are often associated with gas hydrate accumulation. Hydrates are ice-like structures with a high storage capacity for gases [*Kvenvolden and Claypool*, 1988; *Bohrmann and Torres*, 2006]. They form when hydrocarbon saturation in pore water is exceeded, enough water is available and the attendant temperature and pressure conditions fall within the gas hydrate stability field at a given salinity [*Sloan*, 2003; *Bohrmann and Torres*, 2006]. In cold arctic water, gas hydrates occur at shallow depths around 300 m, where in warm tropical waters, the stability zone is not reached until 750 m depth [*Suess*, 2014]. Moderate fluxes of hydrocarbons are required to build solid layers of gas hydrates [*Roberts et al.*, 2006]. Too strong fluxes driven by high upward fluid velocities hamper gas hydrate accumulation, and when fluxes are too slow the hydrocarbon flux can only sustain gas hydrates formation [*Brooks et al.*, 1986].

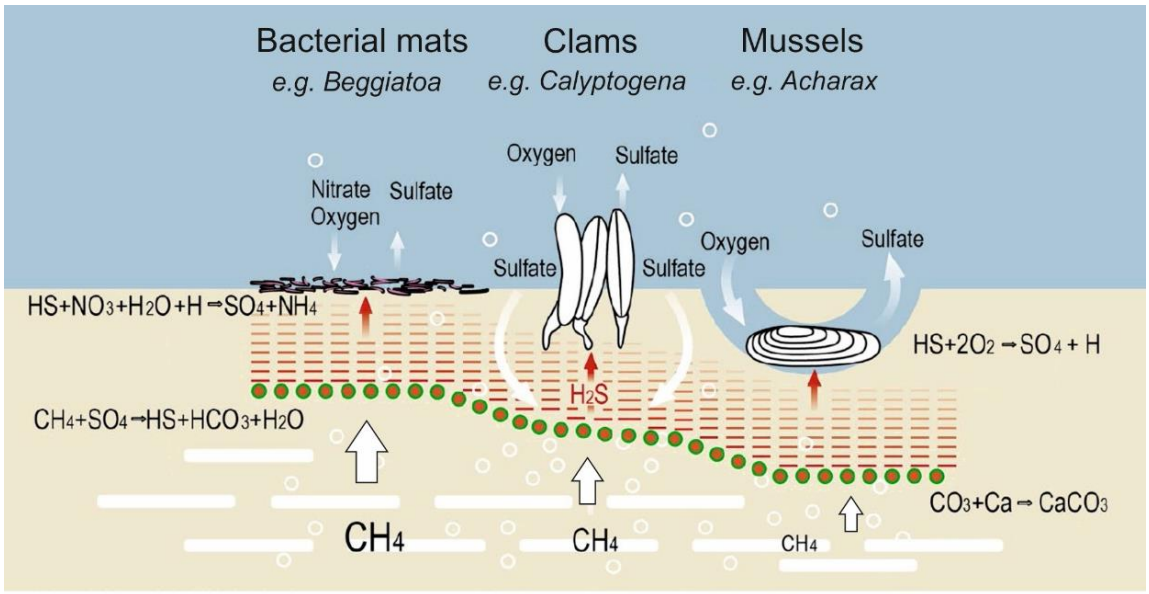

Figure 4: Anaerobic oxidation of methane. Buried gas hydrates and free gas from below supply different rates of methane (arrows) to AOM-consortia (red-green circles) concentrated at flux dependent depths below seafloor. The consortia consume seawater sulfate and oxidize methane. Produced hydrogen sulfide and bicarbonate; hydrogen sulfide rises to the sea floor and is oxidized in bacterial mats, clams or mussels using oxygen or nitrate; in the process calcium carbonate precipitates [modified after *Sahling et al.*, 2002; *Suess*, 2014].

Sediment temperatures increase with depth in accordance with the local geothermal gradient; thus there is also a lower limit to the gas hydrate stability zone. Below the stability zone free gas can accumulate beneath permeability seals, which in some cases may be due to gas hydrate accumulation in the sediment pore space. Free gas increases the hydrostatic pressure, which may push gas hydrate and the surrounding sediment upwards, leading to formation of gas hydrate mounds at the seafloor [*Hovland and Svensen*, 2006; *Paull et al.*, 2008]. An overpressure can further lead to hydrofracturing of the sediment package and leads to seepage at the seafloor [*Tréhu et al.*, 2004; *Talukder*, 2012]. Because they are less dense than seawater, gas hydrates exposed at the seafloor can float up in the water column, leaving scars in the sediments and a distinct morphology at the seafloor [*MacDonald et al.*, 1994; *Pape et al.*, 2011]. Changes in the environment, e.g. temperature increase or sea level changes, affect the depth range of hydrate stability, gas hydrate dissociation results in input of hydrocarbon gases into the water column. Hydrate dissociation or dissolution can further be a possible source for seepage [e.g. *Westbrook et al.*, 2009].

1.1.5 Mud volcanoes

Mud volcanoes (MVs) are, in contrast to other cold seeps, the superficial results of liquefied sediment-transport towards the surface [*Dimitrov*, 2002; *Van Rensbergen et al.*, 2003; *Deville et al.*, 2010]. The fluidized sediment or mud breccia matrix depends on the underlying strata. Transport of low-competence parent bed and rock fragments can often be related to the regional geology and clay or shale-bearing lithologies [*Kopf*, 2002]. *Van Rensbergen* [2003] concluded that subsurface sediment mobilization requires movable sediments, abundat fluids and a pressure gradient to initiate the ascent. Furthermore, the shallow subsurface is more prone to mobilization, because there, sediments are less compacted and more fluids are available than in the deep subsurface. Fluid seepage is often observed at the sediment surface, where a crater, a mud flow or other morphologies reveal the mud extrusion center. However, sediments, liquids and gases do not all necessarily originate from the same depth or source [*Kopf*, 2002]. Most mud volcanoes are described with a main feeding channel for fluids and mud in the center of the mud volcano [e.g. *Bohrmann et al.*, 2003; *Sauter et al.*, 2006; *Feseker et al.*, 2008; *Kutterolf et al.*, 2008; *Suess*, 2014]. *Deville et al.*, [2006, 2010] introduced a model for sediment and fluid mobilization at a circular uplift structure around mud volcanoes. There are different interpretations for this uplift, such as mobile shale formation, reverse fault formation or formation of a downward tapering fault cone, but all show two migration pathways for fluids. One pathway exists along the outer circular fault structure and the other one along the main feeding channel from depth (Figure 5). All of these indicate that deep fluids predominantly migrate along the inner pathway while shallow fluids mainly escape along the surrounding fault structure probably without any connection between the two pathways [*Deville et al.*, 2010].

When fluids and muds reach the seafloor, high contents of gaseous and dissolved hydrocarbons are released into the hydrosphere. Numerous studies attempted to quantify the methane flux from mud volcanoes and investigated their possible impact on the atmosphere [e.g. *Dimitrov*, 2003; *Haese et al.*, 2003; *Kopf*, 2003; *Milkov*, 2003; *Vanneste et al.*, 2011]. Most of these calculations are based on sediment data collected in the center of the MV or based on observed gas emissions rates, but dissolved methane emissions from a mud flows itself has not been considered so far [*Wallmann et al.*, 2006; *Vanneste et al.*, 2011].

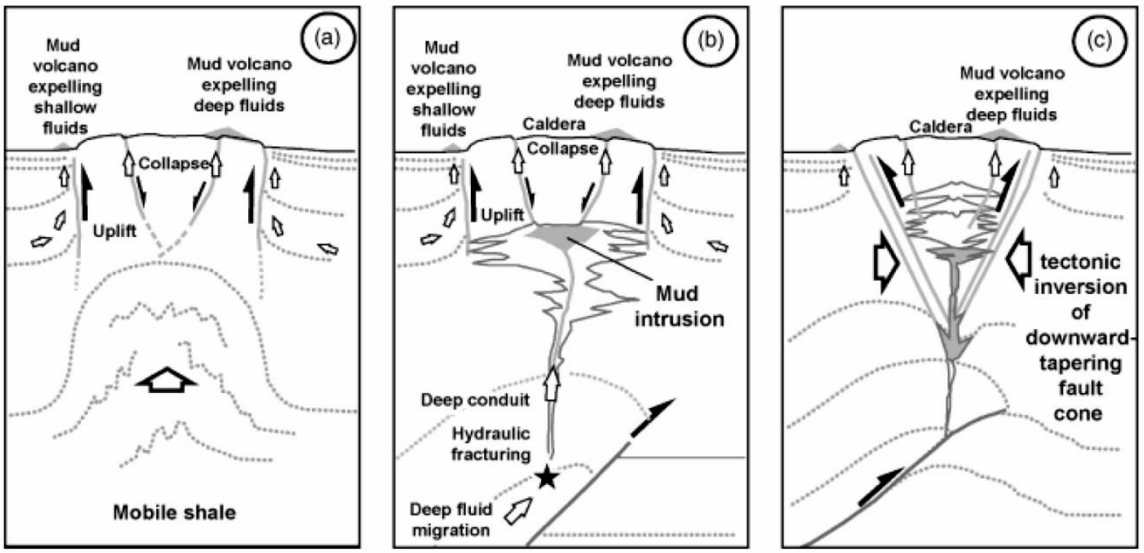

Figure 5: Different interpretations of the genesis of the sub-circular massive uplift structures. Two pathways for fluid migration are illustrated for shallow and deep fluids [from *Deville et al.*, 2010].

The fresh extruded mud is full of gas [e.g. *Pape et al.*, 2014] which is released into the water column by compaction and diffusion as the mud flow progresses. *Wallmann et al.* [2006] suggests that the diffusive input of methane by both quiescent dewatering and by the degassing of mud may be similar, but the data are very limited so far.

1.1.6 Mud volcanism at the Calabrian Arc

The Calabrian Arc is located in the northern Ionian Sea in the western Mediterranean and between the plate boundaries of Africa and Eurasia. It is situated above a NW dipping subduction system with slow convergence rates of 4–5 mm/yr [*D'Agostino et al.*, 2008; *Devoti et al.*, 2008; *Polonia et al.*, 2011; *Panieri et al.*, 2013]. Above this subduction zone the Calabrian accretionary prism is 300 km wide and extends almost 300 km, with a change in topography from 1928 m onshore in Calabria to water depths of around 4000 m (Figure 6). Since the late Miocene (> 10Ma), the accretionary prism has been pushed over 300 km towards the southern Apennines and the Ionian domain. The submarine section of the accretionary prism is divided into three sections, the Fore-arc basin, the inner and outer Pre-Messinian prism, and the Post-Messinian prism [*Rossi and Sartori*, 1981; *Ceramicola et al.*, 2014]. The Pre-Messinian prism contains many thrusts that indicate out-of-sequence movements. The largest movement is represented by the Calabrian Escarpment which is up to 750 m high and 200 km long. This escarpment divides the Pre-Messinian prism into an inner and outer plateau, the latter one featuring a rougher surface structure and higher relief [*Ceramicola et al.*, 2014]. The possibility of mud volcanoes in this prism was reported

by *Sartori* [2003] and later confirmed and investigated by several studies (Figure 6) [*Praeg et al.*, 2009; *Panieri et al.*, 2013; *Ceramicola et al.*, 2014; *Mascle et al.*, 2014]. Almost all MVs identified are located on the inner Pre-Messinian prism and within the fore-arc basins. Within this prism fluids migrate upwards along fault structures influenced by evaporitic and shale seals in the center of the fore-arc basins [*Ceramicola et al.*, 2014].

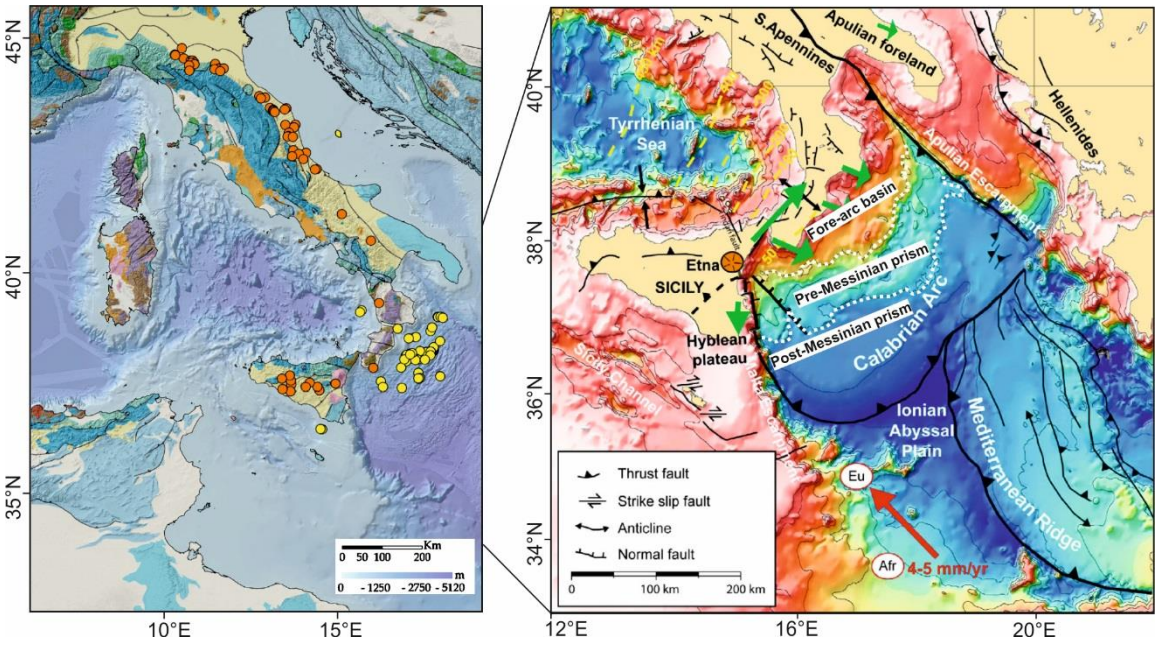

Figure 6: Distribution of mud volcanoes and fluid/mud releasing structures on the Calabrian margin (yellow dots) and terrestrial mud volcanoes on Italy and Sicily (orange dots, left map) [from *Mascle et al.*, 2014]. Tectonic setting with the main morpho-tectonic zones of the Calabrian margin is demonstrated in the right map [modified from *Polonia et al.*, 2011 and *Ceramicola et al.*, 2014].

1.2 METHANE ENVIRONMENTS

1.2.1 Methane in sediments

Transport processes. Methane is transported in sediments by two major processes: fluid advection and diffusion. Fluid advection, including dissolved and gaseous methane, can be driven by buoyancy effects e.g. due to gas inflow, gas formation or by pressure gradients. Fast sediment accumulation or compaction at active or passive margins, can increase pore pressure within the sediments. If fluid pathways are blocked or not available, excess pore pressure can create cracks and fluid migration pathways through the overlying sediments or geological formations [*Etiope and Martinelli*, 2002; *Kopf*, 2002]. Fluid advection is a fast process and accelerates the more gas is available with upward migrating methane reaching velocities of up to 10^3 m/day [*Etiope and Martinelli*, 2002]. The second process diffusion describes migration of molecules along a concentration gradient from high to low concentration and depends on the porosity in sediments and the steepness of the concentration gradient. Flow of molecules is not limited to the upward direction, diffusion always follows concentration gradients independent of the directions. It is a much slower process compared to advection [*Krooss and Leythaeuser*, 1996; *Etiope and Martinelli*, 2002; *Luff et al.*, 2004], nevertheless, the methane input by diffusion can be significant and should not be underestimated. Diffusive flux (J) of methane can be calculated under steady state conditions according to Fick's first law [*Berner*, 1980]:

$$J = -\varphi \cdot D_s \cdot dC/dz \qquad \text{(Eq.4)}$$

where J is the diffusive flux [mmol/m² a], φ is the porosity, D_S is the sediment diffusion coefficient [m²/a], C is the concentration of methane [mM] and z is the depth [m]. D_s can be calculated after *Boudreau* [1997], where $D_s = D_0/\theta$, with a porosity-deviated tortuosity (θ) and the diffusion coefficient of methane in seawater D_0.

Biogeochemical processes. The driving force for the following processes is organic matter (OM) which is deposited as organic detritus (CH_2O) in sediments. This detritus is formed by primary productivity in surface waters, it sinks through the water column and if not decomposed during transport or at the sediment-water interface, it is buried in sediments [*Suess*, 1980]. In sediments where oxygen is available, CH_2O is respired aerobically to CO_2. Once oxygen is consumed, the ongoing carbon metabolism uses nitrite, iron(III), and manganese(IV) to decompose organic matter according to the energy yield of each reaction [*Froelich et al.*, 1979]. Once all inorganic electron acceptors are depleted, organic matter is decomposed by fermentation and releases hydrogen and short-chain organic compounds,

that are required for organoclastic sulfate reduction and methanogenesis [*Valentine*, 2002; *Pohlman et al.*, 2013]. Methanogenesis is described in the previous paragraph and processes of the microbial methanogenesis are displayed in Figure 7.

When the resulting methane diffuses or is slowly advected upwards, it is often consumed by anaerobic oxidation of methane (AOM), a "microbial process embedded within a complex network of biogeochemical reactions" [*Sommer et al.*, 2006]. A consortium of sulfate reducing bacteria and anaerobic methane oxidizing archaea consumes methane (CH_4) and sulfate (SO_4^{2-}) and releases bicarbonate (HCO_3^-) and sulfide (HS^-) described by the overall reaction [*Hoehler et al.*, 1994; *Niewöhner et al.*, 1998; *Hinrichs et al.*, 1999; *Boetius et al.*, 2000]:

$$SO_4^{2-} + CH_4 \rightarrow HCO_3^- + HS^- + H_2O \qquad \text{(Eq.5)}$$

Seawater sulfate diffuses downwards into the sediment pore water, where it is reduced by either organoclastic sulfate reduction or AOM. Methane formed by microbial or thermogenic processes migrates upwards by advection and/or diffusion. The zone where both dissolved compounds are almost completely reduced by AOM is called the sulfate-methane interface (SMI) [*Niewöhner et al.*, 1998; *Borowski et al.*, 1999; *Paull et al.*, 2000]. The depth of the SMI depends on the methane flux from below, where higher methane inputs from below shift the SMI towards shallower depths [*Borowski et al.*, 1996, 1999].

Bicarbonate (HCO_3^-), also expressed as dissolved inorganic carbon (DIC) or alkalinity, is a product of AOM and induces authigenic carbonate formation when calcium and other cations are availlable [*Bohrmann et al.*, 1998; *Naehr et al.*, 2007; *Snyder et al.*, 2007; *Nöthen and Kasten*, 2011] and thus, these methane derived carbonates are good indicators for AOM at recent and former seepage sites. Another product of AOM is sulfide (HS^-). In the presence of dissolved iron , ironsulfides are formed and create dark mineral precipitations [e.g. *Hensen et al.*, 2003] observed as black spots or areas in sediments.

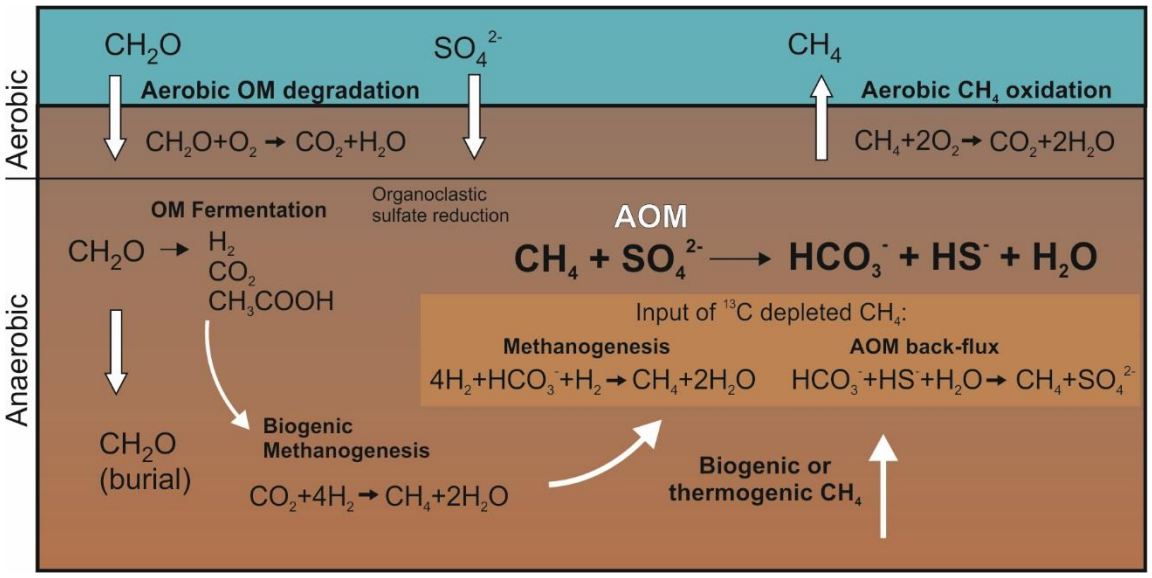

Figure 7: Microbially-mediated carbon transformations in methane seeps. Organic matter (OM, represented as CH_2O) deposited on the seafloor is aerobically and anaerobically degraded to CO_2, hydrogen (H_2) and smaller organic compounds (represented as acetate, CH_3COOH). Methane may be anaerobically oxidized, aerobically oxidized (6) or emitted to the water column. Methane is produced by biogenic methanogenesis or of thermogenic origin. The anaerobic oxidation of methane (AOM) is a possible sink of methane as well as aerobic oxidation in oxic sediments or in the water column. Input of ^{13}C depleted methane is displayed by two processes: Methanogenesis with AOM-derived bicarbonate and AOM backflux [modified after *Pohlman et al.*, 2013 and *Yoshinaga et al.*, 2014].

As microbial activity leads preferentially to the consumption of the lighter carbon isotope ^{12}C, an enrichment of ^{13}C at the lower part of the SMI of both carbon substrates CH_4 and DIC would be the logical consequence [*Alperin et al.*, 1988; *Whiticar*, 1999]. However, recent studies report of a ^{13}C depletion within the SMI [*Pohlman et al.*, 2008; *Hong et al.*, 2013; *Treude et al.*, 2014; *Yoshinaga et al.*, 2014]. So far two processes are described that explain this reverse effect:

(1) The more common and accepted explanation is the secondary methanogenesis in the lower part of the SMI [*Borowski et al.*, 1997; *Paull et al.*, 2000; *Hong et al.*, 2013, 2014]. Here, instead of using DIC derived from organic matter degradation, methanogens use the DIC derived from AOM to generate ^{13}C depleted CH_4 (Figure 7):

$$4H_2 + HCO_3^- + H^+ \rightarrow CH_4 + 3H_2O \qquad \text{(Eq.6)}$$

(2) The second explanation is introduced by *Yoshinaga et al.* [2014] and is based on a theory that enzyme-catalyzed reactions, like AOM, are reversible [e.g. *Casciotti*, 2009]. Indeed, a AOM back flux up to 5% of DIC to CH_4 had been reported before by *Holler et al.* [2011]. In contrast to methanogenesis no hydrogen is required to form CH_4, however, the

net methane production is not achieved [*Yoshinaga et al.*, 2014]. This back flux occurs preferably in the lower part of the SMI, where sulfate is limited (Figure 7).

However, even if there is additional input of methane below or in the lower part of the SMI, AOM will act as a microbial filter suppressing the release of methane into the overlying sediments and bottom water [*Alperin et al.*, 1988; *Hinrichs et al.*, 1999; *Boetius et al.*, 2000; *Valentine and Reeburgh*, 2000]. The efficiency of this filter is reported to reduce 50–96% of the upward migrating methane [*Torres et al.*, 2002; *Boetius and Suess*, 2004; *Sommer et al.*, 2006] and strongly depends on the flux from below. With a very strong diffusive flux or advecting fluids, containing dissolved and gaseous CH_4, the capacity of AOM is exceeded and methane is released into the overlying water column.

1.2.2 Methane in the water column

Transport processes. Once methane reaches the hydrosphere it can be transported in various ways. When methane is emitted as bubbles on the seafloor, a fraction of the gas dissolves during its way through the water and creates a plume in the water column [*Leifer and Judd*, 2002; *McGinnis et al.*, 2006; *Greinert and McGinnis*, 2009]. Bubble emission in water depth shallower than 100 m frequently reach the atmosphere and, hence, contribute to the atmospheric methane budget [*Hovland et al.*, 1993; *McGinnis et al.*, 2006; *Gentz et al.*, 2014; *Mau et al.*, 2015]

Bubble emissions in the deep sea often do not reach surface waters [*Damm and Budéus*, 2003; *Schmale et al.*, 2005; *McGinnis et al.*, 2006]. Bubbles are observed only in the lower part of the water column, dissolve during their ascent in the water and, thereby, create a dissolved methane plume in that area [*Clark et al.*, 2003]. The rising height of methane bubbles depends mainly on the residual bubble diameter and water depth [*McGinnis et al.*, 2006]. In addition to bubble dissolution methane diffuses through the bubble's surface due to the strong concentration gradient between bubble and seawater [*Rehder et al.*, 2009]. Methane is then replaced by other gases available in the water such as carbon dioxide, oxygen or nitrogen. Most of the bubbles from deep emission sites reaching surface waters do not contain methane anymore and, therefore, are not significant for carbon budgets. The rising height of the bubbles can be further controlled by hydrate coatings, which seals the bubble as long as the bubble is within the gas hydrate stability field [*Rehder et al.*, 2002; *Judd*, 2003]. The same effect is observed with bubbles coated by oil where lifetime is extended due to the sealing nature of oil [*MacDonald et al.*, 2002; *Heeschen et al.*, 2003]. If the surrounding methane concentrations are already high, methane will diffuse slower out

of the bubble since the concentration gradient is smaller [*Clark et al.*, 2003]. Another process is described for deep seepage, where a vertical upwelling of the gas plume was observed. Upwelling water masses support and accelerate the upward flux of bubbles, and, therefore, reduce bubble dissolution [*Leifer et al.*, 2006; *Solomon et al.*, 2009].

Especially in shallow areas this upwelling may enhance the flux into the atmosphere. Recent studies of an abandoned well site with very strong seepage report from an opposite effect. A spiral vortex bubble plume motion enhances the travel time within the bubble stream and therefore, most of the methane is dissolved out of the bubbles although the emission site is located in only 90 mbsl [*Schneider von Deimling et al.*, 2015]. The dissolved methane forms a megaplume which is advected, spreads along a thermocline and only a relatively small portion of the methane released is transported into the atmosphere (Figure 8) [*Leifer and Judd*, 2015; *Leifer et al.*, 2015; *Schneider von Deimling et al.*, 2015].

Several methods are described so far to determine the methane input in form of bubbles into the water column. They include visual observations by video imaging [e.g. *Sauter et al.*, 2006; *Römer et al.*, 2012], by hydroacoustic imaging [e.g. *Greinert et al.*, 2006; *Römer et al.*, 2014] and also are based on collected gas volumes over time [*Römer et al.*, 2012]. These methods provide estimates about the diffusive methane input in the water column. However, direct measurement of methane concentration in water samples has the potential to give a more realistic value which can be used for input calculations in the study area. The total diffusive input is calculated by the spatial diffusion, advection and methane oxidation rates (MOx) in the water column. All three processes are described in the following:

In dissolved form methane can be advected horizontally by water currents. This advection (ADV) is calculated by the in situ methane concentration [CH_4] and the current velocity (v) [e.g. *Mau et al.*, 2015]:

$$ADV = v \cdot [CH_4] \qquad \text{(Eq.7)}$$

During advection CH_4 is not only transported from one point to another, but is mixed and diluted with the bottom water. Changes in current velocity and direction result in a turbulent mixing in the water, the eddy diffusion. The diffusion coefficients for horizontal and vertical direction parameterize the eddy diffusivity (∂) and include these turbulences in the calculations. Therefore, diffusive flux of methane (DIF) in the water column is calculated by the horizontal/vertical diffusion coefficient and the horizontal/vertical concentration gradient ($\partial[CH_4]/\partial x$), respectively [*Roberts and Webster*, 2002; *Largier*, 2003]:

$$DIF = \partial \cdot (\partial[CH_4]/\partial x) \qquad \text{(Eq.8)}$$

The horizontal diffusion gradient ranges between 0.1 and 1000 m^2/s and depends on the distance to shore [*Sundermeyer and Price*, 1998; *Largier*, 2003]. If the distance is around 0.1 km, ∂ horizontally will be in the order of 1–10 m^2/s, 100 m^2/s for a distance of 10 km and 1000 m^2/s for 100–1000 km distance from land. For the vertical diffusion coefficient values between 10^{-3}–10^{-5} m^2/s are reported. The vertical eddy diffusivity depends on stratification and on the energy in the water column e.g. produced by wind or tidal fluctuations [*Denman and Gargett*, 1983; *Wunsch and Ferrari*, 2004; *Palmer et al.*, 2008; *Mau et al.*, 2015]. Vertical eddy diffusion is very limited at thermoclines or pycnoclines, therefore dissolved plumes are often found along pycnoclines, where they spread in the horizontal direction (Figure 8) [*Damm et al.*, 2005; *Schmale et al.*, 2010; *Gentz et al.*, 2014]

Biogeochemical processes. In order to construct the transport processes and final sink of methane in the water column, the possible oxidation reactions of methane have to be regarded. If oxygen is available, methane will be microbially oxidized in the water column to carbon dioxide and water [*Sansone and Martens*, 1978; *Valentine et al.*, 2001; *Kessler et al.*, 2011; *Mau et al.*, 2013]:

$$CH_4 + 2O_2 \rightarrow CO_2 + 2H_2O \qquad \text{(Eq.9)}$$

Another factor which can control the size, activity and structure of MOx-communities is the abundance of trace metals like iron and copper [*Crespo-Medina et al.*, 2014; *Steinle et al.*, 2015]. However, environmental factors which influence the oxidation rates are still poorly constrained [*Steinle et al.*, 2015].

As previously explained oxidation of methane in sediments or the water column results in an enrichment of ^{13}C in methane. Normal methane background concentrations are in equilibrium with air and hence, can be isotopically distinguished from depleted methane injected by seepage [*Sansone et al.*, 1997]. Together with lateral transport and dilution, microbial oxidation is one of the major sinks for diffusive transported methane in the water column. But if the vertical transport exceeds the horizontal transport and methane oxidation rates are too low to decompose all of the methane, methane will reach the mixed layer at the water surface. This layer defines surface water with a homogenous density that directly interacts with the overlying air [*Kara*, 2003], thus methane in the mixed layer can be easily transported into the atmosphere.

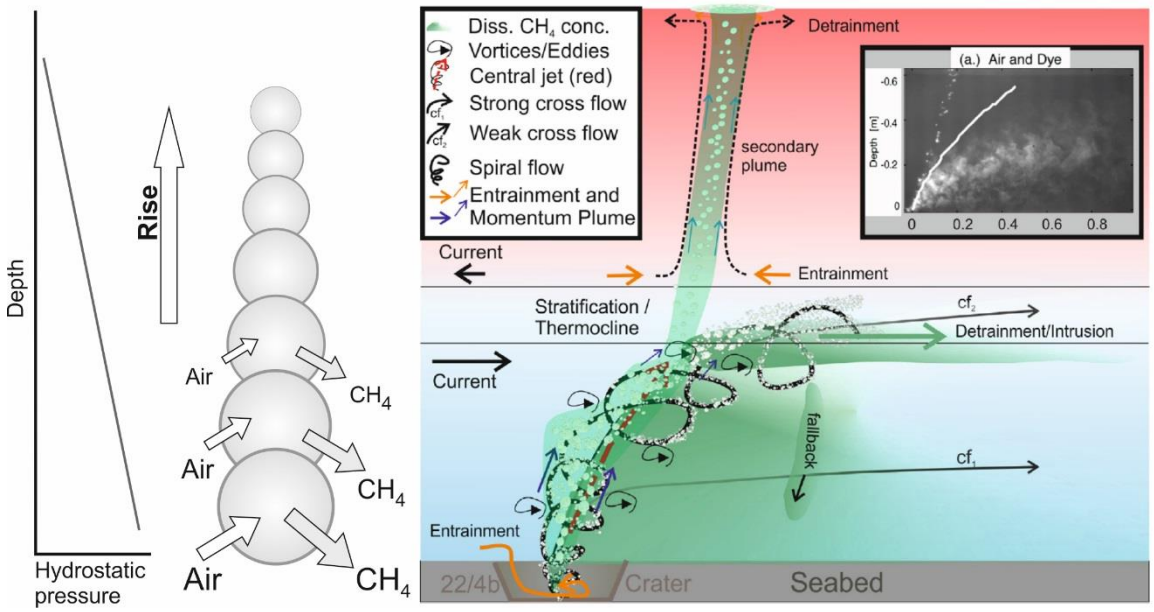

Figure 8: Schematic of gas exchange in bubbles emitted from seeps (left). Methane (CH_4) outflow is greater than air inflow and bubble diameter decreases with decreasing hydrostatic pressure [modified from *Leifer and Judd*, 2002]. Schematic sketch indicates a mega plume and related pathways of gaseous and dissolved methane in response to various cross-flow velocities (right) [from *Schneider von Deimling et al.*, 2015].

1.2.3 Methane in the atmosphere

Methane is the second strongest greenhouse gas with, whose atmospheric concentration has increased by a factor of 2.5 since preindustrial times [*IPCC*, 2013]. Because the warming potential of methane is 21 times that of carbon dioxide [*IPCC*, 2007] it plays an important role in the current global warming [*Badr et al.*, 1991]. Natural seepage, including terrestrial and marine seepage, is estimated to reach 53±11 Tg/yr and, thus, makes it to an important input source to the global methane budget [*Etiope et al.*, 2008]. However, the contribution to the global methane input by marine seepage remains largely unknown because of the uncertainty of losses in the water column and the low amount of studied locations in the ocean [*Leifer et al.*, 2015]. Thus, "there is an urgent need to develop, demonstrate, and apply new measurement technologies" [*Leifer et al.*, 2015] to investigate marine seepage sites and their contribution to the atmospheric budget. Especially because the current global warming may increase oceanic methane emissions [*Westbrook et al.*, 2009; *Kretschmer et al.*, 2015], particularly in Antarctica and in the Arctic, where global warming is most pronounced. Global warming would not only influence terrestrial methane release from permafrost [*Christensen*, 2004; *Schuur and Bockheim*, 2008], but also gas hydrate dissociation at continental margins [*Jung and Vogt*, 2004; *Mienert et al.*, 2005], and sea ice

melting [*Walter et al.*, 2006; *Damm et al.*, 2015] might accelerate methane release to the atmosphere. Most of high-latitude studies have been conducted in the Arctic and so far only little is known about methane dynamics in the Southern Ocean [*Heeschen et al.*, 2004; *Römer et al.*, 2014a].

1.3 MOTIVATION

Methane seepage at cold seeps is a well-known process that occurs globally at the seafloor. However, considering the overall amount of investigated seepage sites, direct analyses of methane in the water column right above active cold seeps, especially above mud volcanoes, are still limited to only a few case studies. With the aim to contribute to the ongoing research of methane seepage in the marine realm and its impact to the global carbon cycle, three different topics were addressed in this study:

1) Investigation of new seepage sites in Antarctica

2) Development of a fast and simple detection method for methane in water

3) Water column investigation above an active mud volcano in the Mediterranean

1) Investigation of new seepage sites in Antarctica. Seepage in Antarctica is still poorly known, but, especially with respect to current global warming, these high latitudes have become an area of increasing interest. During research cruise ANTXXIX-4 with FS POLARSTERN in the Southern Ocean seepage sites were discovered within the Cumberland Bay and along the northern shelf of South Georgia. In order to obtain a detailed picture of the source and sink of methane, a number of sediment and water samples were taken and analyzed. Pore water data were used to reconstruct processes of the carbon cycle within the sediment while the source of methane and fractionation processes were investigated on the basis of molecular and isotopic analyses of methane. Moreover, oceanographic conditions were taken into consideration and measurements of methane concentration in the water column performed to answer the following questions: What is the cause of gas generation and seepage? Which biogeochemical reactions take place in the sediments and how does seepage-related methane affect the carbon cycle? What happens to methane in the water column? And, finally, how much methane is released into the atmosphere? Onboard work during this expedition demonstrated that sampling and analysis of methane in the water column has been a very time consuming process, which limits the amount of available data and clearly shows the urgent need for a new and more efficient method to analyze methane in water samples.

2) Development of a fast and simple detection method for methane in water. Recent developments in methane detection focus mainly on the water/atmosphere boundary to determine the amount of methane released into the atmosphere. Commonly, the instruments are continuously analyzing sea water which is pumped from several meters below the sea surface. However, this method is not suitable to detect methane in the deep

sea or in the lower part of the water column, where, in fact, the main transport and oxidation processes of methane have been reported. In order to conceive the dissolved methane plume behavior at seepage sites and the general methane sinks a large number of water samples is required. Most of the available methods are very time consuming with long preparation times as well as complicated sampling and storage processes. In situ mass spectrometry would have been the preferred detection method, but this technology had been still in its development phase and, therefore, could not be utilized for this thesis. A comparison of the previously used Vacuum-Extraction method with the newly developed method is given in Chapter 2. The new method benefits from only little preparation time, a simple sampling procedure and a fast detection method using Off-Axis Integrated Cavity Output Spectroscopy (OA-ICOS). This method was approved by intense sampling during two 6-week long research cruises and was further used for the final study in this thesis (Chapter 5).

3) Water column investigation above an active mud volcano in the Mediterranean Sea. The Venere MV is a recently discovered active mud volcano within the Calabrian Arc in the Ionian Sea. During the research cruise M112 with RV METEOR multiple gas emission sites were discovered along a circular structure around the mud volcano. The mud extrusion site was identified at the summit of the mud volcano and a relatively recent mud flow was observed on various mud flow deposits. So far, no study analyzed bottom water concentrations along mud flows and the impact of diffusive flux of methane from freshly extruded mud into the overlying water column has only been estimated. This thesis addresses several questions to investigate the total input of methane from an active mud volcano into the water column in Chapter 4: What is the origin of the gas and how is methane distributed in the water column? Where do the highest methane concentrations occur? How significant is the methane input at bubble emission sites in relation to the diffusive input above freshly extruded mud? And, finally, what are the migration pathways and does any methane reach surface waters and the atmosphere?

Guided by these questions, this work provides new insights into methane behavior in the water column focusing on (i) the Southern Ocean as specific region and (ii) the waters directly above a fresh mud flow in general. The newly developed method enables more extensive sampling and will simplify future water column investigations of methane around seepage sites.

CHAPTER 2: NEW DEVELOPED METHOD

RAPID ANALYSIS OF METHANE CONCENTRATION IN WATER SAMPLES USING HEADSPACE EQUILIBRATION AND OFF-AXIS INTEGRATED CAVITY OUTPUT SPECTROSCOPY (ICOS)

Patrizia Geprägs[1,*], Marta E. Torres[2], Timo Fleischmann[1], Susan Mau[1], Thomas Pape[1], Gerhard Bohrmann[1]

submitted in Limnology and Oceanography: Methods

[1]MARUM – Center for Marine Environmental Sciences, Department of Geosciences, University of Bremen, Klagenfurter Str., 28359 Bremen, Germany

[2]School of Oceanic and Atmospheric Sciences, Oregon State University, 104 Ocean Admin Building, Corvallis, OR 97331-5503, United States

Keywords: dissolved methane, headspace equilibration, Integrated Cavity Output Spectroscopy, discrete sampling, deep sea samples, greenhouse gases, fast and accurate, Vacuum Extraction

ABSTRACT

Laser-based instrumentation utilizing the off-axis integrated output spectroscopy (ICOS) technology has become increasingly popular for the continuous measurement of methane in air and surface seawater. Here we describe a novel and simple method for the analysis of discrete water samples, which extends the applicability of this technology also to deep-water samples. We document the suitability of the approach to both marine and fresh water systems. Samples are collected in large plastic syringes; headspace is generated using methane-free air and is analyzed with a Greenhouse Gas Analyzer (GGA, Los Gatos Research) after equilibration. Measuring one sample, including headspace addition, injection into the GGA and analysis of the sample, takes only 5–10 min. Methane concentrations ranging from 1.5–65000 nM are detectable with a precision better than 2.5%, thus allowing for measurements that range from typical seawater concentrations to the extremely high abundances encountered at methane seeps or in peat channels. This ability to generate data in the field is highly advantageous in refining sampling strategies. The approach described here enables fast and accurate measurements of methane in the field, uses low cost and reusable materials, and does not require chemicals for sample preservation.

INTRODUCTION

Methane is an important greenhouse gas, whose atmospheric concentration has increased by a factor of 2.5 since preindustrial times [*IPCC*, 2013]. Because the warming potential of methane is 21 times that of carbon dioxide [*IPCC*, 2007] it plays an important role in the current global warming [*Badr et al.*, 1991]. Even though the ocean source is thought to have only a small impact on the global methane budget, there is a lack of data to fully quantify this input source, such that its contribution, especially from shallow regions may be underestimated. It is possible that the ocean source term has been increasing due to ocean warming and release from either gas hydrate or permafrost [*Bange*, 2006].

Methane generated in marine sediments can accumulate below the seafloor and at some locations it discharges at cold seeps, either dissolved in fluids or, in the case of over-saturation, in the form of methane bubbles. In addition, conspicuous maxima in dissolved methane have been documented in oxic water layers, revealing production under oxic conditions in the water column [*Traganza et al.*, 1979; *Holmes et al.*, 2000; *Damm et al.*, 2009]. There is clearly a need to monitor methane concentrations in the water column, if we are going to fully constrain its role in the global carbon cycle and its potential contribution to the atmosphere. The pressing need for methane surveys is also evidenced in recent publications describing analytical approaches (e.g. Gülzow et al. 2011; Arévalo-Martínez et al. 2013; Magen et al. 2014; Li et al. 2015). Magen et al. (2014) described collection and preservation of water samples for subsequent measurement of methane in the headspace using gas chromatography, up to 3 months after collection. With the advent of off-axis integrated cavity output spectroscopy (ICOS), new instrumentation became commercially available for the continuous monitoring of greenhouse gases (methane and carbon dioxide) at atmospheric levels with high precision and accuracy [*Baer et al.*, 2002; *Berman et al.*, 2012]. This analytical breakthrough was expanded to continuously monitor CH_4 and CO_2 in surface seawater samples by use of an equilibrator system [*Schmale et al.*, 2010; *Gülzow et al.*, 2011; *Arévalo-Martínez et al.*, 2013; *Li et al.*, 2015]. Thereby, the water enters equilibrators where a constant volume of air is circulated through the water and equilibrates with the water phase. The air is then dried and transported to the analyzer and measured via ICOS [*Gülzow et al.*, 2011]. These two approaches combined, atmosphere and surface seawater analyses, allow for monitoring processes at the seawater-atmosphere interface at high resolution. However, not all of the methane entering the water column reaches the atmosphere. When methane is emitted as bubbles on the seafloor, a fraction of the gas dissolves during transit through the water column depending on release depth,

bubble volume and the buoyancy of the plume (e.g. Greinert & McGinnis 2009). Bubble dissolution creates patches of dissolved methane [*Clark et al.*, 2003], which in cases where methane emissions are persistent and of sufficient magnitude can form large continuous plumes. Only if this dissolved methane is transported to the mixed layer, it can be transferred to the atmosphere via sea-air gas exchange; the amount depends especially on wind speed (e.g. Mau et al. 2007). Furthermore, studies have shown that the methane within bubbles can be replaced by other gases via exchange processes during bubble ascent through the water column (e.g. McGinnis et al. 2006). In addition, microbial consumption of CH_4 restricts its release into the atmosphere [*Reeburgh*, 2007], and aerobic oxidation of methane may contribute to ocean acidification (e.g. Biastoch et al. 2011). To fully constrain the methane budgets, sources to and microbial consumption in seawater, it is important to generate concentration profiles of dissolved methane throughout the entire water column. Here, we describe a simple and rapid method to measure methane in discrete water samples using ICOS technology, which allows for results to be generated in the field shortly after sampling. Furthermore, as this instrumentation can also generate air and surface seawater measurements with minimal modification, a complete depiction of methane in ocean/atmospheric system can be obtained.

MATERIAL AND PROCEDURES

Material

Analyses by GGA require a total gas volume of 140 ml. Therefore, we used 140 ml plastic syringes with a rubber plunger head (Monoject™) for sample collection at sea, where these syringes were filled directly from Niskin bottles. Small water bodies on land were sampled directly from shore. The syringes were each attached to a one-way valve to close them and we used a 22-gauge needle (e.g. Hamilton SN 7751-13) for sample processing.

Methane free synthetic air (known as 'Zero Air') is required for measurement procedure and various gas standards for calibration of the ICOS. Zero Air is available from Air Liquide (Germany) as ALPHAGAZ_1 in 200L or 50 L tanks or as N12, in small (12L) pressured portable canisters. We used three methane standards with different concentrations for the calibration of the analytical instrument (1, 10 and 100 ppm). The 1 ppm and 10 ppm standards were supplied by Air Liquide as custom-made products (Chrystal gases), these have to be purchased in larger quantities (min. 10L) but can be requested in small canisters

Analyses were done by off-axis integrated cavity output spectroscopy (ICOS), using the Greenhouse Gas Analyzer (GGA- 'Enhanced Performance' with 'Syringe Injection Mode') from Los Gatos Research (LGR), California. The instrument uses conventional Laser Absorption Spectroscopy, where the absorption of the infrared laser beam directed through the sample is used to calculate the mole fraction of methane in the gas. The use of high reflectivity mirrors in the absorption cell enlarges the optical path length by thousands of meters and thus the measured IR absorption is significantly enhanced [*Baer et al.*, 2002]. A small vacuum pump and the required tubing are included in this set up, additional septa for the injection port have to be ordered separately from LGR.

Procedure

At sea, water samples are taken with Niskin bottles, either during hydrocasts or using a remotely operated vehicle. Immediately upon recovery, each Niskin bottle is sampled by filling three 140-ml syringes outfitted with a valve. Tygon tubings were used to fill the syringes to avoid potential water degassing induced by turbulence during sampling. The syringes were flushed and filled with exactly 100 ml of seawater without any air bubbles. Two syringes were used for the analysis, and the remaining one was saved as a spare.

For analyses of methane in water streams or ponds, samples can be collected directly on 140-mL syringes, and transported to the lab for immediate analyses. To test the reproducibility of the method in fresh water, we collected up to 10 L of surface water from a peat channel in Bremen, Germany. Subsamples in 140-ml plastic syringes were taken within 10 minutes of collection.

After water collection either from Niskin or surface waters, the syringes were left to equilibrate to room temperature for at least 30 minutes and room temperature and ambient pressure were noted at the beginning of the analytical run. In some cases the samples are very cold around 1°C, to avoid a long equilibration time the sample temperature can be taken shortly after the injection. To generate a gas headspace within the syringe 40 ml of Zero Air were drawn from a 200 L gas tank outfitted with a septum port through a needle attached to the syringes. Potential overpressure was released, the valve was closed and the needle was removed. The procedure was repeated for the second syringe. Both syringes were shaken vigorously for over 1.5 minutes to allow for equilibration between water and headspace [*Magen et al.*, 2014]. To minimize the risk of water injection into the GGA instrument chamber the 40 ml headspace gas each from both syringes were collected in a gas tight 100 ml glass syringe via a Luer Lock adapter and the

combined gas volume of 80 ml was injected in the GGA. This was followed immediately by 60 ml injection of Zero Air, as needed to reach the required volume of 140 ml in the instrument chamber of the GGA. Each analytical run took 5 minutes, during which more than 100 readings were acquired.

Calculations

Each GGA run collects around 104 measurements, which are stored in a text file that can be downloaded directly from the instrument. The GGA calculates methane concentrations based on its internal calibration. Because water vapor interferes with the CH_4 concentration by diluting the mixing ratio in air and by broadening the spectroscopic absorption lines [*Rella et al.*, 2013; *Welp et al.*, 2013] the water vapor content of the gas sample is automatically determined and methane concentrations are corrected accordingly and reported as dry methane. To minimize potential errors caused by shifts in the internal calibration of the instrument we ran calibration curves at the beginning of each day, where 30–40 samples were analyzed (see assessment section). A small application with web-installer named TICOSES using the MATLAB Compiler Runtime environment, extracts the measured data (methane, water vapor, carbon dioxide) and relevant parameters (gas pressure, gas temperature, instrument ambient temperature, ringdown time of both lasers) as well as derived variables (methane dry, carbon dioxide dry). Further calculations like the mean concentration and the standard deviation are also performed by the software, stored in two data tables. TICOSES with MATLAB Runtime web-installer is given in the supplemental material. Calculation of the dissolved methane concentration in the samples used the corrected dry methane values, the atmospheric ambient pressure, the water sample volume and the volume of injected gas.

Calculations are based on the headspace formulation detailed in Magen et al., (2014).
Briefly:

$$n_{CH_4} = n_{CH_{4W}} + n_{CH_{4HS}} \quad \text{(Eq. 1)}$$

$$[CH_4]_{GGA} = n_{CH_4}/V_W \quad \text{(Eq. 2)}$$

where nCH_4 is the sum of moles of methane in the water and the headspace gas. To calculate the methane concentration in the water sample after equilibration, the atmospheric ambient pressure and the Bunsen coefficient were used, which required knowledge of salinity and temperature of the sample to define the solubility of methane [*Yamamoto et al.*, 1976]. The methane concentration in the GGA ($[CH_4]_{GGA}$) was calculated using the volume of water in the syringes (V_W). Because of the need to dilute the headspace

with a volume of Zero Air in the instrument chamber, the final methane concentration is corrected with the dimensionless dilution factor, such that the methane concentration in the sample ($[CH_4]_{smp}$) is given by

$$[CH_4]_{smp} = [CH_4]_{GGA} \times 140/V_{HS} \quad \text{(Eq. 3)}$$

where V_{HS} is the volume (in ml) of headspace gas injected and 140 is the total gas volume in ml injected in the GGA chamber.

ASSESSMENT

Analytical range

Supplier's specifications indicate a linear instrument response of the GGA in concentrations ranging from 0.01 to 100 ppm. The method described here takes advantage of this broad range to measure dissolved methane in samples over an extremely wide concentration range (1.5 to 65,000 nM), with minimal modifications to the sample protocol. This allowed us to analyze water samples in the water column directly above methane seep areas, where concentrations range by 3 orders of magnitude within one hydrocast. The only constraint to the dynamic range is that the instrument requires 140 ml of gas for each run. The protocol described above (80 ml headspace diluted with 40 ml of Zero Air) is optimal for typical low seawater concentrations, which have methane concentrations of 2–5 nM (e.g. Bange et al. 1994; Tsurushima et al. 1996; Valentine 2011). For samples above 3,200 nM methane, different headspace to Zero Air ratios can be used. For example, for very high methane concentrations (>5µM), we injected 10 ml of headspace gas using a smaller glass syringe and 130 ml Zero Air. If the volume of the water sample is reduced to 70 ml and 70 ml of headspace gas are added, a maximum of 65 µM methane can be detected.

Instrument response

The instrument precision, calculated as the relative standard deviation of 80 analytical runs is 0.067%. The linearity of the GGA response is shown in Figure 9. We used dilutions of three stock standards (1, 10 and 100 ppm methane) and generated calibration curves ranging from 0.07 to 100 ppm. For the lower concentration range (0.07–10 ppm) the GGA responded linearly with an R^2 of *0.9999* and a slope of 0.90. However, for concentrations exceeding 10 ppm, we used a second calibration curve, with a linear response $R^2 = 0.9992$, but with a different slope of 0.71, which could be due to using various standards.

Our results show that the use of Zero Air to dilute headspace sample within the instrument chamber, followed by GGA analyses, yields data with precision better than 2.4% (Table 1).

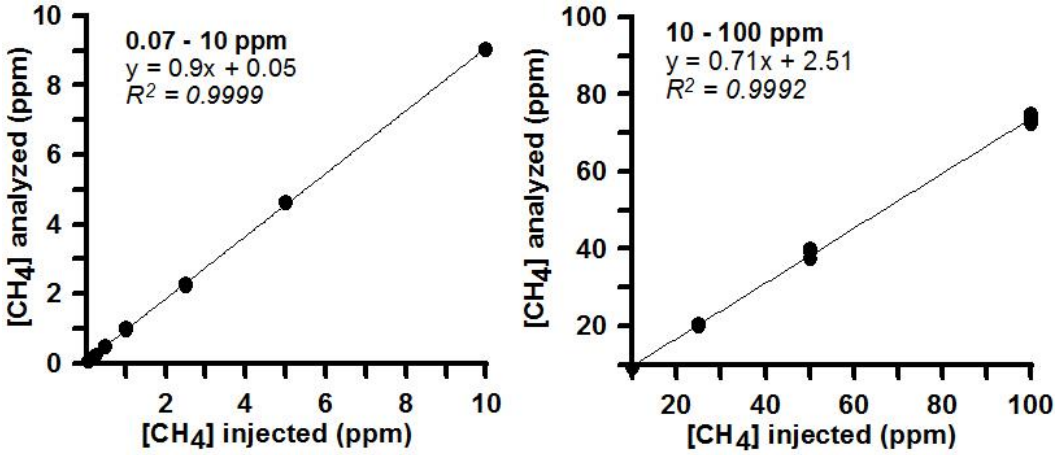

Figure 9: Response of GGA using dilutions of three (1, 10, 100 ppm) stock Air Liquid standards. The graph is separated in two axes for CH_4 concentrations ranging from 0.07–10 ppm and 10–100 ppm. The 100 ppm standard yields a different slope compared to the values obtained using the lower stock concentrations, therefore, we chose two different calibration curves.

Limit of detection

The limit of detection (LOD) was calculated after Currie (1968) using the formula:

$$LOD = 3.29 \times \sigma_{blank} \qquad (4)$$

where σ represents the standard deviation of blank injections, for which we use 140 ml of Zero Air. The LOD obtained (n = 33) is 0.0068 ppm methane. This concentration is not significantly different from the lowest threshold of the GGA, reported to be 0.01 ppm from the supplier, and reflects potentially methane content of the Zero Air used. Therefore, there is no need to use Zero Air of higher purity. The lowest methane concentration we analyzed in seawater is ~2 nM; using 200 ml of seawater, an injection volume of 80 ml headspace gas and 60 ml Zero Air, yields $[CH_4]_{GGA} \geq 0.05$ ppm, and therefore, clearly is within the detection range of the instrument.

Table 1: Reproducibility of syringe injections using a 1 ppm, 10 ppm and 100 ppm methane standard gas and various mixing ratios with Zero Air, mixing ratio is represented in the injected standard gas volume (V_S) and the volume of Zero Air (V_{ZA}). Precision was calculated on the basis of standard deviation divided by the mean of each analyzed CH_4 concentration.

CH_4 injected [ppm]	V_S [ml]	V_{ZA} [ml]	Number of samples	CH_4 analyzed [ppm]	Precision [%]
0.07	10	130	6	0.07	2.34
0.25	35	105	6	0.24	1.22
0.5	70	70	10	0.49	1.78
1.0	140	-	28	0.97	1.42
2.5	35	105	7	2.26	1.15
5	70	70	8	4.63	0.38
10	140	-	17	9.06	0.14
25	35	105	8	20.42	1.54
50	70	70	13	39.38	1.79
100	140	-	41	73.57	0.90

Precision of the Headspace-GGA technique

We tested the reproducibility of our method in both fresh and seawater samples. Water from the freshwater peat channel 'Am Fleet' (Bremen, Germany) was collected in large volumes (~10 L) during the summers of 2014 and 2015, which were subsampled and analyzed immediately after collection at the nearby University of Bremen. Repeated seawater measurements were conducted onboard the research vessel RV METEOR using water samples collected in the Gulf of Mexico above hydrocarbon seeps (Table 2). Repeated analyses (n= 26) yield a precision <2.5%. Am Fleet in 2015, when various operators conducted analyses during training with freshwater samples a precision of 2.1% was reached. This is also reflecting the ease of use and reliability of the method.

Table 2: Precision reported as the mean of relative standard deviation of repeated methane measurement using different methods, and samples with different salinities and concentration ranges.

Site	Salinity [psu]	Number of samples	Concentration range CH_4 [nM]	Precision [%]
Headspace - Greenhouse Gas Analyzer				
Am Fleet '15	0	43	980–3200	2.10*
Gulf of Mexico	35	18	4–82	2.50
Gulf of Mexico	35	8	111–243	2.39
Vacuum Extraction - Gas Chromatography				
Gulf of Mexico	35	3	62–70	5.87
Gulf of Mexico	35	3	225–274	10.84

*various operators

Sample storage

This method was developed for rapid and accurate analysis of dissolved methane concentrations in the field. The sampling described here, using plastic syringes, was deemed accurate over minimum 2-hour time-series. Duplicates of samples were analyzed after 1,2, 14 and 20 hours, significant loss of methane in the plastic syringe of 20% was observed after 14 hours (Figure 10). We did not consider long-term storage as part of this study, since Magen et al. (2014) have provided a detailed report of sample preservation with KOH and NaOH for analyses up to one year after sample collection.

Because the instrument is small and requires no carrier gas, it is relatively easy to transport to the field. Standards and Zero Air canisters are available for ease of transportation. If analyses in the field cannot be achieved, headspace gas samples can be obtained with the new technique described here and be stored in 100-ml glass bottles filled with saturated NaCl solution, and transported to the lab for later analyses. Alternatively, water samples can be collected in 200 ml glass vials equipped with a septum and preserved with NaOH for shore-based gas extraction and GGA analyses.

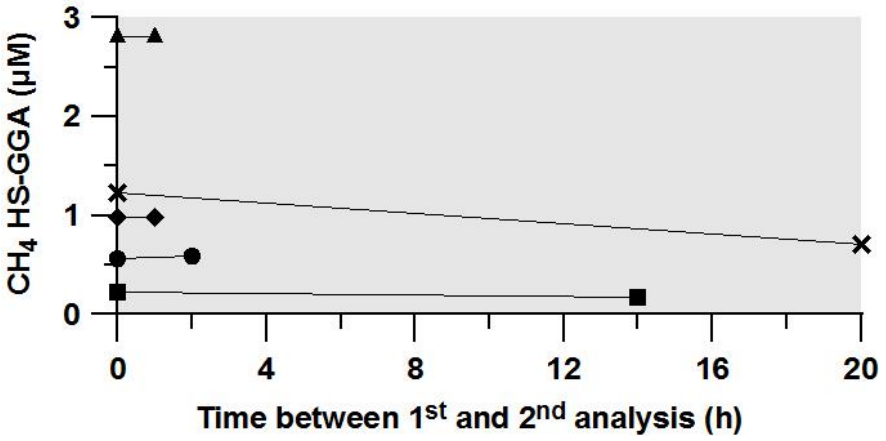

Figure 10: Repetition of samples using the HS-GGA method showing methane concentration of duplicate samples analyzed after different time steps.

Comparison with Vacuum Extraction method

We took advantage of two research expedition onboard FS METEOR to compare our method with the Vacuum Extraction method after Lammers and Suess (1994) modified after Rehder et al. (1999) and Keir et al. (2005, 2009). This technique extracts gas compounds from water using vacuum. Briefly, 700 to 750 mL of seawater are directly collected from Niskin bottles into pre-evacuated ($1x10^{-3}$ mbar) 1L-glass bottles (Schott DURAN), which have a gas tight closure. The gas dissolved in the sample is separated from the water by high-grade vacuum extraction in the bottles. The extracted gas can be transferred with a gas-tight syringe through a septum port in the extraction system into a 20 ml serum glass vial pre-filled with saturated NaCl solution. These gas samples were analyzed for methane concentration with a gas chromatograph using a Flame Ionization Detector and/or can be used for characterization of stable carbon isotope composition [*Pape et al.*, 2010b].

Drawbacks of this traditional method are securing vacuum and the necessity of more equipment for extraction of the gas. The potential for error using the vacuum extraction method is high because of the number of technical steps involved and the need to ascertain full vacuum of $1x10^{-3}$ mbar in the glass bottles, which was not always achieved or got lost over time as bottles leaked. We tested the reproducibility of the Vacuum Extraction method analyzed with the gas chromatograph (VE-GC) using triplicate samples, which yield precision values of 5 to 10% (Table 2). The vacuum technique also requires significantly more equipment (vacuum pumps, glass bottles, stop cocks, magnetic stirrer, glass valves and tubing etc.), that needs a lot of space and is partly quite expensive.

For the comparison with the HS-GGA method some water samples were analyzed with the VE-GC method, and shown as discrete grey symbols in Figure 11. In all cases, both methods yield the same trend, with partly indistinguishable variations given the large concentration ranges encountered. Interestingly, in some cases the concentration measured using the VE-GC method was lower than that detected with the HS-GGA, indicating incomplete extraction with the vacuum approach.

But for background samples with concentrations <5nM, methane concentrations determined with the HS-GGA were constant between 1.1 and 1.9 nM whereby the values analyzed with the VE-GC approach revealed higher concentrations around 3.5 nM methane. The reason for higher values detected with the VE-GC method could be contamination with atmospheric air, e.g. due to a poor vacuum in the bottle.

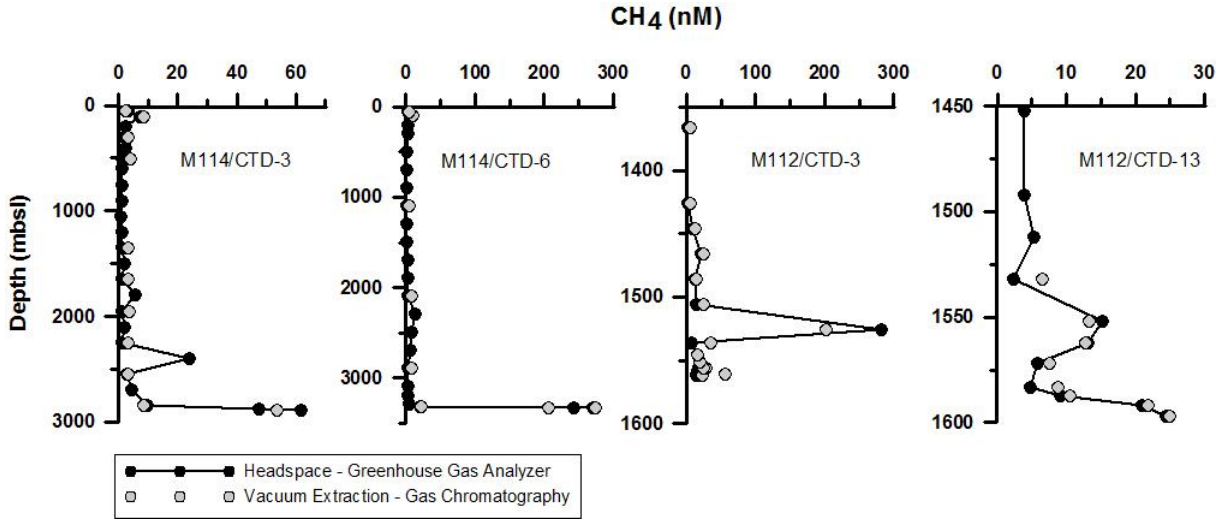

Figure 11: Vertical concentration profiles of dissolved methane in the water column using the HS-GGA method (black symbols) and the VE-GC (grey symbols) obtained for ship stations performed during cruise M112 and M114.

Field results

The field results presented here were compiled from different settings and are supposed to provide examples of the usage of ICOS. First we cover field data of the marine realm and then freshwater settings. As already mentioned above, during expeditions, M112 and M114 with RV METEOR (Bohrmann et al. 2014), water samples were collected for methane analyses using the HS-GGA approach to test the handling of the equipment. Both cruises had

the objective to characterize methane released from the seafloor. Therefore, sampling was guided by observation of gas flares during hydroacoustic surveys, such that targeted hydrocasts were conducted as close as possible to the seepage sites. The majority of the analyses were conducted with the HS-GGA method, because of its large analytical range and ease of use. Furthermore, the HS-GGA method was found to be more reliable due to a better reproducibility and an entire hydrocast of 24 samples was analyzed in 3–4 hours, including calibration curve and a few duplicate runs. Examples from four hydrocasts are shown in Figure 11. High methane concentrations (30–300 nM) were found near the seafloor. Plumes in the water column were also detected, with maximum concentrations reaching over 250 nM in the vicinity of mud volcanoes in the Mediterranean. Freshwater samples from the channel 'Am Fleet' were analyzed using the HS-GGA technique in September 2014 and July 2015 (Figure 12) to test the reproducibility and to investigate potential correlation between environmental conditions e.g. rain fall and methane in the system. In this case the methane concentrations were higher, thus, only one syringe filled with 100 ml water was used for the analysis and 40 ml headspace were injected diluted with 100 ml Zero Air. In 2015, at least 5 sample repetitions were taken, and precision was always better than 2.5%, error bars are within the symbol and therefore, not displayed in Figure 12. The detected concentrations varied between 0.2 and 3.2 µM methane. The vertical bars in Figure 4 indicate the air temperature and precipitation height on each day representing environmental conditions during sampling (Deutscher Wetterdienst, http://www.dwd.de, July 2015). No correlation between rainfall and temperature could be observed. Discussion of reasons for observable change in methane concentration and variability is out of the scope of this publication.

An advantage of using the GGA is that it allows for simple way to also obtain air methane concentrations [*Baer et al.*, 2002; *Berman et al.*, 2012]. Our measurements of methane in air samples collected in Bremen during our field experiments, yield concentrations ranging from 0.08 to 0.09 µM, indicating the extreme methane super saturation of the peat channels, which undoubtedly constitute a significant methane source to the atmosphere.

DISCUSSION

We set up and tested a method using GGA for discrete syringe injections to rapidly and accurately analyze dissolved methane in discrete water samples. It was initially developed to analyze dissolved methane in water samples taken from deep sea hydrocasts using Niskin bottles, available in almost all research vessels. But as shown, the technique can be

easily adapted for analyses of water samples from a variety of settings including lakes, aquifers, ponds and estuaries. The reproducibility of the method yield excellent results with values better than 2.5% for different concentrations ranging from 4 to 3200 nM and in samples with salinities ranging from 0 to 35 psu. The precision of the method compares very well with the reported values between 3.3% and 6.8% using headspace equilibration followed by GC injections [*Yoshida et al.*, 2011; *Magen et al.*, 2014; *Capelle et al.*, 2015] and with the precision of 5–10% achieved with the VE-GC method in this study.

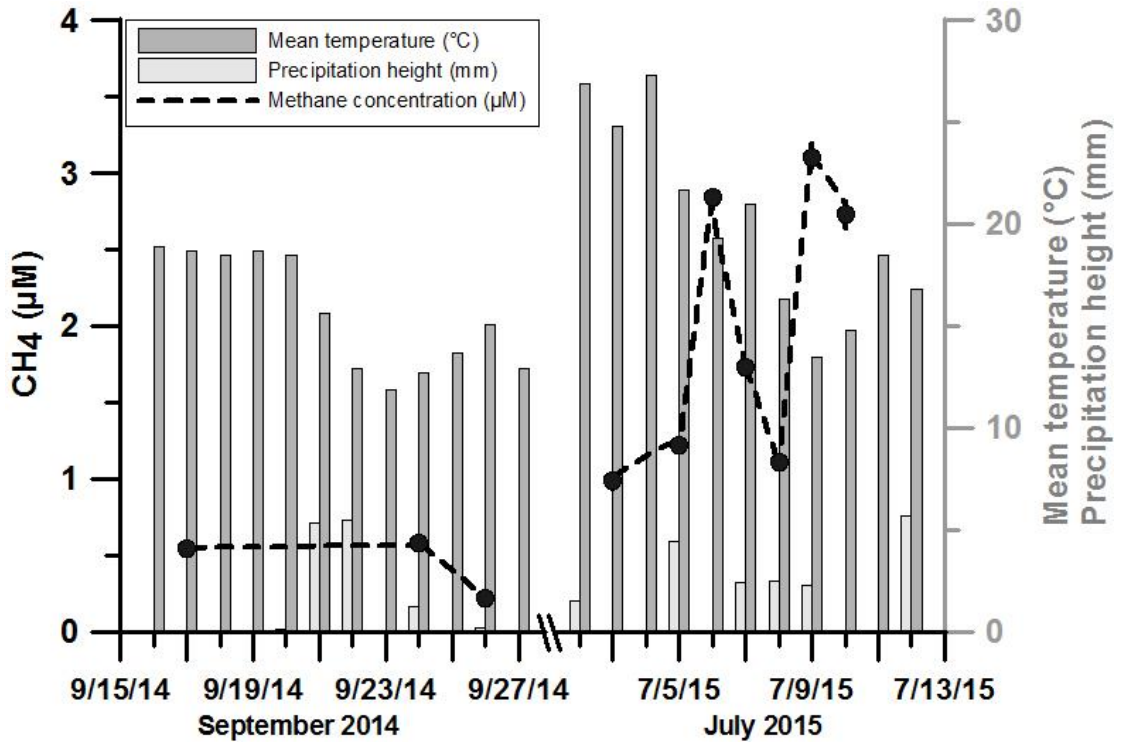

Figure 12: Methane concentration of freshwater channel 'Am Fleet' showing different concentration over time (black dots). Error bars are within the symbols and represent good reproducibility of repeated measurements of minimum 5 samples taken once a day. Dark grey bars and light grey bars indicate daily mean air temperature and precipitation height, respectively.

Reported extraction efficiency for the Vacuum Extraction is 90±6% [*Keir et al.*, 2005, 2009] and, regarding the comparison in Figure 10, the mean outcome from our method is 17 % higher than that for the VE-GC method. The described HS-GGA method using two 140-ml syringes for each sample is appropriate for low methane concentrations, including background seawater values from which methane values in the GGA are an order of magnitude higher than the limit of detection. For higher concentrations, e.g. at gas seepage sites, the range can be easily extended using different volumes of water, headspace and

Zero Air. This flexibility allows for methane measurements in most marine and terrestrial settings where dissolved methane concentration is of interest.

For the VE-GC all sample bottles have to be evacuated before sampling and vials have to be prepared for sample storage. Both technical steps are relatively time-consuming. Using the headspace method after Magen et al. (2014) samples have to be fixated using chemicals. The shipping and transport of chemicals is always complicated and furthermore, the addition of the NaOH or KOH is another and laborious working step which has to be done after sampling. This work is not necessary for the simple determination of methane concentration. However, if the methane concentration in the samples should be sufficient for conventional isotopic analysis (e.g $\delta^{13}C\text{-}CH_4$, $\delta^{2}H\text{-}CH_4$) the Vacuum Extraction method should be considered because methane is not diluted in a headspace. For samples which have to be stored for a longer period the headspace method after Magen et al. [2014] is recommended.

The off-axis ICOS technology was originally developed for continuous measurements of air. Since its introduction it has proven useful for continuous analyses of dissolved methane in surface waters using an equilibration set up. With the addition of the method we describe here to measure discrete samples collected in the water column, the field of application for the GGA is enormous. For example, at seepage sites vertical profiles in the water column can be conducted taking discrete samples. The methane concentration in the surface waters above the seepage system can also be analyzed to generate horizontal transects and these values can be compared with methane concentration in the air above the study site. CO_2 concentrations, which are not considered in this study, can also be determined with this instrument. This capability extends the application of the ICOS technology for another important greenhouse gas.

COMMENTS AND RECOMMENDATIONS

The Greenhouse Gas Analyzer is easy to install and use, no carrier gas is needed, and allows for field-based analyses of methane over a wide range of concentrations. Field measurements have the advantage of providing immediate results that can guide subsequent sampling and field experimental strategies.

The utilization of syringes with movable piston as sampling devises prevents development of over pressurized headspace. In contrast with the use of vials that require pressure compensation during subsampling, the plunger in the syringe and the valve allow for easy

adjustment of the pressures during headspace transfer. We note that small bubbles, which appear in the syringe before shaking, might get lost due to pressure compensation but potential loss of methane was proved to be insignificant by repeated analyses.

Preparation of the sample for injections, including addition of headspace gas, shaking and transferring the gas into the injection syringe, can be done while the instrument analyzes the previous sample (~5 minutes total), so that a mechanical shaker would not necessarily improve efficiency of analyses.

ACKNOWLEDGEMENTS

This study was financed by the U.S. Department of Energy Grant #DE-FE00135331. In addition, we acknowledge support through DFG Research Center / Cluster of Excellence "The Ocean in the Earth System". We thank the captain and crew members during expeditions M112 and M114 of the R/V Meteor for their outstanding support at sea, and Stefanie Buchheister for her excellent laboratory assistance both at sea and onshore.

CHAPTER 3: CASE STUDY 1: SEEPAGE IN ANTARCTICA

CARBON CYCLING FED BY METHANE SEEPAGE AT THE SHALLOW CUMBERLAND BAY, SOUTH GEORGIA, SUBANTARCTIC

Patrizia Geprägs[1], Marta E. Torres[2], Susan Mau[1], Sabine Kasten[1,3], Miriam Römer[1], Gerhard Bohrmann[1]

submitted in Geochemistry, Geophysics, Geosystems

[1]MARUM – Center for Marine Environmental Sciences and Department of Geosciences, University of Bremen, Klagenfurter Str., 28359 Bremen, Germany
[2]College of Earth, Ocean, and Atmospheric Sciences, Oregon State University, 104 CEOAS, Administration Building, Corvallis, OR 97331-5503, USA
[3]Alfred Wegener Institute, Helmholtz Centre for Polar and Marine Research, Am Handelshafen 12, 27570 Bremerhaven, Germany

Keywords:
Methane seepage in the Southern Ocean with almost no impact to the atmosphere
AOM is the major sink for methane in sediments
Strong isotopic fractionation around the sulfate-methane interface (SMI)

ABSTRACT

Recent studies have suggested that the marine contribution of methane from shallow regions and melting marine terminating glaciers may have been underestimated. Here we report on methane sources and potential sinks associated with methane seeps in Cumberland Bay, South Georgia's largest fjord system. The average organic carbon content in the upper 8 meters of the sediment is around 0.65 wt.%; this observation combined with Parasound data suggest that the methane gas accumulations probably originate from peat-bearing sediments currently located several tens of meters below the seafloor. Only one of our cores indicates upward advection; instead most of the methane is transported via diffusion. Sulfate and methane flux estimates indicate that a large fraction of methane is consumed by anaerobic oxidation of methane (AOM). Carbon cycling at the sulfate-methane interface (SMI) results in a marked fractionation of the $\delta^{13}C\text{-}CH_4$ from an estimated source value of -65‰ to a value as low as -96‰ just below the SMI. Methane concentrations in sediments are high, especially close to the seepage sites (~40 mM); however, concentrations in the water column are relatively low (max. 58 nM) and can be observed only close to the seafloor. Methane is trapped in the lowermost water mass, however, measured microbial oxidation rates reveal very low activity with an average turnover of 3.1 years. We therefore infer that methane must be transported out of the bay in the bottom water layer. A mean sea-air flux of only 0.005 nM/m^2s confirms that almost no methane reaches the atmosphere.

INTRODUCTION

Methane is an important greenhouse gas, whose atmospheric concentration has increased by a factor of 2.5 since preindustrial times [*IPCC*, 2013]. Because its radiative forcing relative to CO_2 is ~21 times higher, atmospheric methane levels play an important role in climate models [*Badr et al.*, 1991], which estimate a global warming potential of methane to be 86 times that of CO_2 in the next 20 years [*IPCC*, 2013]. Even though the oceanic methane source is thought to be small, there is evidence suggesting that the marine contribution from shallow regions may have been underestimated [*Hovland et al.*, 1993; *McGinnis et al.*, 2006; *Mau et al.*, 2015]. This is particularly true at high latitudes where the effects of climate change are amplified [*Walter et al.*, 2006; *Archer et al.*, 2009; *Carlson*, 2013], and methane release from permafrost [*Christensen*, 2004; *Schuur and Bockheim*, 2008], gas hydrate dissociation [*Jung and Vogt*, 2004; *Mienert et al.*, 2005], and sea ice melting [*Walter et al.*, 2006; *Damm et al.*, 2015] have all been put forward as possible factors that might accelerate methane release to the atmosphere. Most of these high-latitude studies have been conducted in the Arctic, and so far only little is known about methane dynamics in the Southern Ocean [*Heeschen et al.*, 2004; *Römer et al.*, 2014a].

Römer et al. [2014a] report on the first observation of widespread seepage in the Southern Ocean, via hydroacoustic mapping of methane release on the northern shelf of South Georgia. The 133 instances of detected flare activity are restricted to the fjords and glacial troughs along the shelf. The authors also suggest that natural seepage in the Southern Ocean might be more common than previously expected due to high organic matter input to shelf areas around Antarctica that are also influenced by glaciers [*Schlitzer*, 2002; *Wadham et al.*, 2012; *Murphy et al.*, 2013].

This study follows on the work of *Römer et al.* [2014a] with a detailed look into the carbon source and its sinks associated with the reported flare activity in the Cumberland Bay, South Georgia's largest fjord system. For this purpose we discuss biogeochemical methane-related processes in the sediments, the fractionation of the stable carbon isotopes of methane during its rise from the source to the seafloor, the fate of methane in the water column and possible escape into the atmosphere.

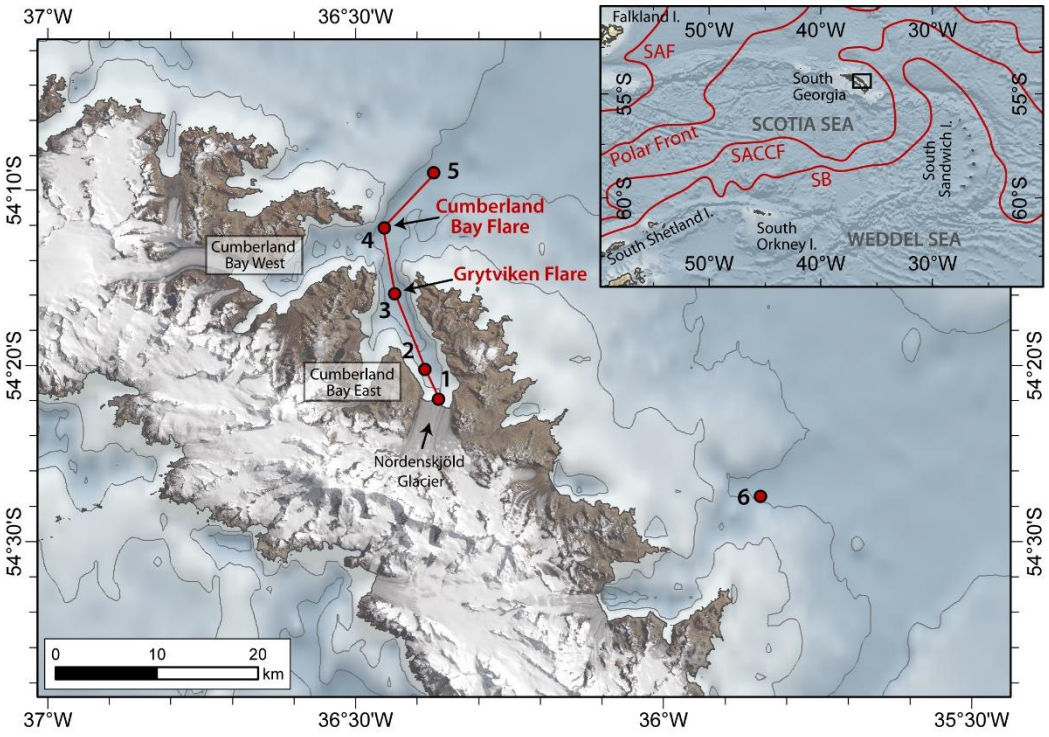

Figure 13: Study area in Cumberland Bay East on South Georgia. All six stations are marked by a red circle. The transect is shown from station 1 to station 5, which sampled two major flare sites: Grytviken Flare and Cumberland Bay Flare. Inset shows schematic locations of the ACC fronts across the Scotia Sea, adapted from Orsi et al. [1995] and Murphy et al. [2004]. Fronts are (north to south) the Subantarctic Front (SAF), the Polar Front, the Southern ACC Front (SACCF), and the Southern Boundary of the ACC (SB).

STUDY SITE

The Island of South Georgia is an isolated microcontinental block in the NE of the North Scotia Ridge [*Cunningham et al.*, 1998], which lies 350 km south of the Antarctic Polar Frontal Zone (Figure 13 inset; [*Orsi et al.*, 1995; *Murphy et al.*, 2004]). The South Georgia Mountains are heavily glaciated with series of ice fields feeding glaciers that most commonly terminate in the ocean via steep sided bays and U-shaped fjords (Figure 13). The bays and fjords dissect the coastline to the north and south of the island and extend into major glacial cross-shelf troughs [*Graham et al.*, 2008], with a consistent pattern of glacial features such as moraines and inner sediment basins [*Hodgson et al.*, 2014].

Cumberland Bay, situated centrally on the northern shoreline of South Georgia, is the largest of the bays on the island and is divided into a western and eastern section. Cumberland Bay East is approximately 35 km long, 15 km wide and up to 270 m deep. Two moraines are present in the east segment of the bay: the inner basin moraine corresponds to the last glacial advance during the last glacial maximum (> 18.6 ka), and the outer basin

moraine is correlated to marine isotope stage 6 (MIS6) [*Hodgson et al.*, 2014]. The outer basin moraine is more pronounced than the inner moraine, with a sill depth of ~ 100 meters that limits circulation with the surrounding ocean waters.

The general ocean circulation around South Georgia is dominated by the eastward flow of the Antarctic Circumpolar Current (ACC) (Figure 13). The Subantarctic Front (SAF) and the Polar Front are located to the north of the island, and the Southern Antarctic Circumpolar Front (SACC) lies immediately south [*Ward et al.*, 2002; *Meredith*, 2003a; *Murphy et al.*, 2004]. A prominent water mass around South Georgia is the Antarctic Surface Water AASW, which extends from Antarctica to the Polar Front [*Orsi et al.*, 1995]. Flowing beneath the AASW, the Circumpolar Deep Water CDW is commonly divided into the Upper CDW (UCDW) and the Lower CDW (LCDW) [*Orsi et al.*, 1995; *Meredith*, 2003b].

Oceanographic conditions around South Georgia result in a rich ecosphere and large phytoplankton plumes [*Whitehouse et al.*, 1996; *Korb et al.*, 2004] that are particularly intense on the northern shelf area of South Georgia and in the Georgia Basin [*Borrione and Schlitzer*, 2013]. Enhanced supply of iron from the island and rapid recycling of nitrogen provide a good base, which in the presence of a shallow stable stratification created by seasonal warming and local inshore conditions result in large phytoplankton blooms [*Atkinson et al.*, 2001].

Cores recovered during the RV POLARSTERN cruise ANT-XXIX/4 in March/April 2013 from the Cumberland bay fjord consist of muds to sandy muds. Sediment color varies between black or dark green to grey and some have evidence of bioturbation. In general the sediments display a homogenous lithology [*Bohrmann*, 2013]. Total organic carbon contents measured at a site close to the so-called Grytviken Flare in the Cumberland Bay East fluctuate around 0.65 wt.%.

MATERIAL AND METHODS

To characterize the methane system fed by seeps in Cumberland Bay, we analyzed sediment and water samples collected from 6 stations during RV POLARSTERN cruise ANT-XXIX/4 in March/April 2013 (Figure 13, [*Bohrmann*, 2013]).

Methane in sediment samples

Sediment cores were collected using a 10-m-long gravity corer. Three sediment cores were taken within the Cumberland Bay starting with a core close to the glacier (GC 258-1) and two cores close to the main seepage sites (Grytviken Flare GC 284-1, Cumberland Bay Flare

GC 281-2). Another core was taken at station 6 (GC 280-1) located approximately 45 km southeast of the bay area on the northern South Georgia shelf (Figure 13).

Immediately after recovery the cores were cut in one-meter sections. Sediment samples (3 ml) for methane analyses were obtained at every freshly cut surface using cut-off syringes and transferred into 20 mL glass vials prefilled with 5 mL of 1 M NaOH [*Kvenvolden and McDonald*, 1986]. Prior to gas analysis, the samples were kept for several hours at 20 °C and were shaken occasionally. Subsequently, the headspace gas was analyzed onboard for its methane concentration, which was quantified using a two-channel 6890N gas chromatograph equipped with a capillary column and a Flame Ionization Detector (GC-FID) [*Pape et al.*, 2010a]. The instrument was calibrated using commercial standard gases (100 ppm–100% methane in nitrogen). Precision was better than 2.4%.

Headspace samples were also analyzed for the stable carbon isotope ratio ($^{13}C/^{12}C$) of CH_4. The majority of the samples (with methane concentrations of > 0.6 mM) were analyzed using a GC-isotope ratio mass spectrometer (GC-IRMS) at the MARUM in Bremen, with a precision better than ±0.4%. The stable carbon isotopic composition of the upper four CH_4 samples collected at station 4 with GC 281-2 were analyzed by GEO-data (Environmental-Laboratory in 30827 Garbsen – Germany), because the methane concentrations of these samples were too low for the GC-IRMS at MARUM. The samples collected from 38 and 138 cmbsf could be only analyzed once due to their low carbon content. The other sample in 238 cmbsf was analyzed twice and the results agree within 0.5‰. Comparisons of the isotopic composition of those samples reported by both laboratories agree within 0.3‰. In all cases, stable carbon isotopic ratios are reported in δ notation in parts permil relative to the Vienna PeeDee Belemnite (V-PDB).

Pore-water sampling and analyses

Pore water from gravity cores was extracted through holes drilled into the PVC liner of the cores in a 4 °C cold room within 3 hours after core recovery using rhizons (Rhizosphere Research Products) with an average pore size of 0.15 µm according to the procedure described by *Seeberg-Elverfeldt et al.* [2005]. Subsamples taken for the analysis of the stable isotopic composition ($\delta^{13}C$) of dissolved inorganic carbon (DIC) were poisoned with $HgCl_2$. These analyses were conducted at Oregon State University using a Gas-Bench II automated sampler interfaced to a gas source stable isotope mass spectrometer as described in Torres et al. (2005). DIC is allowed to evolve as CO_2 by addition of H_3PO_4. A known volume of dry

CO_2 is transferred to a Finnigan DELTAplusXL mass spectrometer, which integrates the relevant isotope masses (m/z = 44, 45, and 46) as the CO_2 peak enters the source. The precision of the $\delta^{13}C$ measurements based on replicate analyses of a $NaHCO_3$ stock solution is better than ±0.1‰. Unfortunately, the alkalinity titrator did not work properly during the cruise, therefore, we report estimates of DIC concentrations based on the voltage peak obtained during $\delta^{13}C$ measurements, also calibrated against analyses of a $NaHCO_3$ stock solution. Precision of the DIC concentrations determined by this technique is ~4%.

Pore-water sulfate concentrations were analyzed at the Alfred Wegener Institute (AWI) in Bremerhaven using a Metrohm Ion-Chromatograph Compact IC 761. Pore-water samples were diluted 1:50 and analyzed by column separation and the resulting change in conductivity.

We use Fick's first law [*Berner*, 1980] to estimate diffusive fluxes of SO_4^{2-}, DIC and CH_4 towards the sulfate-methane interface (SMI), also known as sulfate-methane transition (SMT), a reaction zone where these two metabolites get depleted [*Niewöhner et al.*, 1998; *Borowski et al.*, 1999; *Paull et al.*, 2000], as:

$$J = -\varphi \cdot D_s \cdot dC/dz \qquad \text{(Eq. 1)}$$

where J is the diffusive flux (mmol/m²a), φ is the assumed sediment porosity of 0.7 and D_s is the sediment diffusion coefficient for each parameter. D_s was calculated after *Boudreau* [1997], where $D_s = D_0/\theta$, with a porosity-deviated tortuosity (θ) of 1.71. We used the seawater diffusion coefficients (D_0), which are 4.64E-10 m²/s for SO_4^{2-}, 4.81E-10 m²/s for DIC/HCO_3^- and 7.29E-10 m²/s for CH_4 [*Schulz*, 2000].

The concentration gradient is given by the pore water concentration (dC) in mmol and the sediment depth (dz) in cmbsf.

Water column

Hydrocasts were carried out using the ship's Sea-Bird Electronics, Inc. SBE911plus (Sea-Bird Electronics) CTD, which records salinity, temperature, pressure and dissolved oxygen online. The unit was mounted on a carousel with 24x12 L water sampling bottles. Collected water samples were subsampled for dissolved methane, methane oxidation rates and $\delta^{18}O$ analysis of seawater. From total four hydrocast stations in this study, three were located within the Cumberland Bay and one (CTD 286-1) immediately outside the bay. Within the Cumberland Bay station 1 was situated closest to the Nordenskjölk Glacier with CTD 282-1

and the other two CTDs were located close to the main seepage sites (Grytviken Flare: CTD 284-3, Cumberland Bay Flare: CTD 281-1) (Figure 13).

Methane concentrations were obtained using a modification of the Vacuum Extraction method of *Lammers and Suess* [1994]. Briefly, we collected 700 to 750 mL of seawater directly from Niskin bottles into pre-evacuated 1 L gas-tight glass containers. The dissolved gas in the pre-evacuated bottles was separated from the water by high-grade vacuum extraction [*Rehder et al.*, 1999; *Keir et al.*, 2009]. The released gas was collected with a gas-tight syringe through a septum port in the extraction system and transferred into 20 ml serum glass vials pre-filled with saturated NaCl solution. Methane concentration in the gas samples was analyzed onboard using a two-channel gas chromatograph 6890N from Agilent Technologies using a Flame Ionization Detector. Precision of this analysis ranges between 5-10%. The stable carbon isotopic composition of two water samples were analyzed after *Damm et al.* [2005], modified after *Popp et al.* [1995] and *Faber et al.* [1998].

Methane oxidation (MOx) rates were determined from ex situ incubations of water samples in 100 mL serum vials. Sampling and incubations were performed as described in Mau et al. (2013). Briefly, duplicate samples were collected and treated with 50 µL of ^{3}H-labeled methane (52 kBq) in N_2. After shaking the bottles to equilibrate the tracer with the water, the samples were incubated in the dark at 4 °C for three days. After incubation, the total activity (^{3}H-CH_4+ ^{3}H-H_2O) in 1 mL aliquot was measured by wet scintillation counting, and the activity of ^{3}H-H_2O was measured after sparging the sample for >30 min with N_2 to remove excess ^{3}H-CH_4. For measurement, the aliquots were combined with Ultima Gold AB scintillation cocktail and analyzed using the Perkin Elmer Tri-Carb 2900TR liquid scintillation counter on board the vessel. MOx rates were then calculated assuming first-order kinetics [*Reeburgh et al.*, 1991; *Valentine et al.*, 2001]:

$$MOx = k' \cdot [CH_4] \quad \text{(Eq. 2)}$$

where k' is the effective first-order rate constant calculated as the fraction of labeled methane oxidized per unit time, and $[CH_4]$ is the in situ methane concentration.

Control samples were frequently taken and poisoned immediately after the addition of the tracer. The mean (x) and SD (s) of all controls sampled during the cruise were calculated and the limit of detection (LOD) was set as:

$$LOD = x + 3s \quad \text{(Eq. 3)}$$

LOD was 0.0006 d^{-1}. The MOx values were also corrected for differences between in situ and incubation temperatures. Replicates differ on average by 17%.

The subsamples for $\delta^{18}O$ were stored without a headspace in 5 ml glass vials. Prior to analyses the samples were equilibrated with carbon dioxide gas for 10 hours and analyzed by dual inlet mass spectrometry using a DeltaPlusXL isotope ratio mass spectrometer at Oregon State University. Data are presented in the typical delta notation ($\delta^{18}O$) versus VSMOW (Vienna Standard Mean Ocean Water). Standard deviation is better than ±0.5‰.

RESULTS

Sediment

The results of the pore-water analyses are ordered along the transect stations of 3 cores (GC 258-1, GC 284-1 and GC 281-2), starting with the core closest to the glacier within the bay and finishing with the core taken outside the bay at station 6 (GC 280-1). The data are listed in the supplementary information (Table S1). The pore-water profiles illustrated in Figure 14 show the concentration profiles of CH_4, SO_4^{2-} and DIC in the left plot of each station and the isotopic composition of CH_4 and DIC on the right plot. The SMI is marked in the plots where both, sulfate and methane are depleted.

Core GC 258-1, retrieved from station 2 close to the marine-terminating Nordenskjölk glacier (Fig. 13), shows very low methane concentrations that range from 0.003 to 0.004 mM. Sulfate is present over the whole length of the core and decreases from 26 mM in the shallowest sample to 6 mM at 663 cmbsf. DIC concentrations slightly decrease downcore from 27 to 9 mM. Low methane concentrations in this core precluded analyses of its isotopic composition. $\delta^{13}C$-DIC range from -11.6‰ in the upper sediment section to -14.6‰ in the lower part of the core.

Methane concentrations in core GC 284-1 retrieved from station 3, close to the position of the Grytviken Flare, are very low in the top 238 cm and show an approximately linear downward increase up to 14.1 mM from 238 cm to the bottom of the core at 830 cmbsf. Sulfate concentrations decrease steadily from 24 mM at the top of the core down to 280 cmbsf, where the SMI is located. DIC concentrations fluctuate between 18 and 42 mM; we observe an increase in the upper 400 cm, below which, DIC concentrations decrease. The most negative values for $\delta^{13}C$-CH_4 can be observed below the SMI, where we obtained a value of -96.7‰ at 338 cmbsf; followed by a downcore increase to -82.4‰. Even if the samples collected from 38 and 138 cmbsf could be only analyzed once by GEO-data due to very low methane concentrations, the sample in 238 cmbsf yields a similar ^{13}C-CH_4 enriched value of -75.8‰, which confirms the strong offset in the $\delta^{13}C$-CH_4 above the SMI.

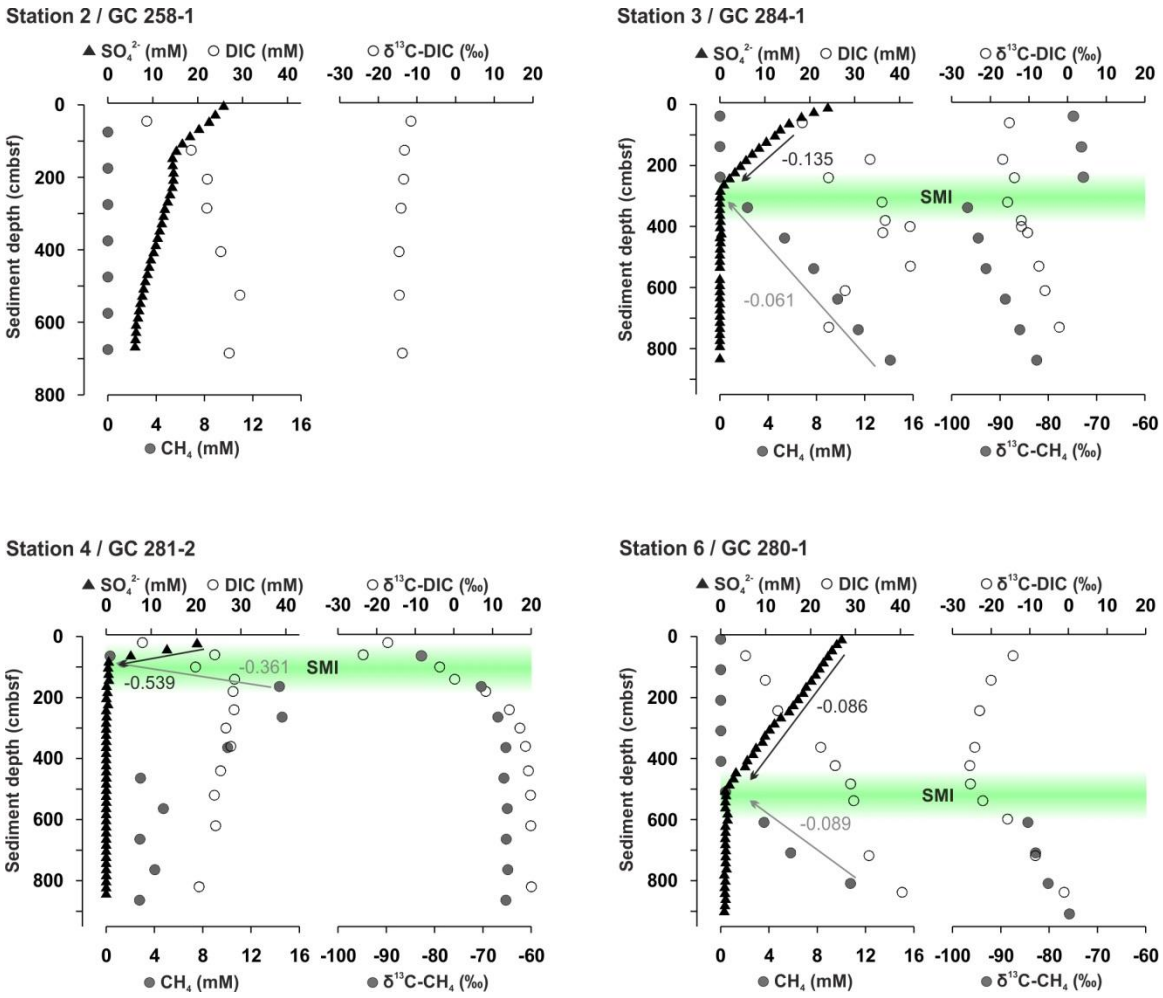

Figure 14: Sediment profiles showing concentrations of SO_4^{2-}, DIC and CH_4 in left panel for each station plot and $\delta^{13}C$ values of CH_4 and DIC in the corresponding right panel. Numbers and arrows denote fluxes towards the sulfate-methane interface (SMI) for methane (grey) and sulfate (black) in mmol/cm^{2}a. (See Figure 1 for sample location and Table 1 for flux data)

The methane concentrations in core GC 284-1 retrieved from station 3, close to the position of the Grytviken Flare, are very low in the top 238 cm and show an approximately linear downward increase up to 14.1 mM from 238 cm to the bottom of the core at 830 cmbsf. Sulfate concentrations decrease steadily from 24 mM at the top of the core down to 280 cmbsf, where the SMI is located. DIC concentrations fluctuate between 18 and 42 mM; we observe an increase in the upper 400 cm, below which, DIC concentrations decrease. The most negative values for $\delta^{13}C$-CH_4 can be observed below the SMI, where we obtained a value of -96.7‰ at 338 cmbsf; followed by a downcore increase to -82.4‰. Even if the

samples collected from 38 and 138 cmbsf could be only analyzed once by GEO-data due to very low methane concentrations, the sample in 238 cmbsf yields a similar ^{13}C-CH_4 enriched value of -75.8‰, which confirms the strong offset in the $\delta^{13}C$-CH_4 above the SMI. The isotopic composition of dissolved inorganic carbon ($\delta^{13}C$-DIC) below the SMI follows the same trend as the stable carbon isotopic composition of CH_4, with an increase from -15.5‰ at 320 cmbsf to -2.1‰ at 730 cmbsf. Above the SMI, where the offset of the isotopic composition of CH_4 is ~23‰, there is no discernable offset in the $\delta^{13}C$ of the dissolved inorganic carbon.

Core GC 281-2, taken at station 4 and located close to the Cumberland Bay Flare, has a low methane concentration of 0.3 mM in the uppermost sediments. Methane concentrations are highest between 164 and 364 cmbsf reaching a maximum of 14.6 mM at 264 cmbsf. In the deeper part of the core methane values fluctuate between 2.8 to 4.7 mM. Sulfate is depleted compared to bottom-water concentrations in the upper meter of the core and then remains below 0.6 mM down to the bottom of the core. The SMI is located at a depth of ~80 cmbsf, which is relatively shallow compared to the other sites. The DIC concentrations steeply increase with depth in the upper meters from 8 to 29 mM and then decrease to 21 at 820 cmbsf. Below 360 cm, $\delta^{13}C$ values are relatively constant and fluctuate around -65‰ for CH_4 and around 19‰ for DIC. This is the only core that shows positive $\delta^{13}C$-DIC values. In the shallow sediment, a shift to lighter $\delta^{13}C$ values towards the SMI is observable for both, CH_4 and DIC.

Methane analyses for core 280-1, taken at station 6 outside the bay area, reveal low concentrations from the seafloor down to 400 cmbsf. Below this depth, methane concentrations increase to a maximum of 10.8 mM. Sulfate decreases linearly from the uppermost sample to 500 cmbsf (27mM to 1 mM); sulfate concentrations below that depth remain lower than 1.5 mM.

DIC concentrations decrease steadily from 5.6 to 40.3 mM. The SMI is located around 503 cmbsf. A decrease in $\delta^{13}C$-DIC values from -14.4‰ to -25.5‰ is observed in the upper 400 centimeters of the core; below 500 cmbsf the $\delta^{13}C$-DIC values increase to -1.1‰. The same trend can be seen in $\delta^{13}C$-CH_4 where the values increase below the SMI from -84.4 to -75.8‰. The estimated diffusive fluxes of SO_4^{2-}, DIC and CH_4 towards the SMI are listed in Table 3. All three parameters reveal the highest fluxes at stations 4 and 3, which correspond to the Cumberland Bay and Grytviken Flare sites presented by *Römer et al.* [2014a] (Figure 13). The lowest fluxes were determined at station 1, where SO_4^{2-} is present over the whole

length of the core. The SMI was not reached with this core; therefore, fluxes into the SMI could not be calculated for this station.

Table 3: Sulfate (SO_4^{2-}), dissolved inorganic carbon (DIC) and methane (CH_4) fluxes of each sediment core towards the sulfate-methane interface SMI in mmol/cm^2a

Station/ GC	SO_4^{2-}	DIC	CH_4
3/ 284-1	-0.135	0.116	-0.061
4/ 281-2	-0.539	0.291	-0.361
6/ 280-1	-0.086	0.095	-0.089

Water samples

Water was collected throughout the water column at four stations along the transect (station 1, 3, 4 and 5). Results from our hydrocast stations are illustrated in Figure 15 starting with the stations closest to the glacier within the bay and moving over the flare sites out of the bay. The depth profiles indicate three different water layers. A layer was designated at the depth where most of the parameters show a clear change. The uppermost layer extends from the sea surface to approximately 25 m, the middle layer extends from 25 m to either 150 m or 200 m, and the bottom layer extends from that depth to the ground. The methane data are listed in the supplementary data (Table S2), and hydrographic data are stored in PANGAEA.

Station 1, located closest to the Nordenskjölk Glacier is our shallowest station with 101 m water depth. Two distinct layers can be observed. The upper 25 meters of the water column indicate slightly cooler temperature (2.35 °C) and lower salinity (33.3) compared to the deeper water. Below 25 m, salinity (~33.8) remains stable and temperature increases to 2.69 °C at 62 mbsl and decreases to 2.5 towards the seafloor. The other parameters remain relatively constant throughout the water column. Oxygen decreases only slightly from 7 to 6.7 ml/L towards the seafloor. No $\delta^{18}O$ data are available of this station. Methane concentrations are relatively low, and range from 3.8 to 8.5 nM. The rate constant (*k*'), which provides an indication of the relative activity of methane oxidizing microorganisms in the water sample, fluctuates between 0.0007 and 0.0019 per day at this station.

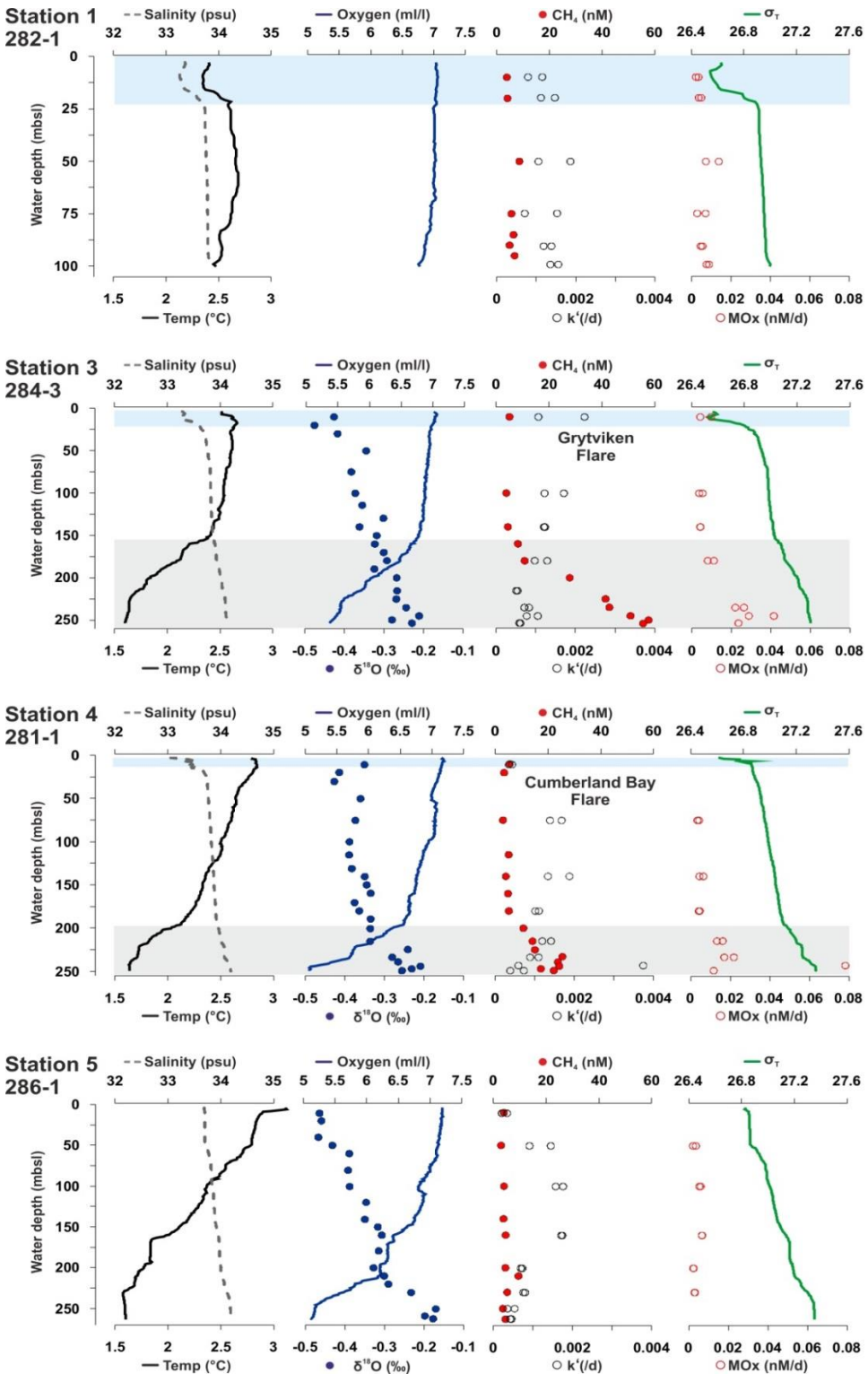

Figure 15: Water column profiles of salinity, temperature and oxygen data for our CTD casts (CTD number mentioned below the station). Oxygen isotopes of water ($\delta^{18}O$), methane concentrations and methane turnover rates (k') were obtained from water samples collected during the casts. The derived variables σ_T and methane oxidation rates (MOx) are plotted in the right panel of each station. Light blue marked areas show freshwater lens produced by glacier melts and the grey areas indicate high methane concentrations associated with a decrease in oxygen and temperature, and a slight increase in density.

At station 3 (Grytviken Flare), three different layers can be observed in the water column. The uppermost layer is solely defined by a salinity minimum of 32.9. Temperature and oxygen decrease slowly from the surface to 160 mbsl - the middle layer, below which there is a faster decline in both parameters (2.3–1.6 °C and 6.7–5.4 ml/L) towards the seafloor. Methane concentrations also show a change at 160 mbsl; the concentrations increase from below 5 nM in the middle layer to 57.7 nM at the seafloor - in the bottom water. The relative activity (*k'*) shows a slight indication of lower values in the bottom water (0.0006 d^{-1}) in contrast to the water above (0.0012 d^{-1}). However, this change occurs not at 160 m, but somewhere between 180 m and 235 m. Oxygen isotopes show a linear increase from the sea surface down to the seafloor (-0.4 to -0.21‰).

At station 4 (Cumberland Bay Flare) also three layers can be identified, the uppermost layer differs again by its lower salinity. Salinity increases in the uppermost 20 meters from 33.3–33.7. The temperature is 2.8 °C; it decreases steadily to 2.0 °C towards 190 mbsl and in the deepest 50 m temperature decreases with a steeper gradient, reaching 1.6 °C at 252 mbsl. The oxygen profile follows the same trend as the temperature curve, a small decrease in the first 190 meters (7.2–6.4) - the middle layer - and then a faster decline down to 5.1 ml/L in the bottom layer. Oxygen isotopes decrease from -0.45 to -0.2‰ towards the seafloor. Methane concentrations are below 5.5 nM for most of the water column, only close to the seafloor values increase to concentrations of 25.4 nM. The relative methanotrophic activity has higher values in the central layer and decreases in the bottom water towards the seafloor.

Station 5 lies immediately outside the Cumberland Bay; it is the deepest station with a water depth of 272 m. A separation into different layers was not done because the transitions appear to be smoother and/or were not observable in most parameters as it was the case at the other sites. There is no salinity minimum in the surface water, salinity slightly increases with water depth from 32.9–34.1. Both, temperature and oxygen decrease with depth, however, the stronger decline in oxygen at 215 mbsl is not observed in the temperature profile, as it was the case for CTD 281-1 and 284-4. Oxygen isotopes have the lowest values in the surface water, decline downwards and show the lightest $\delta^{18}O$ values of -1.7 to -2.0‰ close to the seafloor.

Methane concentrations are low and fluctuate between 2.9 and 5.2 nM, only one value reaches a concentration of 9.5 nM at 210 mbsf. Highest methanotrophic activity (*k'*) was found in the intermediate layer and lower values again in the bottom layer (0.0004 d^{-1}).

DISCUSSION

Methane source

Our stable carbon isotopic data indicate a biogenic origin of the methane sampled at the 4 study sites, with values of $\delta^{13}C\text{-}CH_4$ ranging from -65‰ to -100‰ [*Whiticar*, 1999]. These results support the conclusion of *Römer et al.* [2014a], based on a smaller methane isotope data set. The question remains as to the organic carbon source that may be sustaining methanogenesis in the area.

Seepage of biogenic methane at high latitudes has been attributed to a variety of processes including melting of glaciers and sea-ice, gas hydrate destabilization, climatically-driven enhanced biological productivity and other anthropogenic forcing [e.g. *Christensen*, 2004; *Jung and Vogt*, 2004; *Walter et al.*, 2006; *Archer et al.*, 2009; *Carlson*, 2013; *Damm et al.*, 2015].

The data collected in Cumberland Bay in the framework of this study clearly indicate that the methane source for the observed seepage lies within the sediments, since sediment and water column samples retrieved close to the marine terminating Nordenskjölk Glacier did not reveal elevated methane concentrations. There is therefore no evidence that water flow at the glacier base or thawing of permafrost are currently contributing to the methane budget in Cumberland Bay.

Another possible anthropogenic carbon source to the upper centimeters within this bay was proposed by Platt (1979), who suggested that there was a significant input of organic carbon to the bay in the form of remnants of hundreds of whales, which were discarded each year close to the shore during the period where the whaling station at Grytviken was active. But this would affect only the upper centimeters of the core. And even though high primary production can be observed north of South Georgia [*Atkinson et al.*, 2001], our sediment sites inside the bay indicate only relatively low sedimentary organic carbon contents of 0.65 wt.%.

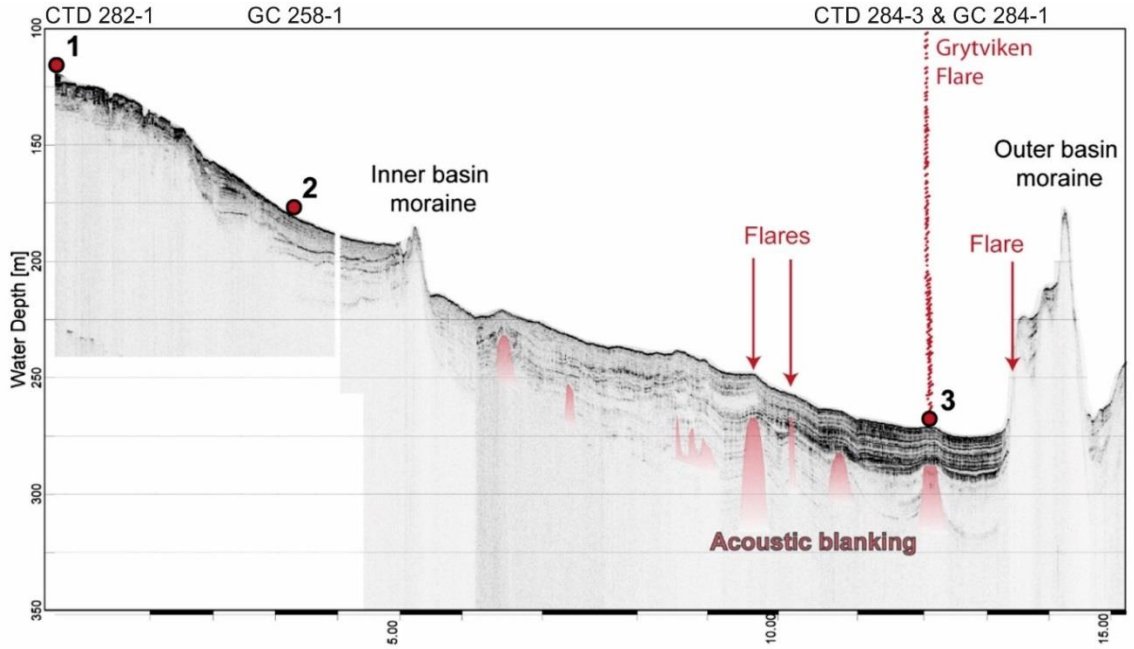

Figure 16: Parasound profile of Cumberland Bay East crossing station 1-3 (red circles indicated by station number). Within this bay an Inner basin moraine and parts of the outer basin moraine are observable [Hodgson et al., 2014]. Arrows show the location of strong (bubble streams) and weak (arrow) flare locations, the Grytviken Flare is projected from a profile line several meters next to this line, therefore acoustic blanking, indicated by red area in sediment does not reach the surface.

Kvenvolden and Claypool [1988] stated that 2 wt.% of organic carbon should be available in the sediments to support significant methanogenesis, which is higher than the values measured in the 8-meter cores retrieved from the Cumberland Bay. We postulate a scenario, where the observed methane seepage is fed by methanogenesis in organic-rich sediments which are below the cored depth. These organic-rich layers could originate from high OC accumulation during deglaciation. Peat formation or peat layers on South Georgia in the Cumberland Bay are reported by *Van Der Putten and Verbruggen* [2005], and can quickly develop onshore after deglaciation [*Smith*, 1981; *Björck et al.*, 1991]. These peats can be eroded and transported by glacio-fluvial processes and deposited offshore during deglaciation. This is a relatively fast process and allows the organic material to be buried without being completely decomposed. Therefore, these organic carbon-rich layers are likely to be buried beneath 10's of meters of sediment within the Cumberland Bay and along the South Georgia margin. Unfortunately, no core is available reaching the depth and age of this/these layer(s). Nevertheless, this assumption is consistent with the report of authigenic carbonates by *Meisel et al.* [2014] in a 8-meter core retrieved in the vicinity of station 6. These authors attribute the formation of these carbonates also to a widespread occurrence of biogenic methane on the shelf. The anaerobic oxidation of methane by sulfate

produces bicarbonate and induces the formation of authigenic minerals [*Bohrmann et al.*, 1998; *Nöthen and Kasten*, 2011; *Römer et al.*, 2014b]. Parasound data collected during the ANT-XXIX/4 expedition reveal distinct acoustic blanking features indicative of gas migration from depth [*Römer et al.*, 2014a]. The subbottom echosounder data corresponding to the profile that crosses our stations 1–3 is illustrated in Figure 16, and documents acoustic blanking most probably caused by elevated gas content in sediments that extends to 20–50 meters below the sediment surface. It is therefore likely that microbial degradation of post-glacial organic carbon deposits supplies enough methane to support gas migration from depth, which is reflected in the subbottom, sediment and water column methane data reported here.

Carbon transformations during transport to the seafloor

When methane accumulates in the sediment at concentrations that exceed its solubility, the overpressures generated by the development of a gas phase force upward migration of the methane-rich fluids towards the seafloor [*Paull et al.*, 1995; *Nunn and Meulbroek*, 2002]. If diffusing methane ions or upward migration of these fluids reaches pore fluids that contain sulfate, anaerobic oxidation of methane (AOM) by sulfate acts as a microbial filter suppressing the release of methane to the bottom water [*Alperin et al.*, 1988; *Hinrichs et al.*, 1999; *Boetius et al.*, 2000; *Valentine and Reeburgh*, 2000]. This reaction, which is typically mediated by a metabolic consortium of methane-oxidizing archaea and sulfate-reducing bacteria [*Hoehler et al.*, 1994; *Hinrichs et al.*, 1999; *Boetius et al.*, 2000] can be summarized as:

$$SO_4^{2-} + CH_4 = HCO_3^- + HS^- + H_2O \qquad \text{(Eq. 4)}$$

This reaction consumes sulfate and methane, leading to the development of the SMI, where these two dissolved compounds get depleted [*Niewöhner et al.*, 1998; *Borowski et al.*, 1999; *Paull et al.*, 2000]. Additional to that, SO_4^{2-} is also consumed by organoclastic sulfate reduction (SR) during organic matter degradation [*Berner*, 1980]. We recognize the complexity of reactions that cycle carbon near the SMI, which have been documented and quantified by a variety of approaches [*Snyder et al.*, 2007; *Torres and Kastner*, 2009; *Hong et al.*, 2013, 2014; *Pohlman et al.*, 2013; *Yoshinaga et al.*, 2014]. In the simplest approach, we compare the fluxes of sulfate and methane into the SMI, where downward diffusing sulfate and upward migrating CH_4 are consumed at an equimolar basis during AOM (Eq. 4). If methane and sulfate reflect in situ values (i.e. no methane is lost during core retrieval or if the gradient into the SMI is determined close to the SMI where methane concentrations are

significantly below saturation), their fluxes to the SMI should balance [*Reeburgh*, 1976; *Borowski et al.*, 1997; *Niewöhner et al.*, 1998; *Malinverno and Pohlman*, 2011].

Dissolved inorganic carbon (DIC) is a product of both AOM and the degradation of organic matter; however, here we do not include DIC in our analyses since alkalinity was not measured and we have only a rough estimate of the DIC removal by authigenic carbonate formation [*Sivan et al.*, 2007]. Authigenic carbonate formation does not affect methane concentrations or the isotopic composition of the methane-carbon [*Teichert et al.*, 2005], so we limit our analyses at comparing methane and sulfate fluxes.
The quasi-linear concentration profiles obtained at most sites (except for station 4) indicates that diffusion is presently the dominant transport mechanism of methane towards the SMI. Data from station 6 show linear profile shapes and equal consumption of CH_4 and SO_4^{2-} at the SMI, where both are consumed in an almost 1:1 ratio (0.97: 1), and thus indicate that AOM is the main reduction process of SO_4^{2-} [*Malinverno and Pohlman*, 2011]. In contrast, inside the bay at station 3 (GC 284-1), the sulfate flux (-0.135 mmol/m^{2}a) towards the SMI is over two times larger than the corresponding methane flux (-0.061 mmol/m^{2}a); which could point to an additional removal of SO_4^{2-} by organoclastic SR.

A comparison of diffusive SO_4^{2-} and CH_4 fluxes towards the SMI was not possible at stations 2 and 4. Core GC 258-1 (station 2) reveals only very low methane concentrations and no SMI could be determined and GC 281-2 at the Cumberland Bay Flare (station 4) has such a strong flux of methane into the SMI that the resolution of the data points with a distance of one meter was too low to construct a realistic methane concentration gradient. Furthermore at station 4, the downcore profiles indicate an advective component to the flux, making any inferences based solely on diffusive flux estimates unreliable.

Video images taken on ANT-XXIX/4 show that the bacterial mats at the seepage sites are only centimeters to decimeters in size [*Römer et al.*, 2014a], this could indicate that these sites are relatively young and that seepage was not very strong in the past, furthermore, it makes it difficult to get a core directly from the seepage location when no visual guidance for coring placement is available. However, the data obtained from our cores reveal a significant removal of methane by AOM, even at the stations close to the seepage sites.

Methane concentrations at station 4 could also indicate methanogenesis with a methane peak in 150–350 cmbsf, however, the relatively low carbon content in these sediments and the vicinity to a bubble emission site makes it more likely that methane is originating from below. A possible explanation for the lower methane concentrations in the deeper part of the core could be supersaturation. These samples may reflect a faster loss of methane

during sampling; assuming very high concentrations (>40 mM methane), which would accelerate degassing since solubility of methane is only around 2 mM under atmospheric pressure [*Yamamoto et al.*, 1976] and thus, would result in lower concentrated methane samples than they actually are. Furthermore, the location of the SMI is shallowest at station 4 (Figure 14), which indicates a methane flux from below that is stronger than at the other locations [*Borowski et al.*, 1999]. A faster transport of methane towards the seafloor, supported by fluid advection, will also prevent significant isotopic fractionation of methane carbon [*Zhang and Krooss*, 2001; *de Visscher et al.*, 2004]. The heaviest methane-carbon signatures ($\delta^{13}C\text{-}CH_4$ = -65‰) are observed in core 281-2 (station 4) at the Cumberland Bay Flare and are quite constant from the SMI depth to the bottom of the core. The value of -65‰ most likely represent the stable carbon isotopic signature of the source material, whereas most of the other cores show $\delta^{13}C$ values that reflect a degree of isotopic fractionation. Two methane samples collected in the water column close to both seepage sites (CTD 284-3, 252mbsf; CTD 281-1, 249 mbsf) were also analyzed for their $\delta^{13}C$ value. The sample close to the Grytviken Flare (CTD 284-3) has a value of -55.8‰ and the one close to the Cumberland Bay Flare (CTD 281-1) reveals a $\delta^{13}C\text{-}CH_4$ of -55.2‰. Assuming that the upward advecting methane gas has an isotopic signature of -65‰, the methane carbon in the water column has to be fractionated by methane oxidation or mixed with background water to reach $\delta^{13}C$ values around -55‰.

As microbial activity preferentially targets the lighter carbon isotope ^{12}C, the DIC (HCO_3^-) produced by organic matter degradation and by AOM should have more negative $\delta^{13}C$ values than the source substrate. Indeed, the most negative values of $\delta^{13}C$-DIC in each core were found around the SMI, where DIC is produced from anaerobic oxidation of a ^{12}C-enriched methane source (Figure 14). This same fractionation induced by AOM yields methane enriched in ^{13}C [*Hinrichs et al.*, 1999]. However, several recent studies have shown a decrease in $\delta^{13}C\text{-}CH_4$ values in the zone where methane concentrations are reduced [*Pohlman et al.*, 2008; *Hong et al.*, 2013; *Treude et al.*, 2014; *Yoshinaga et al.*, 2014]. Our data from GC 284-1 (station 3) also show a marked decrease in $\delta^{13}C\text{-}CH_4$ towards the SMI, where it reaches values as low as -96.4‰. Although less pronounced, the isotopic data of methane in core 280-1 also show decreasing values towards the SMI. Two different processes have been postulated to explain the observed $\delta^{13}C$ depletion of methane at the SMI, which we consider here in the context of our Cumberland Bay observations.

(1) Secondary methanogenesis within the SMI, supported by recycling of ^{13}C-depleted DIC produced by AOM [*Borowski et al.*, 1997; *Paull et al.*, 2000; *Hong et al.*, 2013, 2014]. No

organic matter is involved in this process, rather methanogenesis from DIC proceeds according to the reaction:

$$4H_2 + HCO_3^- + H^+ = CH_4 + 3H_2O \quad \text{(Eq. 5)}$$

This secondary methanogenesis produces methane with a $\delta^{13}C$ value that is depleted in ^{13}C by 55–65‰ relative to the DIC source [*Claypool and Threlkeld*, 1983; *Whiticar*, 1999] but does not significantly increase methane concentrations. The observed minimum in $\delta^{13}C$ - CH_4 values measured at the SMI in this study (-96.4‰) requires a DIC source for methanogenesis that is at least partially derived from AOM, thus indicating that methanogenesis and AOM are coupled and active within and below the SMI.

(2) AOM back flux, where $\delta^{13}C$ depletion of methane is attributed to AOM-mediated carbon isotope equilibration caused by SO_4^{2-} limitation below the SMI [*Yoshinaga et al.*, 2014]. Under sulfate limitation AOM leaves distinctly ^{13}C-depleted residual methane which is visible in the upper three meters of core 281-1. Because here we observe strong fractionation towards ^{13}C-depleted methane, the AOM back flux has to be larger than the regular forward reaction, otherwise the fractionation effect within the SMI would not be as prominent as we observe here.

It is also important to note that the methane stable carbon isotopic composition above the SMI in core 284-1 shows a strong change from -96 to -73‰ in just 100 cm, and that the heavier values remain relatively constant above the SMI. Methane concentrations of these sediments is very low (≤ 17 µM), but the reproducibility of duplicate analyses of one sample just above the SMI give credence to these values. A possible mechanism that may explain this observation would be that the isotopic fractionation process by AOM above the SMI enriches the $\delta^{13}C$ values from -96‰ to -74‰. The isotopic values imply that in this region no significant secondary methanogenesis occurs and there is no sulfate limitation to support fractionation by AOM back flux. Our data indicate that whatever process is responsible for the observed isotopic distribution, it must be limited to a distinct depth because the change in isotope values is sharp and no diffusion can be observed between the different methane pools below/within the SMI and above the SMI (see Figure 14, station 3).

With the amount of data available it is hard to establish which process is responsible for the observed $\delta^{13}C$ values for methane. It is very likely that all the reactions are intimately coupled and the data reflect the collective result of carbon cycling pathways in the vicinity of the SMI.

Fate of methane in the water column

Local Hydrography. A temperature-salinity (TS) plot using data from Cumberland Bay East has been used to identify the water masses in this area (Figure 17). This approach shows the presence of a local melt-water lens, produced by melting of glacier ice and floating icebergs from the Nordenskjölk Glacier.

This melt-water lens extends from the sea surface to ~ 25 m, and it is characterized with 6_T values lower than 26.75 and salinities below 33.6. The thickness of this layer decreases with increasing distance from the glacier and it is not apparent in station 5, outside the bay.

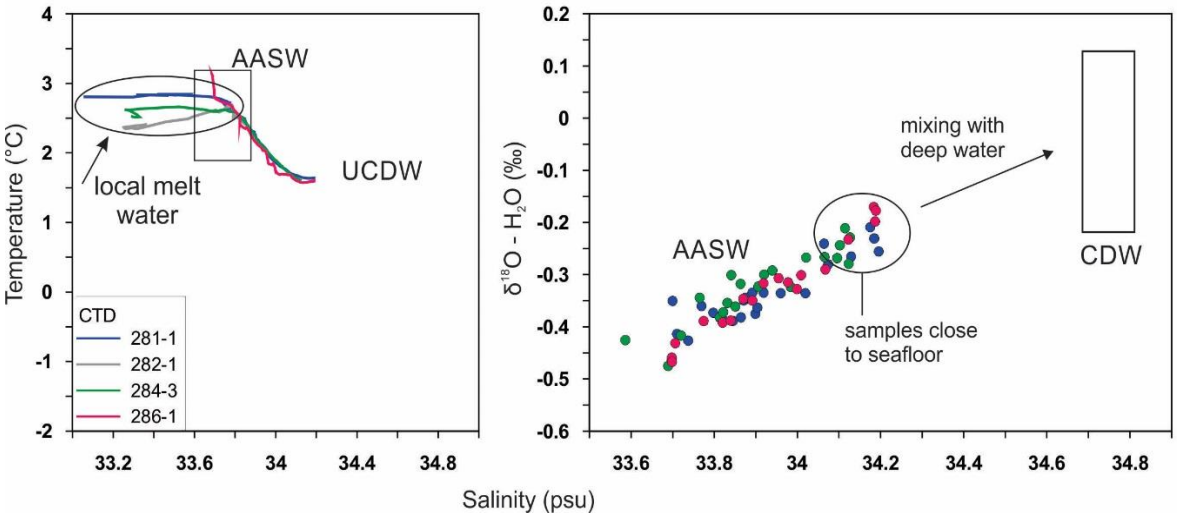

Figure 17: Temperature-Salinity plot (left) illustrates the presence of a fresh melt water layer in the upper 25 m of the water column; Antarctic surface water (AASW) is found immediately beneath the fresh water lens, and the bottom of the bay is filled with a mixture of AASW and Upper Circumpolar Deep Water (UCDW) [Meredith, 2003b]. Consistently, $\delta^{18}O$ data plotted against salinity (right) also indicate a mixture of AASW with Circumpolar Deep water (CDW) [Archambeau and Pierre, 1998].

The water mass below the melt-water lens plots in the temperature and salinity field characteristic of the AASW (Figure 17). AASW is characterized by typical summer temperature values of 2–3 °C and salinities of 33.6–33.8 over the South Georgia shelf, and in the Cumberland Bay was clearly identified in samples collected from 30 to 150 meters water depth. Oxygen concentrations in AASW of the Cumberland Bay range between 7.18 – 6.57 mg/l. These values correspond with data reported by Meredith et al. [2003] along a transect from the northern shelf of South Georgia into the Georgia Basin that was sampled during austral summer in 2000. The deepest waters of the bay and the adjacent shelf plot towards the UCDW in the TS curves. However, the maximum salinity value of 34.2, sampled

close to the seafloor is still too low to belong to this deep water mass, which is characterized by a salinity of 34.70 [*Meredith*, 2003b]. *Orsi et al.* [1995] described an isopycnal horizon at 6_T = 27.6, characteristic for the UCDW. The maximum density of station 6 reaches only a value of 27.4.

Collectively, our data indicates that the water sampled in this study beneath the Antarctic Surface water is most probably a mixture between the AASW and the underlying UCDW. Water masses illustrated in Figure 17 using the isotopic composition of the water samples confirm this classification. Even though the amount of water isotope data limits this comparison, data from Southern Ocean waters between South Africa and Antarctica [*Archambeau and Pierre*, 1998] support our inference that the water column immediately below the fresh water melt represents AASW with an isotopic signature of -0.25 to -0.5‰. Data taken in the lower water column tends towards higher salinities and lower $\delta^{18}O$ values, as reported for the CDW [*Archambeau and Pierre*, 1998].

Sink of methane. Within the context of this hydrographic regime, we note the input of methane to the bottom water documented by the presence of hydroacoustic flares and elevated methane concentrations in the bottom water (Figures 15, 16). The two major identified flares (Grytviken Flare and Cumberland Bay Flare) reach a height of ~100 m below the sea surface, additional minor flares were also imaged in Cumberland Bay but with a much lower intensity. Rising bubbles at the two major seep sites emanate as single bubbles from the seafloor and no continuous stream was visually observed during the cruise [*Römer et al.*, 2014a].
It is well documented that methane diffuses out of bubbles [*Guinasso and Schink*, 1973; *McGinnis et al.*, 2006; *Greinert and McGinnis*, 2009], so that most of the methane released as gas dissolves soon in the surrounding water column. Indeed, we observed elevated methane concentrations in the bottom water close to the bubble streams.

Once dissolved, methane in the water column can be consumed by aerobic microbial oxidation or it can be transported and diluted. The measured methane oxidation rates (MOx-rates) compared to the list of data presented in Mau et al., 2013, that include seepage sites offshore Svalbard and in the Santa Barbara Basin, indicate very low rates of methane oxidation (Table 4). As the oxidation rate is the product of the rate constant (relative methanotrophic activity) and the methane concentration, either lower activity or lower methane concentrations might explain the low MOx-rates.

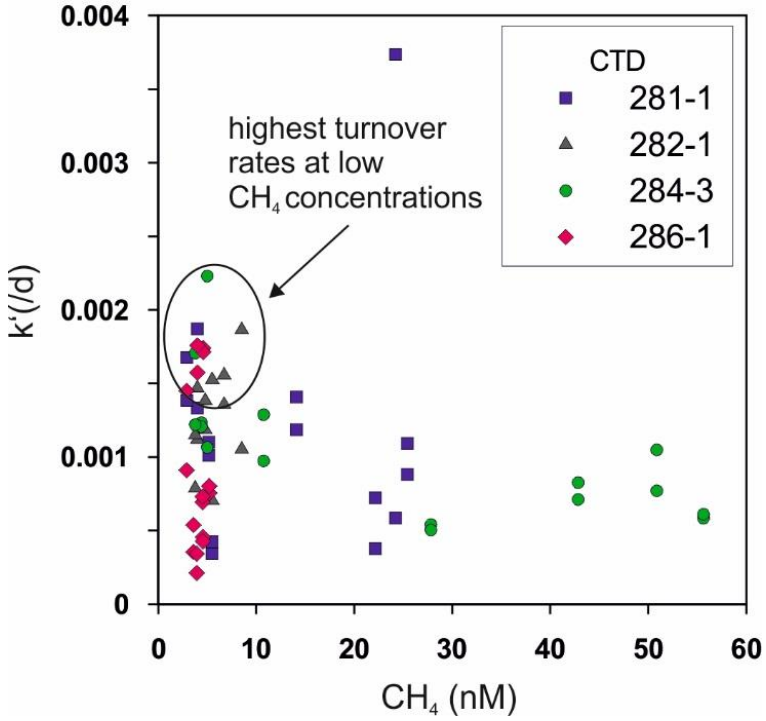

Figure 18: Relative methanotrophic activity (k') per day plotted over CH_4 concentrations in water samples collected at all CTD stations. Highest activities were observed where methane concentrations are low.

Table 4: Microbial turnover rates of methane and Sea-air flux in the Cumberland Bay compared to other seepage sites.

Area	**M**in	**M**ax	**A**verage	**R**eference
	Microbial turnover rates of methane			
Storfjorden/Spitsbergen	2.15 yr	0.06 yr	0.28 yr	[*Mau et al.*, 2013]
Santa Monica Basin	3.5 yr	0.04 yr	0.34 yr	[*Heintz et al.*, 2012]
Santa Barbara Basin	1.80 yr	0.02 yr	0.35 yr	[*Mau et al.*, 2012]
Cumberland Bay	6.44 yr	0.85 yr	3.12 yr	
	Sea-air flux in nmol/m^2s			
Baltic Sea	0.008	1.145		[*Gülzow et al.*, 2013]
Santa Barbara Basin	0.02	18.35	0.47	[*Mau et al.*, 2007]
Cumberland Bay	2.12E-05	0.02	0.005	

Comparing the dissolved methane concentrations measured off Svalbard and in the Santa Barbara Basin in the down-current plume of the Coal Oil Point seepage field, we found that

methane concentrations were lower in the Cumberland Bay (Table 4). However, the differences between these sites are on the orders of magnitudes in the case of turnover time, which is the reciprocal of the relative activity (*k'*). Hence, both, low methane concentrations and the low potential of methanotrophic activity, results in the low MOx-rates in the Cumberland Bay (Table 4). Ongoing research tries to identify the restriction.

Highest MOx-rates were observed where methane concentrations are highest close to the seafloor, although the relative methanotrophic activity is low. Higher relative activities appear where methane concentrations are reduced (Figure 18), right above the methane plume (see also Figure 15). Thus, the dissolved methane that is transported vertically by turbulent eddy diffusion of the water appears to be faster oxidized than in the bottom water. Possibly the AASW has a higher potential for methane oxidation than the mixture of AASW and UCDW. The UCDW with its low oxygen concentrations indicates that most organic matter in the water mass is consumed and thus microbial activities and abundances (including methanotrophs) might be limited.

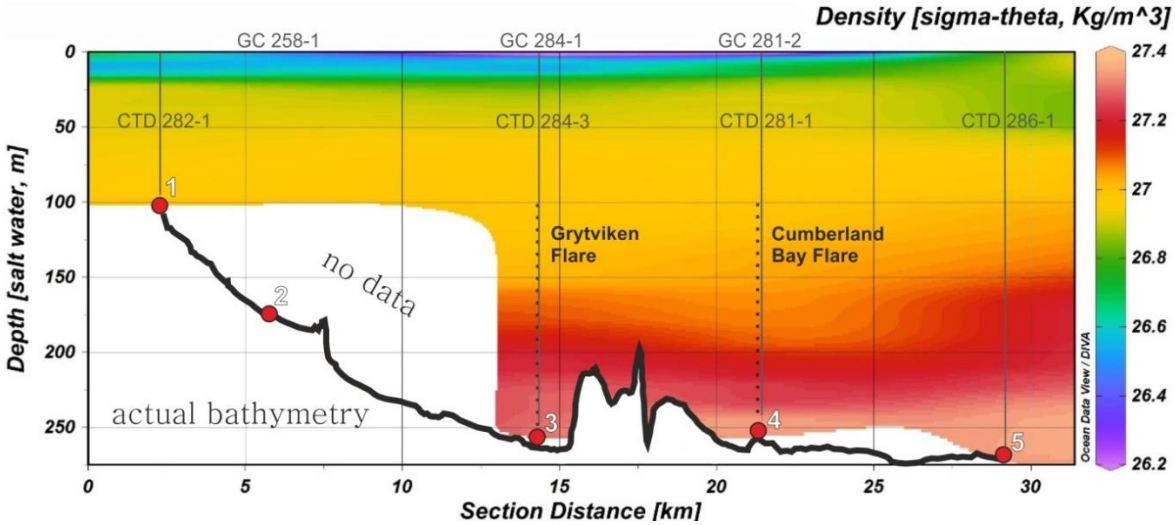

Figure 19: Sigma theta plotted over depth along transect from station 1 to station 5 (red circles), illustrating the extent of the fresh water lens, and deep waters in the Bay. As well as location of the CTDs. DIVA grid was processed with CTD data and station depth. Depth profile obtained from parasound bathymetry was overlaid on the Ocean Data View (ODV) plot (bold black line).

To constrain the vertical transport and possible release to the atmosphere we compare the methane concentration in the upper meters of the water column with the atmospheric

equilibrium value at our site. For a temperature of 2.7 °C and a salinity of 33.6 the atmospheric equilibrium of methane is around 3.3 nM [*Wiesenburg and Guinasso*, 1979]. Methane concentrations in surface waters range from 3–5 nM and are therefore only slightly enriched compared to the atmosphere. Sea-air flux was calculated using parameterization developed by *Wanninkhof et al.* [2009]. This exercise resulted in a mean value of 0.005 nM/m²s, with a maximum of 0.02 nM/m²s. Required methane data from surface waters were rather taken in the surface melt water layer than in the surface mixed layer.

A comparison with two other seepage sites in Table 4 shows that even the highest flux is very low compared to a maximum sea-air flux of other regions where methane seepage occurs at shallow depths [*Mau et al.*, 2007; *Gülzow et al.*, 2011]. These results are not surprising since the water column within the bay is stratified. The local meltwater lens, with a $6_T \leq 26.8$, clearly separates the underlying waters, where 6_T ranges from 26.9 to 27.1. This strong pycnocline prevents any methane dissolved in the deeper layers from escaping to the atmosphere (Figure 19).

Since methane appears slowly consumed by microbes and if at all only a small fraction reaches the upper part of the water column, it seems to be dispersed horizontally and vertically in the water column. The larger fraction appears to prevail in the lowermost water mass to be transported and diluted by methane-free UCDW. At station 5, a small peak in 210 mbsl was observed (9.5 nM). This indicates that either methane is diluted very fast that no elevated values can be detected outside the bay or that we just sampled in the inflow waters and missed the water masses leaving the bay.

CONCLUSIONS

We suggest that the methane gas accumulations in Cumberland Bay sediments probably originate from peat-bearing sediments similar to those found on land, which correspond to high OC accumulation rates after the last glaciation. Advective gas transport in form of bubbles within sediments is limited to very small areas, as imaged by distinct blanking zones in the sub-bottom data, discrete flares and very small patches of bacterial mats on the seafloor. Most of the methane appears to be transported in the sediment via diffusion. Because this transport mechanism is slow and involves dissolved methane, a large fraction of the methane is consumed by AOM. Anaerobic consumption and production of methane in the SMI region leads to extreme isotopic fractionation, with $\delta^{13}C\text{-}CH_4$ values being further depleted from -65‰ at the possible source gas to -96‰ measured just below the SMI at station 3 (Figure 20).

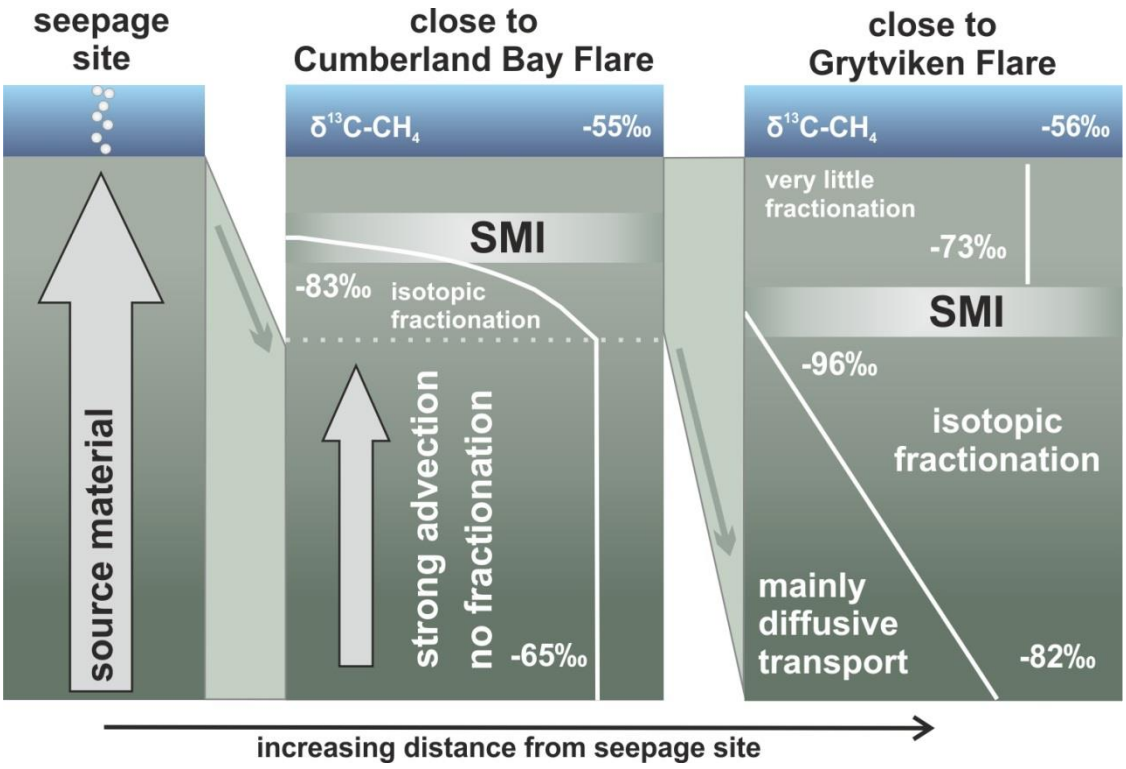

Figure 20: Schematic view of the transport mechanisms and isotopic fractionation of $\delta^{13}C$ in methane below and above the SMI. The actual seepage site was not sampled, but we infer that at this location methane escapes the microbial filter and is discharged in the gas phase at the seafloor. At station 4 (near the Cumberland Bay Flare), there is evidence for advecting supply of methane, which is consumed and fractionated towards lighter methane carbon at the SMI. The value of -65‰ is assumed to be that of the source gas. A strongest fractionation is observed at station 3 (Grytviken Flare), where methane carbon has values as low as -96‰.

Further aerobic methane degradations in the overlying water column might result in $\delta^{13}C$-CH_4 values around -55‰. Sulfate and methane flux estimates indicate that within the bay a large fraction of methane is consumed by AOM. This inference also supports our postulate that the methane is generated in deeper horizons with higher organic carbon contents. The discharge of methane gas rapidly dissolves in the bottom water leading to methane concentrations of up to 57.7 nM. This methane is probably trapped in the lowermost water mass beneath surface water and a melt-water lens. Notwithstanding the strong stratification, and resulting lack of methane exchange with the atmosphere, measured microbial turnover rates are extremely slow, suggesting that the main mechanism for methane dispersal is by horizontal advection and dilution. Unfortunately, there is not enough coverage of methane profiles to quantify the loss term by horizontal transport out of the Cumberland Bay.

ACKNOWLEDGMENTS

We would like to thank the shipboard support from the master and crew of the research vessel Polarstern during cruise ANT- XXIX/4. We are grateful to Ellen Damm and Anne-Christin Melcher for the analysis of $\delta^{13}C$-CH_4 samples in the water column at the AWI. We are also grateful to Benjamin Löffler, David Fischer and Eva Kirschenmann for their help with pore-water and sediment sampling on board. We further thank Gunter Wegener for helpful comments regarding the data. This work was supported by the Deutsche Forschungsgemeinschaft (DFG) in the framework of the priority program 'Antarctic Research with comparative investigations in Arctic ice areas' by a grant to BO 1049/19 and through the DFG-Research Center/Cluster of Excellence "The Ocean in the Earth System" MARUM. Patrizia Geprägs was further supported by a DAAD Grant (57044996) "Kurzstipendium für Doktoranden". Hydrographic data reported are made publicly available through the PANGAEA information system sustained by the World Data Center for Marine Environmental Sciences (WDC- MARE).

CHAPTER 4: CASE STUDY 2: SEEPAGE IN THE MEDITERRANEAN

METHANE IN THE WATER COLUMN ABOVE AN ACTIVE MUD VOLCANO IN THE CALABRIAN MARGIN

Patrizia Geprägs[1], Marta E. Torres[2], Miriam Römer[1], Thomas Pape[1], Paul Wintersteller[1], Gerhard Bohrmann[1]

In preparation for Journal of Geophysical Research

[1]MARUM – Center for Marine Environmental Sciences and Department of Geosciences,
University of Bremen, Klagenfurter Str., 28359 Bremen, Germany
[2]College of Earth, Ocean, and Atmospheric Sciences, Oregon State University, 104 CEOAS, Administration Building, Corvallis, OR 97331-5503, USA

ABSTRACT

Methane release from submarine mud volcanoes is well known, but most of the input estimates so far are based on sediment fluxes or visual observations in the water column. Here we combine hydroacoustic mapping, bottom water sampling and collection of gases at the seafloor in two contrasting settings (mud flows and gas seeps) of the Venere MV, an active mud volcano in the Calabrian Margin, Ionian Sea. Active gas discharge at five flare locations show strong variability in intensity over repeated surveys over 31 days. Four of these flare sites are arranged along a circular structure around the mud volcano, with one weak bubble emission site located in the vicinity of the summit. Bottom water over gas flares and mud flow sites has very high methane concentrations up to 566 μM only in close proximity to the seafloor, and no significant methane (< 20 nM) is detected ~100 meters above seafloor. The highly concentrated methane plumes are relatively small and stationary with a vertical extend of 5 m above the seafloor and a maximum horizontal distribution of 50 m. The advective input, estimated by direct gas collection at the most active flare site, is 0.39 mol/min. The diffusive input from degassing mud is 11 mol/min, much higher than the vertical gaseous methane input from the combined bubble emission sites. Despite the strong methane flux, high concentrations are only observed close to the seafloor, no methane reaches surface waters. Methane oxidation in the water seems to be a major methane sink.

INTRODUCTION

Submarine mud volcanoes are known to occur worldwide with a variety of morphological expressions [*Milkov*, 2000; *Dimitrov*, 2002; *Kopf*, 2002]. All of them, independent of their shape, transport fluidized sediments, gases and water from deep within the sediment to the seafloor [e.g. *Kopf*, 2002; *Deville et al.*, 2006], driven by excess pore pressures at depth. Methane, and other hydrocarbons are the most prominent gases responsible for the mud eruptions [*Kopf*, 2002]. It is therefore common to observe fluid vents in the vicinity of mud volcanos. These gas vents may be distributed randomly, or cluster either in the center of the mud volcano (e.g. Hakon Mosby [*Sauter et al.*, 2006]) or along linear or circular fracture systems around the mud volcano [*Deville et al.*, 2010].

Methane discharge from mud volcano systems is not only associated with active fluid seepage at vents, but the extruded muds are also very enriched in methane and degas slowly into the bottom water by compaction and diffusion [*Wallmann et al.*, 2006] contributing to the methane budget [*Kopf and Behrmann*, 2000]. Current estimates of methane released to the bottom water from mud volcanoes are based on sediment fluxes and pore fluid modeling from small sampled areas, which are then extrapolated to the overlying water column [e.g. *Haese et al.*, 2003; *Kopf*, 2003; *Milkov*, 2003; *Sauter et al.*, 2006; *Wallmann et al.*, 2006]. Several factors compromise these estimates. Within the sediments the methane supplied in the dissolved phase is efficiently consumed by anaerobic oxidation of methane (AOM) [*Hinrichs et al.*, 1999; *Boetius et al.*, 2000]. And visual observations at seeps only capture the advective bubble flux. The overall methane impact in the overlying water column is then affected by gas composition, water depth and gas exchange out of the bubble during its rise. Therefore, the best way to constrain the total methane input, both diffusive and advective, is by direct sampling of the water column above active mud volcanoes.

In this study we report on bottom water and water column measurements performed above an active mud volcano (Venere MV) in the Calabrian accretionary prism, offshore Italy (Figure 21). Our data allow us to compare the advective input, estimated from a bubble emission site, with the diffusive input from a recent mud flow.

STUDY AREA

Mud volcanoes are very abundant along the eastern Mediterranean Ridge [*Mascle et al.*, 2014] but only few (54 MVs) have been reported on the Calabrian accretionary prism

[*Ceramicola et al.*, 2014]. This accretionary prism is ca. 300 km wide and extends from onshore Calabria to a frontal trust in 4000 mbsl [*Ceramicola et al.*, 2014]. Among these volcanoes, Venere is the only one with present day mud flow extrusion and advective methane discharge. It was first described by *Ceramicola et al.* [2014] as having twin cones reaching 60 m above the seafloor and a high backscatter area.

Detailed surveys of the Venere MV during RV METEOR expedition M112 (October and November 2014) document that both summits reach a water depth around 1500 m, but only the western summit is currently experiencing mud flow discharge (Figure 21). Our water column surveys are focused on and around the western summit, and no sampling was conducted along the eastern summit since here no recent mud flow nor gas discharge were observed.

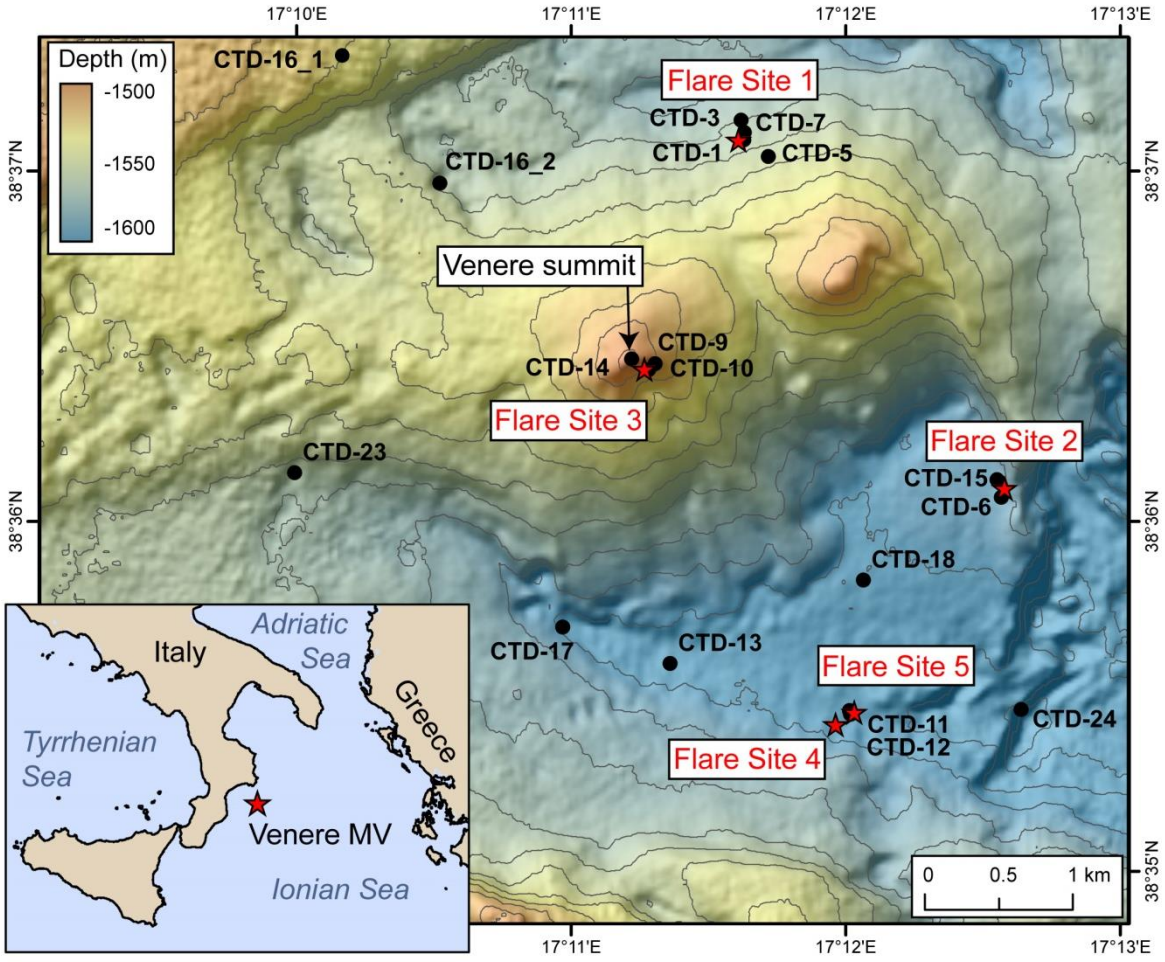

Figure 21: Study area in the Ionian Sea with the Venere MV in the center, the summit mark the active summit with the mud extrusion site on top. Flare sites are indicated by a red star and appear on a concentric rim around Venere MV and in the center.

MATERIAL AND METHODS

One of the main targets of the RV Meteor cruise M112 was to explore gas emission sites in the area around Venere MV with a focus on their temporal and spatial variability. Gas emission sites were mapped acoustically, and the gas plumes in the water column are designated here as flares. To this aim we used a hull-mounted multibeam echosounder (KONGSBERG EM122); and a multibeam sonar (KONGSBERG EM2040) mounted on the autonomous underwater vehicle AUV SEAL operated by MARUM.

We conducted repeated surveys along a path that crossed all flare locations in the Venere area to monitor activity and intensity of gas emissions over 31 days. These data, as well as those obtained by repeated hydrocasts in the area were interpreted in the context of sub-seafloor features imaged by a hull-mounted parametric sub-bottom profiler (ATLAS PARASOUND). Post-processing of the data was done by FLEDERMAUS MIDWATER (©QPS) and by ESRI ARCGIS™.

The seafloor in the Venere MV area was also explored using the MARUM remotely operated vehicle ROV QUEST 4000. Real-time video streaming from the vehicle provided us with detailed images of the seafloor and guided our sampling of both gas streams and bottom water in close proximity to the seeps using a Gas Bubble Sampler (GBS) operated by the ROV (Figure 22a and 22b). These custom built samplers consist of 400–500 ml evacuated steel tubes outfitted with a valve that is closed under atmospheric pressure before deployment and opened on the seafloor. Bubbles and fluids are collected through a funnel located in front of the valve and forced into the sampling tube by the underpressure of the empty barrel [*Pape et al.*, 2010b]. Although the GBS were initially designed to sample gases, we also utilized this sampler to collect water samples with the ROV in close proximity to the seafloor. In total, we collected 20 bottom water samples and four gas samples from locations of active bubble discharge.

The effect of seafloor seepage on the water column was investigated by conventional hydrocast sampling in 22 sites in the Venere MV area. Physical-chemical parameters (temperature, salinity and oxygen) were monitored during each down and up cast with a Seabird SBE 9plus CTD probe. Water samples were taken from 17 of these stations during CTD upcasts, using 21 (12L) Niskin bottles mounted on a rosette. Since our study was focused on the effects of seepage in the water column, some casts were designed to sample only the deeper water by repeated lowerings of the rosette at nearby locations (marked with the numbers 1-3 behind the CTD number). This tow-yo approach allowed us to enlarge the sampling resolution near the seepage sites.

Good positioning of the CTD was achieved with an ultrashort baseline navigation system POSIDONIA IXSEA mounted on the CTD cable approximately 10 m above the rosette. Such precise navigation was particularly useful in the vicinity of seepage sites, where several lowerings of the water sampling rosette were conducted aided by the exact positioning provided by POSIDONIA, thus, each water sample has its own coordinates.

An upward- and downward-looking Lower Acoustic Doppler Current Profiler (LADCP) from the Institute for Physical Oceanography, University of Bremen was mounted in the sampler rosette, which took the space of three Niskin bottles. The LADCP was deployed to generate water current speed and direction data in 20 of the hydrocasts. A MATLAB post-processing toolbox was used to process the LADCP raw data, aided by CTD time information (start time and end time of individual casts and bottom contact) as well as accurate GPS positions for the start and end point. Detailed description of the post processing can be found in *Fischer and Visbeck* [1993] and *Visbeck* [1995].

Analyses

Methane concentrations in water samples collected from both the Niskin bottles as well as the GBS samplers were determined by the headspace extraction and analyses described in Geprägs et al. 2016 (in submission, see chapter 2). Briefly, two 140 ml-syringes outfitted with a 3-way valve were flushed and filled with 100 ml of water, care was taken that no air bubbles were left in the syringe before closing the valve. After syringes were equilibrated to room temperature, 40 ml of Zero Air (synthetic air without methane) were added to each syringe which were then shaken for minimum 1.5 minutes.

For the water column samples, the 80ml of headspace gas (40 ml from each syringe) were injected in the Greenhouse Gas Analyzer from Los Gatos Research (GGA-30r-EP) and diluted with 60 ml of Zero Air within the chamber of the instrument. Since methane concentrations in the GBS samples were elevated, we used a higher dilution with Zero Air before analyses with the GGA. The remaining headspace gas was stored in 20 ml-glass vials containing a saturated NaCl-solution for isotopic analysis (method see below).

Gas samples collected directly over the bubble discharge with the GBS were analyzed onboard for their composition and concentration using a two-channel 6890N (Agilent Technologies) gas chromatograph [*Pape et al.*, 2010a].

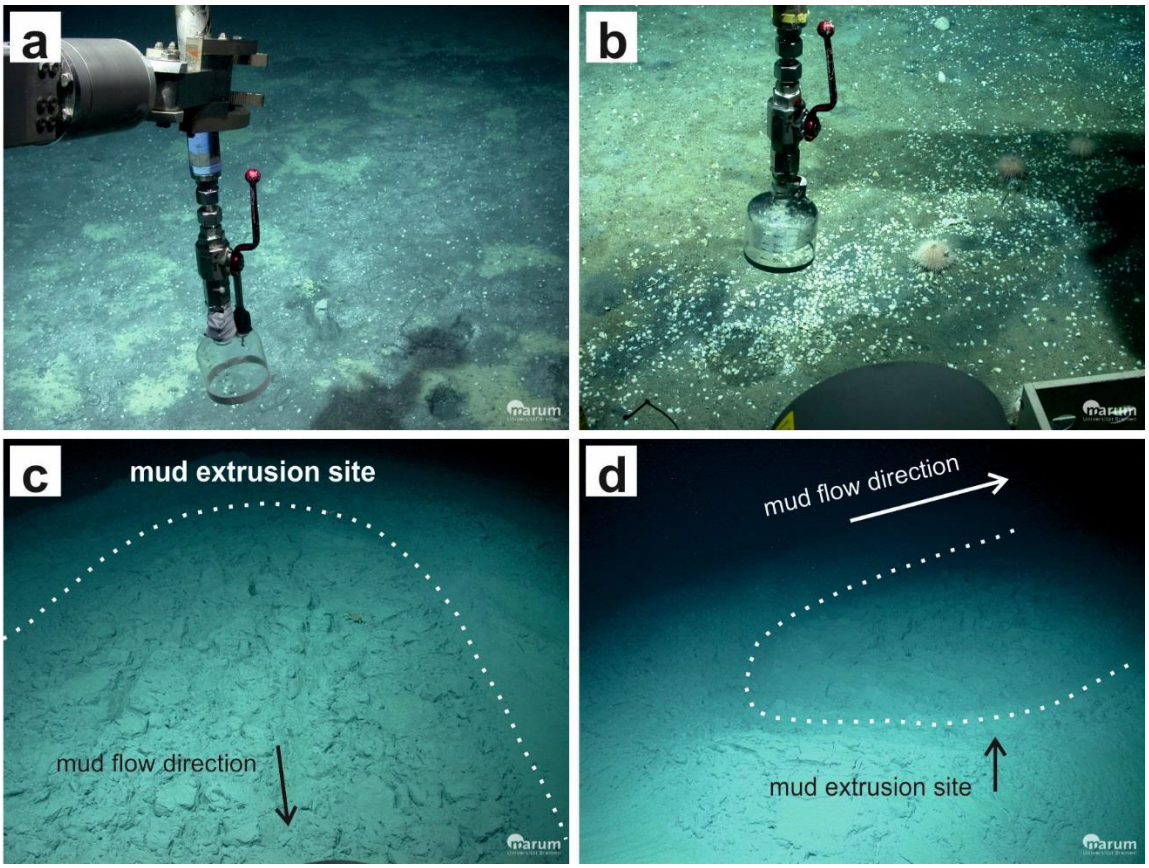

Figure 22: Sampling with the GBS for water and gas samples. a) Water sample GBS-3 is taken at Flare Site 1 above black spots with bacterial mats and small clams. b) Gas sample is collected at one emission site of Flare Site 4 for quantification and analysis of the isotopic and molecular composition of the gas. A lot of small clams and sea urchins are settled around the emission site with black spots on the sediment surface. c) And d) show the mud extrusion site at the summit of Venere MV from two directions the diameter of the mud extrusion is around 3-4 m. A thin yellow-brownish layer can be observed on the mud in picture c).

Light hydrocarbons (C_1 to C_6) were separated and quantified with a capillary column connected to a Flame Ionization Detector. The instrument was calibrated using commercial standard gases (100 ppm–100% methane in nitrogen). Precision of the analyses is better than 3%. Gas subsamples were also preserved in a saturated NaCl-solution for shore based analyses of their isotopic composition.

The gas extracted from bottom water samples with high methane concentration and gas samples collected directly over the vents and preserved in saturated NaCl-solution were analyzed for the stable carbon isotope ratio ($^{13}C/^{12}C$) of CH_4 using a GC-isotope ratio mass spectrometer (GC-IRMS) at the MARUM laboratories in Bremen agree within 0.2%.

RESULTS

Flare imaging and ROV observations

In total, five different flare locations were detected hydroacoustically. Four of the flare sites are arranged in a circular pattern around the rim of the mud volcano, and Flare Site 3 is situated inside the circular structure, on the southeastern flank of Venere summit (Figure 21). Flare Site 1 is located NE of the summit. This site showed intense bubbling activity early in the cruise, with a maximum flare height of 150 m above the seafloor. Repeated surveys in the second half of the cruise (11/26/14–12/10/14) showed weak to undetectable activity. Flare Site 2, east of the Venere summit, was active over the entire 26 day survey. Intensities were very variable, ranging from weak up to strong. The maximum height was 270 m above seafloor and was therefore the highest flare detected in that area. Emissions from Flare Site 3 had the weakest intensities; with strongest intensities during the first two days of the survey, and diminishing activity towards the end of the survey. The maximum flare height reached only 70 m above the seafloor. Flare Site 4 and Site 5 are situated in the southeast rim of the crater in close proximity to each other; both were active throughout the survey with high seepage intensities.

All flares reach a water depth between 1440–1325 meters. A relation to a distinct pycnocline was not observed, and since there was a strong variability in the intensity between the flare sites, the flare height is probably mainly dependent on seepage intensity.

ROV surveys of the flare sites revealed patches of biological activity with the characteristic presence of bacterial mats, clams, tube worms and sea urchins, accompanied by authigenic iron sulfide minerals and carbonates (Figure 22a, 22b), an indication for active seepage over a long period [e.g. *Barry et al.*, 1996; *Boetius et al.*, 2000; *Sahling et al.*, 2008; *Suess*, 2014]. Active gas discharge was observed from the ROV at all of the flare sites, with the exception of Flare Site 3, where we did not obtain visual confirmation of the bubble emissions, even though some bacterial mats were observed at this location. Among all the flare sites, Flare Site 4 showed the strongest discharge. It was thus selected to estimate gas flux emissions by quantitative collection of the gas.

In contrast to the activity along the circular rim of the Venere MV, no flare activity was observed directly over the crater of the mud volcano, even though the recent mud flows on the south-east slope of its western summit were mapped and surveyed repeatedly over the 31 day cruise. The mud flows were systematically surveyed with the ROV, with video recording over the entire length of the mud flow, and several transects across the mud flow

were used for detailed photomosaic efforts. The mud flow had a distinct light color with a thin yellow-brownish layer overlying the muds. This thin layer or stain, which increase in thickness and intensity of color in the older sections of the mud flow, may be due to mineral precipitation or oxidation on the mud surface (Figure 22c). In spite of the repeated surveys no chemosynthetic activity was observed in association with the mud flow.

Hydrography data

CTD data from 22 hydrocasts, were used to aid the understanding of the water masses in the region. Results of temperature, salinity, oxygen and density measurements during all stations are presented in Figure 23. Major changes occur only in the in the upper 250 m of the water column and below 1000 m all CTD profiles reveal the same values. The first part of the cruise was sunny and warm followed by a colder period in the second half. This is reflected in the Ionian Surface Water [*Sellschopp and Alvarez*, 2003], where the temperatures strongly vary due to the weather conditions. The water mass below is probably the Levantine Intermediate Water mass (LIW), which is characterized by warm and salty waters during summer [*Lascaratos et al.*, 1999; *Pinardi and Masetti*, 2000].

Since the focus of this study the methane imprint to the bottom water, only the lowermost water mass is of interest. The deepest water mass shows a kink in the TS-plot in Figure 24A below 1200 mbsl and has a southward directed flow. Deep water is formed in the Adriatic Sea and is an important mixing component in the upper Ionian Sea for intermediate waters [*Schlitzer et al.*, 1991; *Sellschopp and Alvarez*, 2003]. Adriatic Deep Water (ADW) has a temperature of 13.3°C and a salinity of 38.663 [*Schlitzer et al.*, 1991]. There is a slight decrease of temperature towards the seafloor around 1250 mbsl from 13.75 to 13.77 °C, with a concomitant salinity decrease of 0.005 PSU (Figure 24A and 24C). This effect is observed at all hydrocasts, including background stations and therefore, fluid flow of warm fresh water by mud volcanism is unlikely. Probably a mixing of the ADW and LIW leads to this temperature increase in the area.

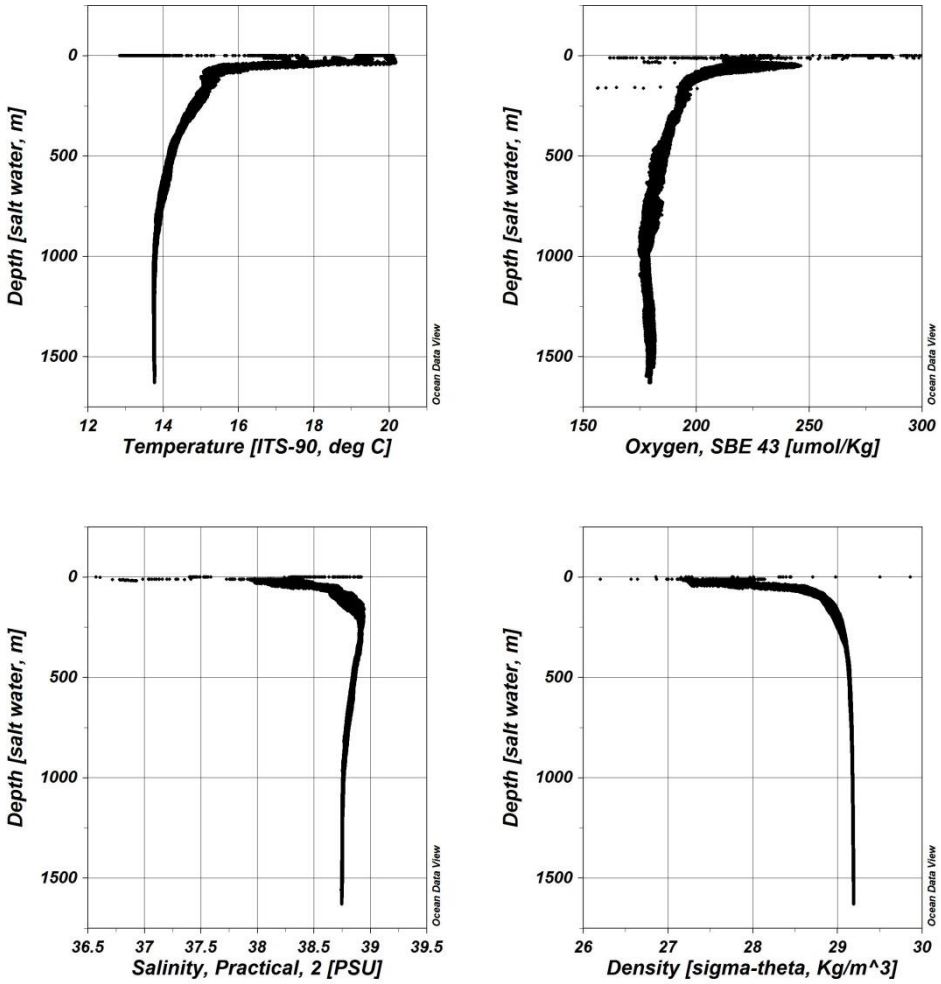

Figure 23: Hydrographic parameters temperature, oxygen, salinity and density over the total water depth. All CTD stations are plotted in one graph and indicate uniform conditions between all stations and stable values especially in the deeper part of the water column.

However, the T-S changes are too small to have a marked effect in density, and a continuous increase in density towards the seafloor is observed at every station (Figure 24B). The CTD data are complemented with results from LADCP measurements obtained in association with deployments of the rosette tool. Table 5 shows the results from processed data, which illustrate prevailing current direction and speed 50 m above the seafloor during the expedition. Unfortunately, the error of these measurements is relatively high with errors of 1.9–2.7 cm/s, in contrast to the low current velocities of 0.9–5.4 cm/s observed. But since the majority of the analyses showed a strong southward trend in current direction, we assume a southward current with a mean velocity of 3 cm/s, which decreases towards the seafloor.

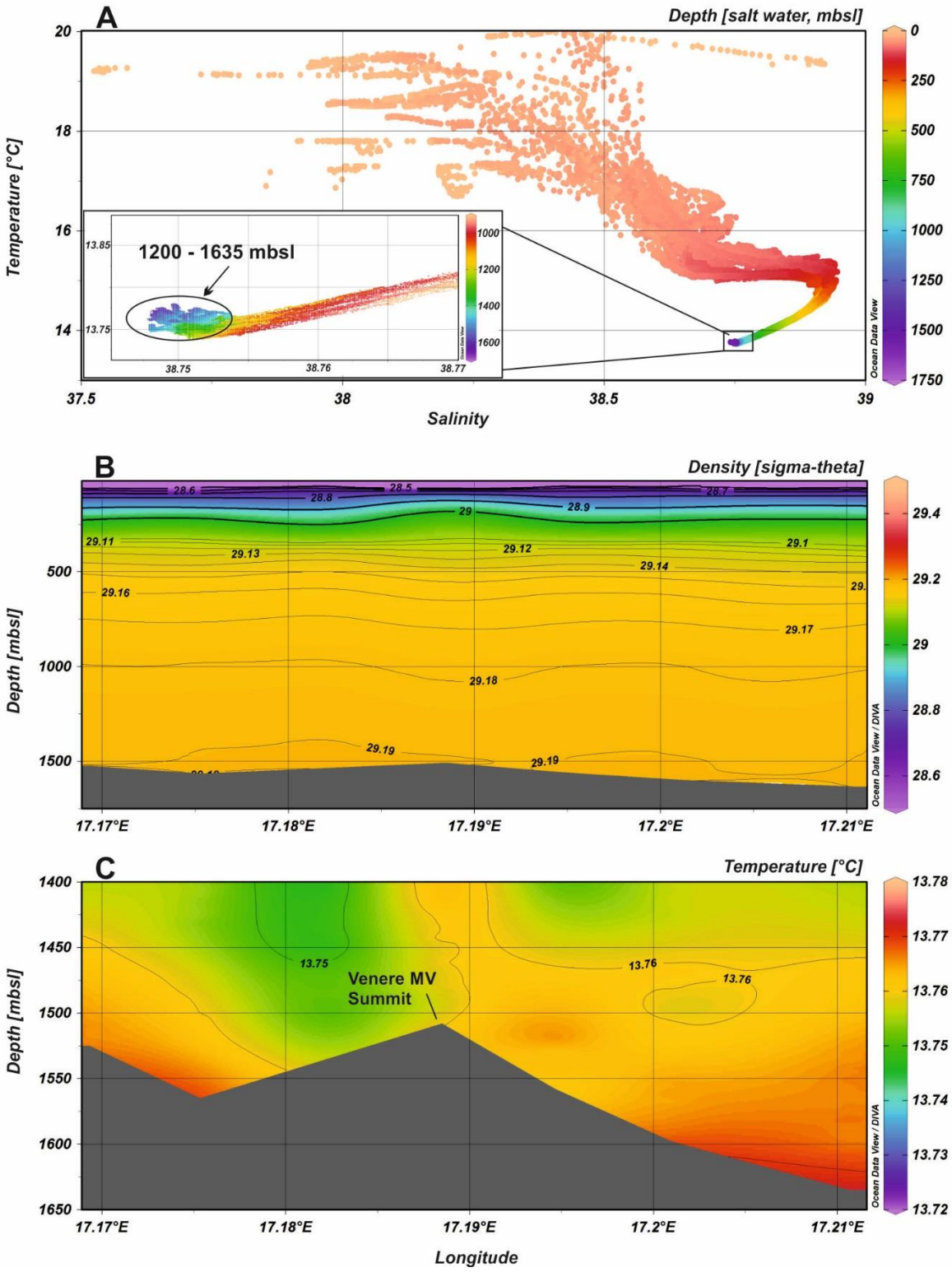

Figure 24: A: TS-diagram with a close up into the temperature decrease below 1200 mbsl, depth is indicated by color scheme on the right side. B: Density plotted over total water depth and along a cross section from west to east crossing the Venere MV in the center. C: Lower part of the water column illustrates the temperature increase towards the seafloor along the same cross section as the plot above (B).

Table 5: Current velocities analyzed 50 m above the seafloor. Velocities are given for East direction (u) and North direction (v) and the combined vector (uv) in cm/s. Current direction is illustrated by an arrow in 360° direction and indicates the southward flowing trend of the bottom water.

Location	CTD	u [cm/s]	v [cm/s]	uv [cm/s]	direction
Flare Site 1	5	2	1.1	2.3	
Flare Site 1	7	1.1	-0.5	1.2	
Flare Site 2	6	1.3	-1.1	1.7	
Flare Site 2	15	-0.2	-3.7	3.7	
Flare Site 3	9	-2.3	-2.1	3.1	
Flare Site 3	10	1.5	-5.2	5.4	
Summit	14	-0.9	-2.9	3.0	
Flare Site 5	11	0.4	-0.8	0.9	
Background	13	-1.7	-0.9	1.9	
Background	16.1	0	-5.6	5.6	
Background	16.2	-1.4	-3.2	3.5	
Background	17	-3.3	-2.3	4.0	
Background	18	-0.9	-2.6	2.8	
Background	23	-1.7	-2	2.6	
Background	24	0.3	-2.2	2.2	

Methane concentrations in the water column

Methane concentration data are illustrated in Figure 25, and the data are listed in Table S1. In all cases, the deepest sample was collected 4 to 5 meters above the seafloor, guided both by POSIDONIA and the CTD altimeter.

Flare Site 1 is the most frequently sampled seep location. Consistent with hydroacoustic data, the highest methane concentrations were detected in the water column over this site at the beginning of the survey, but decrease in magnitude in subsequent visits during the second half of the cruise. CTD-1 shows an increase in methane towards the seafloor, reaching 1754 nM in 1554 m water depth. CTD-3 revealed lower methane values of ~ 15 nM throughout the water column, with the exception of a single sample collected ~ 40 m above the seafloor (at 1526 mbsl), which had 267 nM methane. CTD-5 and CTD-7 each

consist of three lowerings of the rosette to sample the area close to the seafloor at high resolution. Each lowering is positioned ~ 20 m from each other, except CTD-5.1, which follows a transect opposite to current direction (SW) towards the point of maximum flare activity. In CTD-5.2 a high methane concentration of 9715 nM was detected 15 meters above the seafloor, in 1542 mbsl and a high value of 2924 nM was measured in the deepest sample collected in CTD-5.3. In contrast to these high concentrations CTD-5.1 and all casts of CTD-7 showed methane concentrations ≤ 258 nM.

Flare Site 2 was sampled by two CTD stations, visited 3 weeks apart. In general, methane is lower over this flare site, with the highest methane concentration detected in CTD-6, which yielded 62 nM in a sample from 1532 mbsl and 50 nM close to the seafloor at 1582 mbsl. Within the three lowerings of CTD-15, only slightly enriched methane was detected close to the seafloor, with 28 nM in 1590 mbsl (CTD-15.1) and 34 nM in 1588 mbsl (CTD-15.3).

Flare Sites 5 was sampled with two CTDs, each consisting of three lowerings 20–30 m apart that describe a transect over the seep. The highest methane concentrations were observed closest to the seafloor in CTD-11.3 with 331 nM methane in 1598 mbsl. Except for a value of 62 mM at 1558 mbsf, the rest of the water samples from this hydrocast have methane concentrations ≤ 33 nM. All methane concentrations of methane detected in the three lowerings of CTD-12, show a nice increase towards the seafloor, with a maximum value of 61 nM in 1593 mbsl (CTD-12.1) and a concentration of 44 nM 1598 mbsl (CTD-12.3).

CTD stations 13, 17 were positioned along the canyon structure in the southern part of the study area. CTD-23 was taken in the southwestern part of the study area, in an elongation of this seafloor canyon. Even though no bubble emissions are observed at these locations CTD-13 and especially CTD-17.1 show high methane concentrations of up to 172 nM in 1591 mbsl. CTD-13, although not that enriched in methane, show a methane peak close to the seafloor with a high value of 82 nM in 1595 mbsl (CTD-13.2) and 23 nM in another lowering at this site (CTD-13.1). A well-defined peak was observed in 1550–1562 mbsl in both lowerings of CTD-13, with a maximum concentration of 17 nM methane. Methane concentrations in both lowerings of CTD-23 are below 3.5 nM.

CTD stations 16, 18 and 24 were taken along a NW-SE transect in the study area, away from seepage sites. Samples from the two lowerings of CTD-16 and CTD-18 all had low methane concentrations, with a small peak observed between 1488 and 1513 mbsl with a maximum concentration of 8.9 nM methane (CTD-16.1). Water samples from CTD-18 also show a small enrichment in methane in 1583 mbsl, with values of 9.5 nM and 6.7 nM in CTD-18.1

and CTD-18.2, respectively. The deepest station in the study area was sampled with CTD-24, which shows relatively higher methane concentrations and two clear methane peaks in the water column. The first peak was observed in 1561 mbsl with 18 nM methane and the second peak appeared several meters above the seafloor in 1610 mbsl with a methane concentration of 49 nM.

The lowest methane concentrations were detected in the water column above the Venere summit. In CTD-9, methane concentrations range from 1.4 to 2.4 nM. The station taken in the center of the rim structure (CTD-10), on the southeastern flank of the mud volcano, shows only a slight enrichment, with a maximum value of 9.6 nM close to the seafloor in 1508 m of water. This is only slightly higher than the values measured at the summit, even though this station was close to Flare Site 3. CTD-14 was specially designed to target bottom water around the mud extrusion site and to follow the fresh mud stream. In total 7 lowerings were performed with each 3 water samples close to the seafloor and the lowermost sample around 4 masf. Most of the samples were similar to CTD-9 with background concentrations around 2 nM, only two samples were elevated with 12 and 23 nM.

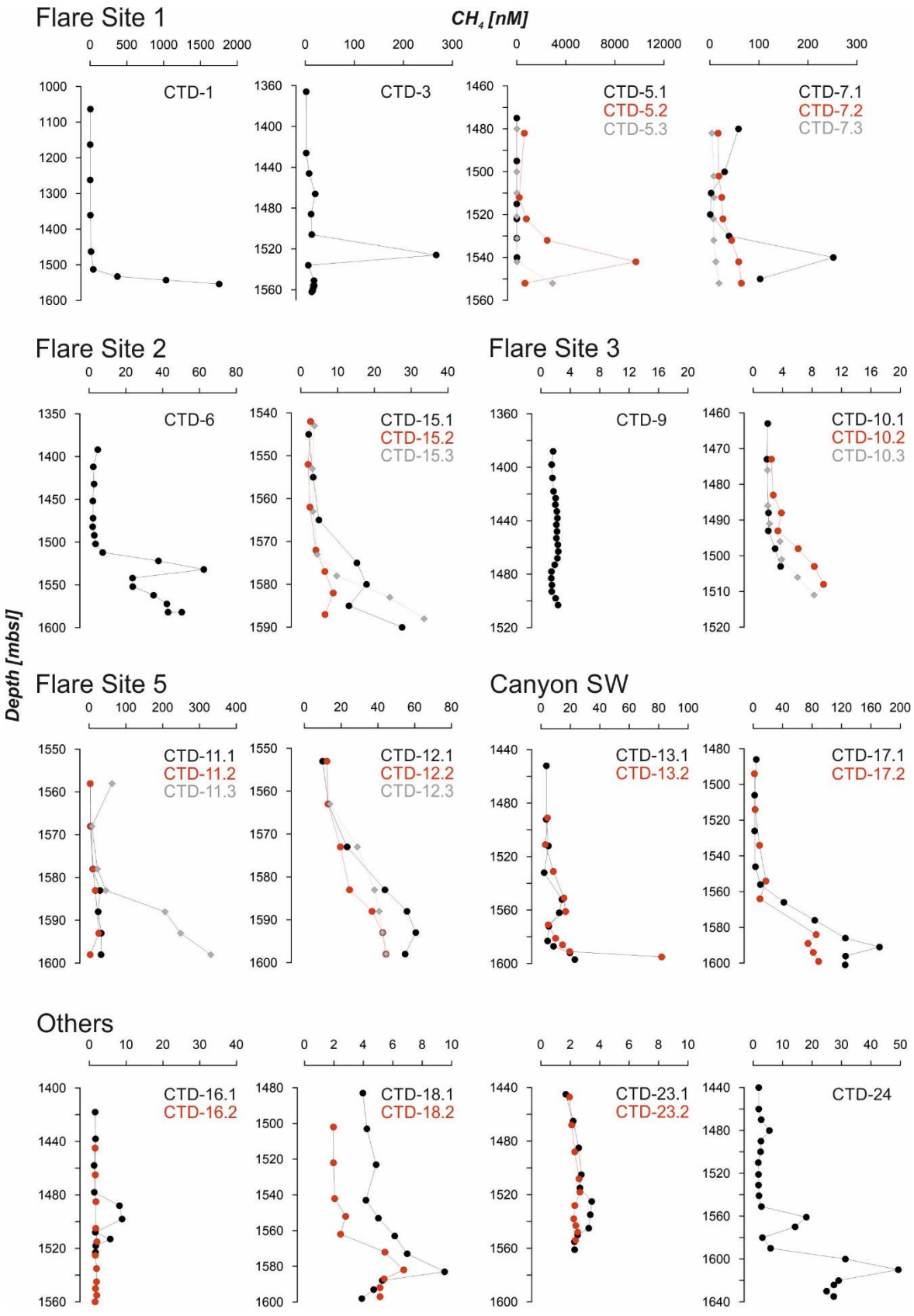

Figure 25: Methane concentrations in the water column collected with the CTD. In case of multiple lowerings during one CTD cast, two or three plots appear in one graph. Please note the different scale of both axes (methane and depth) in all plots.

Methane concentration in bottom water samples

The methane concentration in waters sampled by the GBS were, not surprisingly, much higher than the water column sampled with the rosette-CTD, and therefore, the concentrations are given in µM. (Table 6). Even though the water column above the flare sites had much higher methane concentrations (Figure 25), the highest methane concentrations in bottom waters collected with the GBS were in a sample collected immediately above the fresh mud-flow extruding from the Venere crater. This sample (GBS-9) had a concentration of 566 µM. The water at this location was also sampled 3 and 4 meters above the seafloor, which yielded values of 3 µM (GBS-10) and 4 µM (GBS-11) of methane. GBS-20 and GBS-5 show high concentrations of 171 µM and 30 µM. The other GBS samples taken at the summit area have lower methane concentrations ranging from 0.4–4 µM.

GBS water samples were also collected ~1 m above the seafloor at the location of the flare sites. At Flare Site 1, a methane concentration of 465 µM was observed in GBS-3. The highest concentration at Flare Site 5 was measured in the water sample from GBS-8 with 150µM methane. The maximum concentration at Flare Site 4 was detected in GBS-12 with 63 µM methane. The lowest concentration of methane in water samples collected directly above seep sites was measured at Flare Site 2, where the maximum value reached only 6.2 µM in GBS-2 and 0.02 µM in GBS-22.

Gas composition

A gas sample was collected from each flare location, except for Flare Site 3 because no bubble emissions were found during the two ROV dives in that area. All other samples show a methane concentration of > 99.9 % methane in relation to higher hydrocarbons (ethane, propane, butane, pentane) which is represented in a C_1/C_{2+} ratio > 1000 (Table 3). The analysis of isotopic composition of the carbon in methane ($\delta^{13}C\text{-}CH_4$) resulted in values between -45.67 and -47.23‰ (Table 7).

Table 6: Methane concentrations in the bottom water sampled with the GBS. Note that methane concentration are given in µM, and are therefore much more enriched in methane than other water column samples. An isotopic composition of dissolved methane is given in GBS-3 and GBS-9.

Location	Station no.	Tool	Depth [mbsl]	CH_4 [µM]	$\delta^{13}C\text{-}CH_4$[‰]
Flare Site 1	GeoB 19221-7	GBS-1	1568	22	-
Flare Site 1	GeoB 19230-2	GBS-3	1567	465	-47.4
Flare Site 1	GeoB 19230-11	GBS-4	1568	0.5	-
Flare Site 2	GeoB 19224-3	GBS-2	1595	6.2	-
Flare Site 2	GeoB 19267-2	GBS-22	1597	0.02	-
Flare Site 2	GeoB 19267-11	GBS-23	1596	0.3	-
Flare Site 2	GeoB 19267-12	GBS-24	1595	2.1	-
Flare Site 3	GeoB 19258-3	GBS-19	1515	0.7	-
Mud Flow	GeoB 19232-8	GBS-5	1509	30	-
Mud Flow	GeoB 19232-9	GBS-6	1506	0.4	-
Summit	GeoB 19242-5	GBS-9	1499	566	-47.5
Summit	GeoB 19242-19	GBS-10	1498	2.8	-
Summit	GeoB 19242-20	GBS-11	1496	4.0	-
Summit	GeoB 19258-19	GBS-20	1502	171	-
Summit	GeoB 19258-20	GBS-21	1499	0.9	-
Flare Site 4	GeoB 19249-11	GBS-12	1606	63	-
Flare Site 4	GeoB 19252-8	GBS-13	1607	4.8	-
Flare Site 4	GeoB 19252-12	GBS-14	1606	10	-
Flare Site 5	GeoB 19240-7	GBS-7	1605	0.4	-
Flare Site 5	GeoB 19240-14	GBS-8	1607	150	-

Table 7: Molecular gas composition given in the hydrocarbon ratio (C_1/C_{2+}) and isotopic carbon composition ($\delta^{13}C\text{-}CH_4$) of methane from all sampled flare sites.

Location	Station no.	C_1/C_{2+}	$\delta^{13}C\text{-}CH_4$ (‰)
Flare Site 1	GeoB 19221-2	1855	-46.76
Flare Site 2	GeoB 19224-2	1080	-45.67
Flare Site 4	GeoB 19249-2	1153	-46.67
Flare Site 5	GeoB 19240-2	1176	-47.23

DISCUSSION

Methane sources

In a study of several mud volcanoes, *Deville et al.* [2010] describe the presence of a concentric ring fault system around mud volcanoes with a "downward tapering fault cone". According to these authors, water and gases migrate upwards along these faults, which tap two different sources: the center channel migration of muds and gasses from greater depth, whereas gas and aqueous fluid migration along the ring fault may be sourced from a shallower system. Most of the flare locations in the Venere MV occur in a circular pattern around its two summits (Figure 21), consistent with the simplified model of *Deville et al.* [2010]. In addition to samples taken in the area of flare activity along the rim, CTDs 13, 17 and 24 also revealed high methane concentrations in the bottom water (82 nM, 172 nM, 49 nM). They are located near a clear tectonic edge but are not associated with documented flare activity during our cruise (Figure 21). No ROV surveys were conducted in these locations, but it is conspicuous that all three stations were located at the concentric rim structure around the MV summit, which is the postulated pathway for fluid migration [*Deville et al.*, 2010]. Collectively our observations along the concentric rim structure surrounding the Venere crater document transport by fluids and discharge to the bottom water both via gas and in the dissolved phase, creating a methane source to the area.

Whereas our observations along the rim support the model for fluid discharge of *Deville et al.*, [2010], Flare Site 3 is located in the center of the rim, revealing that a gas pathway also exist in the center of the MV and not only along the outer faults. Furthermore, this observation may indicate a closer connection between the gas at the flare sites and that in the gaseous mud. Gas samples collected at the flare sites point to a single gas source, since the results vary only by 1.5‰. The isotopic composition (-45.7 to -47.2‰) of the gas samples is indicative of a thermogenic origin [*Whiticar*, 1999], but the lack of higher hydrocarbons ($C_1/C_{2+} > 1000$), suggests a microbial generation of methane [*Whiticar*, 1999]. Most probably the gas has a thermogenic source partially mixed with biogenic methane. Gas analyses were complemented with two strongly enriched methane samples in the bottom water, which were also analyzed for their isotopic composition: one taken at Flare Site 1 (GBS-3) and the other collected right above the mud extrusion center (GBS-9). Surprisingly, both samples show the same isotopic composition (-47.5 ± 0.1‰), which is also similar to the isotopic composition of gases collected from all flare sites. Advective transport of methane in the bottom water from Flare Site 1 to the summit can be excluded,

since the distance is quite large and the methane concentration analyzed at the summit is higher as the concentration at Flare Site 1. Since the flares are organized in a circular pattern around the mud volcano with an additional flare site close to the summit, it is possible that the flares and the mud flows are tapping similar sources, which can explain the similarity in the isotopic composition of samples collected over the flares and summit areas. Alternatively, our observations could just be the product by mixing and dilution with surrounding bottom waters. Additional data from different seepage sites both in the water column and the subsurface, and measurements of microbial activity in the water column are needed to fully constrain the methane sources delivered via discharge of gases and mud flows in the area around Venere MV.

Activity and variability over time

Mud volcanism is known to be episodically with long periods of quiescence interrupted by eruptions [*Dimitrov*, 2002; *Kopf*, 2002; *MacDonald and Peccini*, 2009]. So far nothing is known about the episodicity of mud eruptions at Venere MV. Since the mud is still degassing strongly resulting in very high methane concentrations (171 and 566 µM measured immediately above the flow), the most recent mud flow has to be relatively young. Together with the active seepage close to the summit at Flare Site 3 and the surrounding flare sites, this mud volcano is clearly in an active period. We analyzed the variability of seepage surrounding the mud volcano over a short time scale of 31 days and determined a strong variability in flare intensities (Figure 26). The strongest seepage was detected at Flare Site 1 on the first part of the cruise and during the second part the flares were off or only very weak. Seepage is mainly dependent of the gas supply from below [*Kopf*, 1999], which seems to be very variable, but no consistent pattern or correlation between the flares or with the tidal system was observed. However, all CTD stations were taken during strong or medium flare intensities and thus represent strong methane input.

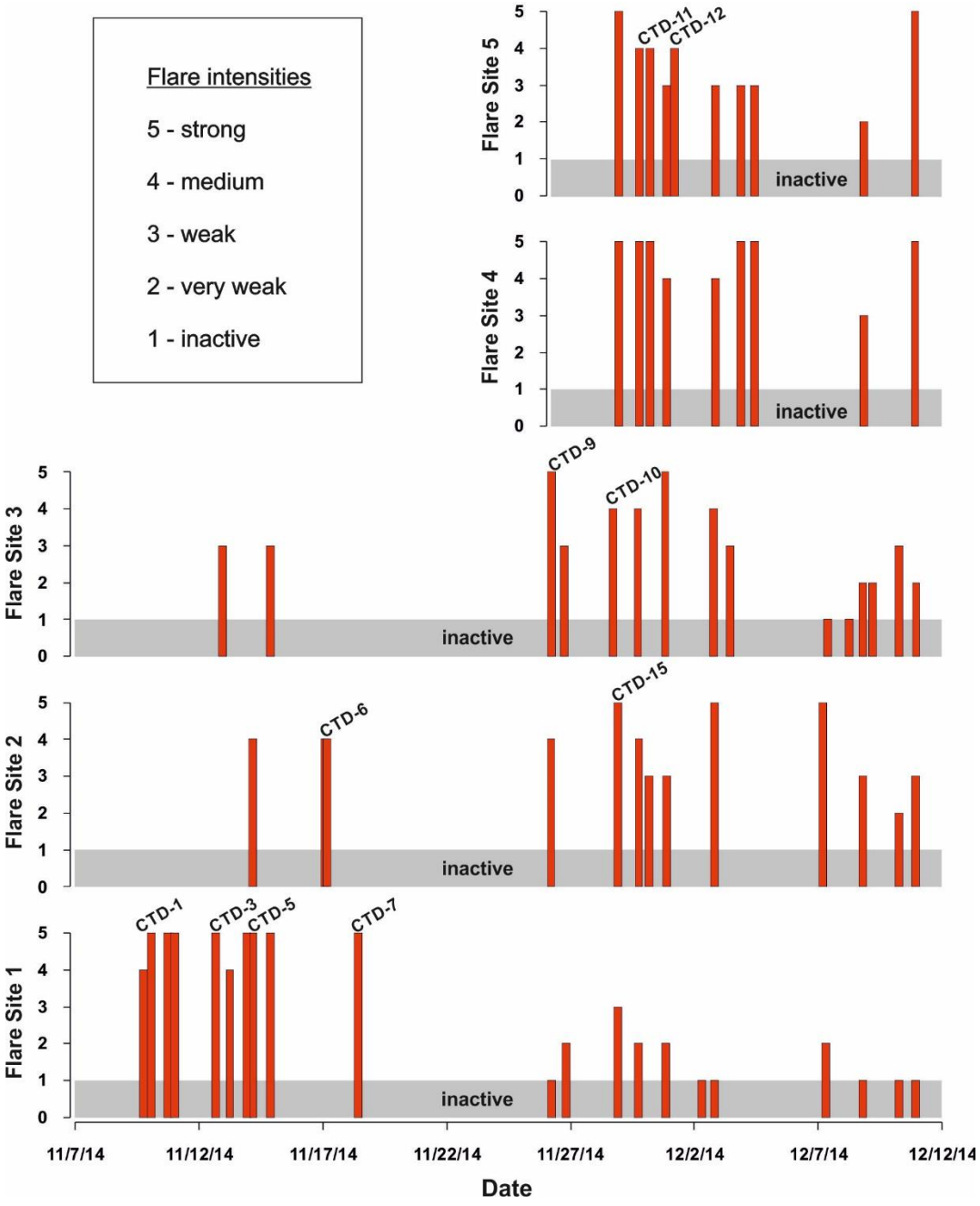

Figure 26: Variability of seepage over time. Repeated surveys over 31 days above the flare locations identified a strong variability of the intensity in bubble emissions.

Methane distribution associated with flare activity

Figure 27 summarizes the methane distribution in the vicinity of the flares and clearly illustrates an extremely rapid decrease in dissolved methane concentration with vertical and horizontal distance from the bubble emission sites. Methane concentrations above 1 µM (10 µM at Flare Site 1) are only detected very close to the sea floor (0.5–1 masf). The

huge difference in concentrations between samples collected by ROV and by hydrocasts samples could be the result of using different methods. GBS samplers were accurately positioned above the seafloor, prior to collecting sediment cores or disturbing the sediment, but they are collected in gas-tight samplers under in situ pressure.

The Niskin bottles were positioned with aid of POSIDONIA navigation and a CTD altimeter, with the lowest bottled tripped 4 to 5 m above the seafloor; however, Niskin bottles are not fully gas tight and may lose some of the methane during the upcast of the CTD. Notwithstanding a potential sampling effect, a general decrease from depth is also observed in the CTD profiles (Figure 24). The dissolved methane plume defined by our water sampling is relatively stationary with a horizontal distribution of 20–50 m and a vertical expression of only 5–10 m.

Figure 26 also allows for direct comparison of water column measurements with bubble plumes imaged hydroacustically. Because of the repeated nature of the surveys and the highly accurate positioning of the water sampling (guided by POSIDONIA and ROV navigation), we can directly compare these observations. In all cases, the dissolved methane signal is limited to a much thiner portion of the water column (<10 m) than the flares that rise from 70 to 230 m from the seafloor. This comparison holds even if we consider only Flare Site 1. Here, gas bubbles were observed to reach 150 m above the seafloor and the water column shows a methane decrease already in 50 masf (Fig 24, CTD-1). Recent analyses of gas plume dynamics have shown that methane gas emanating from the seafloor is rapidly lost out of the gas bubble by exchange with other gases present in the water column, so that even when bubble plumes are imaged high above the seafloor, these do not necessarily represent methane transport [*McGinnis et al.*, 2006; *Greinert and McGinnis*, 2009]. These authors show that most of the methane leaves the bubble in the lower meters, depending on water depth and possible hydrate or oil coatings. Our combined acoustic imaging and water sampling approach is consistent with the methane transport behavior out of bubbles, and results in highly restricted dissolved methane plumes over the flare sites around the Venere MV.

Methane distribution associated with the mud flow

The methane distribution above the mud extrusion site at the summit is very similar to that observed at the flare locations. However, at the summit, there is no gaseous methane input; rather, all the methane is released from the methane-bearing mud flows in dissolved phase.

Three bottom water samples (GBS-9, GBS-10, GBS-11), collected 1 m, 3 m and 4 m as the ROV ascended above the extrusion site, provide excellent documentation of the strong gradient in the water column, which we calculated to be 187.3 µM/m (Figure 27). Methane concentrations directly above the mud flows are significantly higher than those measured in the vicinity of methane gas emission, showing the significance of these flows as methane sources to the bottom water. These observations document, for the first time, the high potential of methane supersaturated muds to impact the bottom water methane budgets, which may be comparable or even higher than the methane input in the gaseous phase at flare sites

Methane input calculations

The unique conditions offered by the Venere MV permit a direct comparison between the diffusive and advective methane contributions in an active mud volcano. To constrain the gas contribution, we use estimates of the gas volume flux obtained by measuring the time needed to fill the known volume of the GBS funnel (Figure 22b). The volume flux in milliliter (ml) per minute (min) was then converted to a mass flux (mol CH_4 per time) after a calculation described in *Römer et al.* [2012]. Methane at high pressure does not behave as an ideal gas, and therefore, the compressibility factor (Z) has to be defined. To get the value for Z an online tool called Pipeng was used (Pipeng: Methane gas compressibility Z factor and gas density. Website: www.pipeng.com/index.php/tsps/itdtoflup00401/). To calculate the mass in mole (n) the product of pressure (P) and volume (V) is then divided by the product of Z, temperature (T) and (R), the ideal gas constant (n = PV/RTZ).

Using this approach, the methane input was estimated from one bubble emission site at Flare Site 4 and resulted in a gaseous methane flux of 0.39 mol/min. This is based on just one measurement, but it represents the most active seepage site during the entire survey time. Most of the gas emissions are significantly weaker than the one at Flare 4, and furthermore, gas discharge along the rim is highly episodic. But even if we were to assume that all the flares are releasing gas at this high rate for 50% of the time, the total advective input of methane in the gas phase is in the order of 1 mol/min.

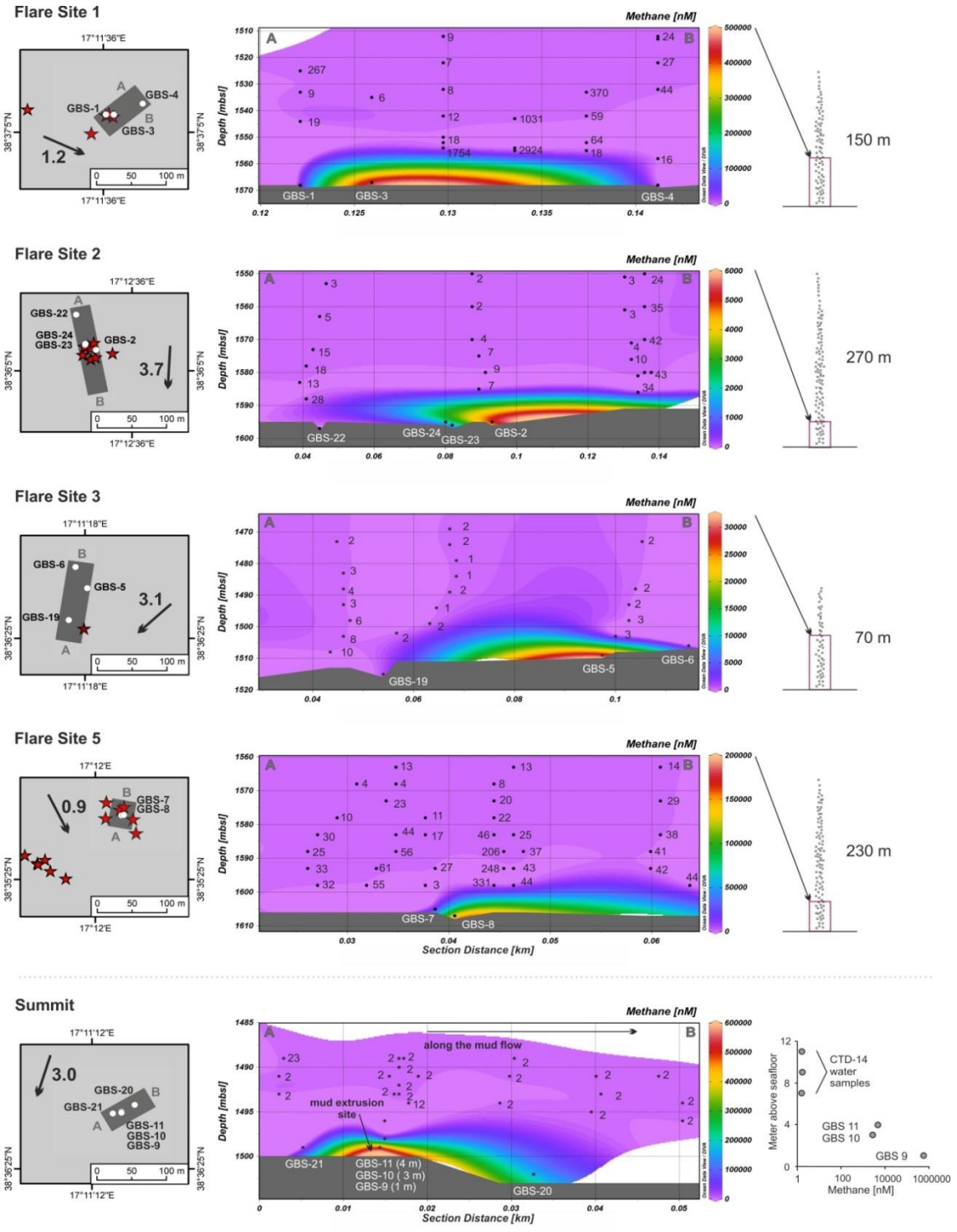

Figure 27: Vertical and horizontal methane distributions close to the seafloor of our study area. The grey maps on the left show the surface distribution of flares (red stars), the location of the GBS in relation to the flares, the current direction and velocity in cm/m (black arrow) and the profile from A to B which was chosen to display the methane distribution (plot in the middle). For gridding the data in OCEAN DATA VIEW(ODV) the DIVA grid was chosen. The panels to the right show the maximum flare height, the red box demarks the water depth covered in the dissolved methane sections. Methane distributions at the Venere MV summit are shown in the lowermost panels. The plot on the right shows the strong methane gradient, which was observed in water samples taken above each other at the extrusion site.

To estimate the vertical diffusive input of methane into the water column from the mud flow we used calculations described in *Mau et al.* [2015]. The diffusive flux (DIF = ∂ (∂[CH_4]/∂x)) is calculated by the diffusion coefficient ∂ and the spatial concentration gradient (∂[CH4]/∂x) of 187.3 µM/m based on the GBS samples taken above the mud extrusion site. For the vertical diffusion coefficient a value of 0.0001 m^2/s was chosen. The vertical diffusion yields a value of 11 mol/min for an area of 10 m^2 representing the mouth of the mud extrusion above the feeding channel. This diffusive flux is higher than the vertical bubble flux at Flare Site 4.

Samplers GBS-6 and GBS-5 sampled the water directly above the mud flow at 110 m and 140 m away from the extrusion center and indicated a loss of diffusive methane input along this mud flow. To fully constrain the diffusive input of the mud in dependency of the mud age and distance to the extrusion center a more detailed sampling of bottom water along the mud flow would be required. Nonetheless, for comparison purposes we extrapolate this diffusive flux over a fresh mud area very conservatively estimated to be of 100 m^2, and arrive at a methane flux from the mud flow that is about two orders of magnitude higher with ~ 112 mol/min than that estimated for the flare emission sites taken as a whole.

It is interesting to consider that the flare sites are characterized by the presence of biological and mineral assemblages typical for seep sites [*Bohrmann et al.*, 2014, cruise report], where anaerobic oxidation of methane acts as an efficient biofilter that prevents methane release to the overlying water [*Hinrichs et al.*, 1999; *Boetius et al.*, 2000]. In contrast to the black, H_2S bearing sediments recovered from the vicinity of the flare sites, the white mud breccias discharging at the summit of the Venere MV had no indication of chemosynthetic activity, and the methane-rich muds had no evidence for sulfide presence [*Bohrmann et al.*, 2014, cruise report]. These observations, and the higher methane flux from mud flows relative to that estimated for the flare sites highlights the importance of microbial communities in consuming methane before it can reach bottom waters. Because AOM communities take time in establishing, recent mud flow activity may have a significant effect on methane discharge because it is not diminished by microbial activity when the mud reaches the seafloor. Ongoing characterization of the microbial communities from flare sites and the mud flow will provide additional data to constrain the role of the deep biosphere in regulating methane release from these and other mud volcanoes.

Rates of extrusion for the Milano and Napoli mud volcanoes have been estimated to be in the order of 3.4–7.8 km^3/yr and 9.5–14.6 km^3/yr, respectively [*Kopf*, 1999]. These volumes were used by *Wallmann et al.* [2006] to estimate the methane discharge rates of 0.2–

$0.7*10^6$ mol/yr and $0.5–1.3*10^6$ mol/yr for the Milano and Napoli MV systems. Our flux estimate based on GBS data over the Venere summit is $5.9*10^6$ mol/yr, and given the uncertainty of all these calculations, it is reasonable to arrive at a common flux rate in the order of 10^6 mol[CH_4]/yr from the various Mediterranean mud volcanoes investigated to date.

Methane fate

We estimated first order advective and diffusive transport of methane in the water column. We used a horizontal diffusion coefficient of 100 m^2/s and a concentration gradient of 56.5 µM/m to estimate the diffusion. The bottom water current out LADCP data in 5 m above the summit yields a velocity of 1.5 cm/s and was multiplied with the max. methane concentration to calculate the advecting component [*Mau et al.*, 2015]. We then arrive at horizontal diffusive flux estimates in the order of $3*10^6$ mol/min and corresponding advective horizontal transport of $5*10^3$ mol/min. Transport in the vertical direction is much slower (11 mol/min). That explains why the shape of the concentrated methane plume is only a few meters high but extends much farther in the horizontal direction.

The methane input to the bottom water does not reach surface waters, nor is it transported in the bottom water to any significant extent, since the methane plumes were not tracked in water surrounding the seeps. The plumes appear to be stationary and stay very close to the seafloor. The mud is degassing constantly over time and may provide a stable supply of methane to oxidizing bacteria. Our observations to date suggest that microbial aerobic oxidation may dominate the horizontal or vertical loss terms. It would be interesting to characterize the microbial response in the water column over mud, follow areas in Venere and elsewhere, to constrain this methane sink term especially in regions where communities responsible for anaerobic oxidation of methane are apparently not well established.

CONCLUSIONS

The Venere MV is an active mud volcano in the Calabrian Arc. Flare sites are located in a concentric rim around the active summit and show a strong variability in bubble emissions. Migration of fluids and gas at the outer rim seem to be connected to the main feeding channel of the mud volcano, because of the presence of a bubble emission site close to the summit and based on similar isotopic carbon compositions of methane in the bottom water.

Strongest seepage was observed at Flare Site 1, resulting in high methane concentration in the overlying water column. However, the created methane plume stays in the lowermost water and high methane concentrations are restricted to the lower 100 m above the seafloor.

The highest methane concentrations were detected above the mud extrusion center and along the mud flow. This indicates that fresh mud is an important and enormous source for dissolved methane in surrounding waters. Calculated fluxes confirm the strong input by the mud, which is even higher than the advective input calculated using rates directly measured at a bubble emission site and extrapolating to the entire flare system.

ACKNOWLEDGEMENTS

We would like to thank the shipboard support from the master and crew of the research vessel Meteor during cruise M112. We are grateful to Prof. Dr. Monika Rhein for providing the LADCPs and to the team of ROV QUEST 400 m for their good assistance. We are also grateful to Stefanie Buchheister and other cruise participants for their help with water sampling on board. This work was supported by the DFG-Research Center/Cluster of Excellence "The Ocean in the Earth System" MARUM. We also acknowledge support to M.E. Torres via a fellowship from the Hanse-Wissenschaftskolleg (HWK), federal states of Bremen and Lower Saxony. Patrizia Geprägs was further supported by a DAAD Grant (57044996) "Kurzstipendium für Doktoranden".

CHAPTER 5: CONCLUSION

CONCLUDING REMARKS

The new method was successfully used during two research cruises and achieved very good results. The collected data was used for comparative studies in Chapter 3 and for the second case study in the Mediterranean Sea. A major improvement compared to previous methods is demonstrated by the significantly increased number of samples between the study in South Georgia and the Calabrian Arc. Moreover, colleagues used this method during a third expedition in the Arctic after only a short briefing which proved another benefit - easy handling of the method and simplicity of the application.

The case studies in this thesis represent two very different settings, one in the Southern Ocean and one in the Mediterranean, but, nevertheless, both indicate that methane seepage has no impact on atmospheric methane concentrations. The released methane from South Georgia probably originates from a shallow biogenic source, whereas fluids of the Venere MV in the Mediterranean are thermogenic, generated in depth and might be mixed during their ascent with a shallower biogenic gas. Pore water data in South Georgia indicated AOM as an efficient filter for methane in the sediments. Only directly above the bubble emission sites methane was traced in the water column. Seepage at the Venere MV was much more pronounced, therefore, a larger amount of methane was released into the overlying water column. Diffusive sediment fluxes were not determined at the Venere MV, but they were expected to often exceed the benthic filter based on very high methane concentrations detected in the water and, thus, suggesting stronger fluxes from below. Seepage in South Georgia only resulted in methane concentrations of about < 60 nM. Strong stratification in the water column and horizontal transports limited methane release into the atmosphere although the water depth was relatively shallow with 250 mbsl. The Venere MV is located in deeper water at around 1500-1650 mbsl but, despite very high initial methane concentrations, hardly any methane was detected 100 m above the seafloor. In both cases, available data suggests that a methane plume was formed only close to the seafloor, although bubbles were rising much higher. This illustrates indeed how important bottom

water samples are to fully understand methane behavior in the water column, especially close to the seafloor (Figure 28).

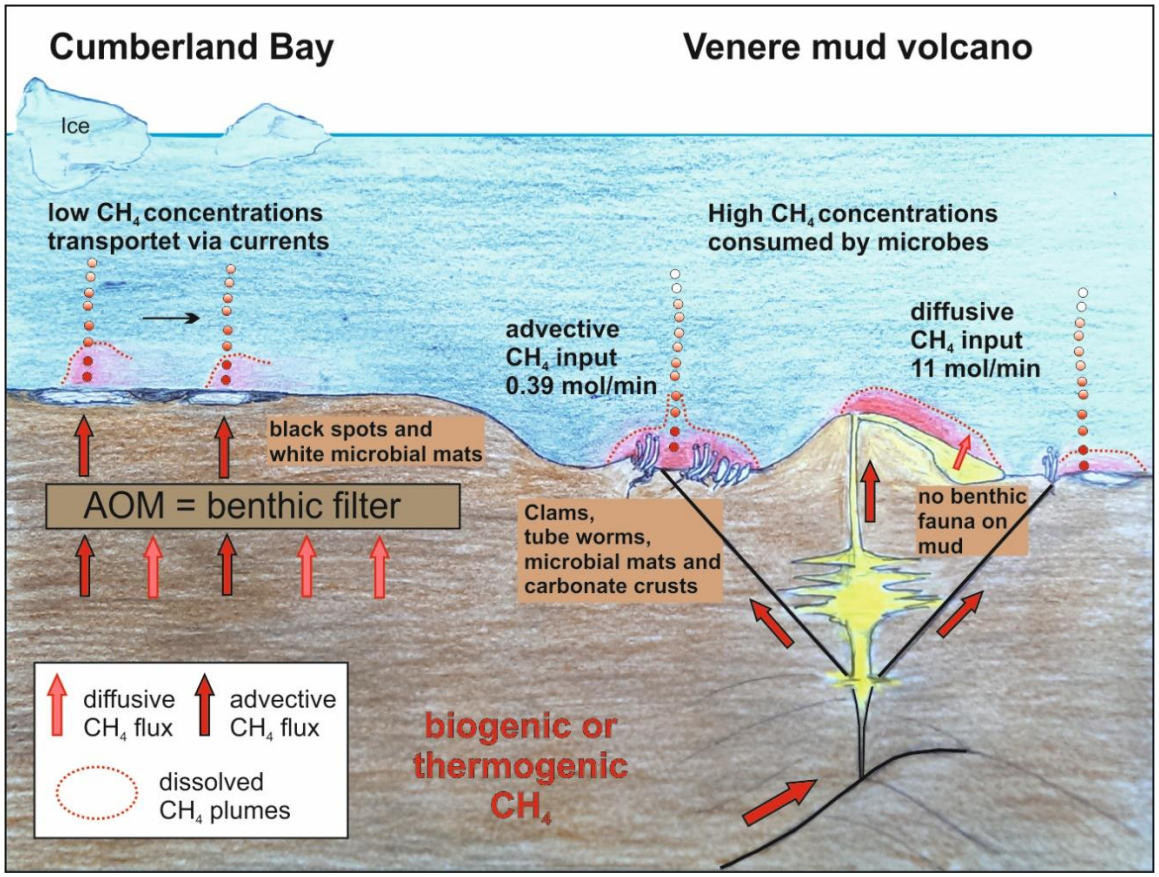

Figure 28: Methane input into the water column. In the Cumberland Bay, South Georgia, only low methane concentrations were detected close to the seafloor and transported and diluted in the lowermost water mass. Most of the methane was microbial oxidized by AOM within the sediments. Methane input at the Venere mud volcano in the Mediterranean is much higher but methane plumes are also only located close to the seafloor. The determined methane fluxes from an active bubble emissions site is very low compared to the diffusive input of methane above fresh extruded mud and most of the methane is probably consumed by microbial oxidation in the water column.

The overall impact of seepage from South Georgia seems to be small. However, only a few sites have been sampled so far and due to strong variabilities in seepage activity the impact may change over time. Even though seepage could not be linked to melt water or other global-warming related processes, these sites still have to be observed in the future in this regard. South Georgia and especially the shelf areas are known for high primary productivity and, therefore, if enough organic matter is available in sediments, seepage will play an important role in that area for the next centuries.

The dissolved methane flux above the freshly extruded mud was significant and seemed to be even higher than the methane input observed at bubble emission sites. Diffusive input had been thought to be smaller than advective input from gas flares [Krooss and Leythaeuser, 1996; Etiope and Martinelli, 2002], then Wallmann et al. [2006] proposed that at mud volcanoes, the advective input might be as high as the diffusive input. In fact, this study shows that the diffusive input was underestimated and that it might be much higher than the advective input from gas flares. Even though, it also needs to be considered that methane diffusing from fresh mud is not consumed by AOM immediately. If there is sufficient methane available and AOM evolves over time, this benthic filter will decrease the methane emissions from mud flows at the Venere MV as it is observed at many other sites.

REMAINING LIMITATIONS

CTD sampling in high water depth, especially with strong currents, remains challenging. Despite utilizing a positioning system for the CTD, it is difficult to guide the ship and the CTD to the right position. A horizontal offset to the target of only 10 meters can already change methane concentrations dramatically in the order of two magnitudes or more. Without visual guidance it is often very difficult to estimate a realistic distance to the seepage site. Another problem that arises due to "blind sampling" is the capture of gas bubbles while closing the Niskin Bottles. Gas bubbles will dissolve during the recovery of the CTD and will increase the residual methane concentration in the water sample. In contrast to this additional input of methane, it is still not known how much methane escapes out of the sample bottle by pressure release during recovery. In order to investigate this loss, it is intended to compare an in-situ pressurized water sample taken by the GBS with a water sample taken by a CTD in a future study.

Moreover, it has not been examined yet to what extent the rotor movement of an ROV changes the local water current regime and how strong these turbulences affect methane concentrations. Furthermore, it should be taken into account that if the ROV sits on the seabed before sampling, due to compression of sediments higher-concentrated pore waters might mix with the ambient and lower-concentrated bottom water.

At both seepage sites the sink of methane was determined by exclusion of two from three possibilities: (i) Methane is transported vertically into the atmosphere, (ii) methane is transported horizontally or (iii) methane is microbially consumed. No horizontal methane transport out of the Cumberland Bay or oxidization close to the seafloor at the Venere MV

was actually observed. Follow-up surveys of the same locations are planned and might address these uncertainties in order to find further evidence in support of the theory stated in this thesis.

OUTLOOK

In addition to the already mentioned suggestions in the previous section, two cruises are planned to continue investigations in South Georgia and on the Calabrian Arc. The next expedition in the Calabrian Arc is scheduled for May 2016. As a first step, the study area should be searched for gas flares and new mud flows. These findings can then be used to investigate the variability of seepage over a period of 1.5 years and to determine if existing seeps are still active or have shifted or if new seeps have been formed. An area of particular interest is the SW canyon structure, where high methane concentrations have already been detected. Furthermore, if new mud flows are identified a more detailed sampling strategy needs to be laid out to determine the overall input of methane by a mud eruption. In case no new mud flows are found current methane fluxes can be compared with flux rates from 2014. Since the methane input from the mud flow was overly high at that time, a comparison of recent and past flux rates can give an estimate about the required time for mud to degas completely. Further, it can be observed how this mud flow evolved over time, if AOM is taking place and if chemosynthetic life such as clams and mussels settles down on the mud surface or if there is any microbial mat formation? But most importantly, as long as there is active seepage, water samples should be taken to determine methane oxidation rates in the bottom water.

The next expedition to South Georgia is planned for 2017, four years after the first investigations. One of the main scopes of work is to find out if there is still active seepage and if seepage has increased. By using the new method, a more comprehensive water column sampling is possible. Moreover, the hydrographic conditions and water currents have to be investigated and methane turnover rates observed in order to ascertain if they are at similar low levels or if they have increased over the years. And are maximum turnover rates still located above the plume rather than at the deepest point, where the highest concentrations occur? Further questions that need to be answered concern potential regional limitations of methane oxidation. Seepage sites in the Cumberland Bay West should be considered as well, with the intent to calculate a budget of in- and outflows in the bay.

As explained before, bottom water samples are a crucial contribution to the understanding of seep systems and their related methane flow regime. Sampling of bottom water (0–5 m above ground) with a certain spatial coverage requires a remotely operated vehicle (ROV). However, manual sampling by an ROV or a CTD and analysis afterwards is a very time-consuming process and also connected with a certain amount of sample loss during transport. In-situ analyses performed by mass spectronomy (in-situ MS) for both long-term and short-time have become of increasing interest. Justifiably so, the advantages of small in-situ mass spectrometers are enormous. These devices can be attached to an ROV or autonomously operated vehicle (AUV) and continuously analyze methane while the ROV/AUV is mapping and sampling. They also can be deployed for long-term observations, are suitable for water depths up to 6000 mbsl and can be used for other substrates than methane as well. Furthermore, the inlet membrane system allows only dissolved methane to enter the analyzer [McMurtry et al., 2012]. This reduces overestimation of the dissolved methane concentration caused by gaseous bubbles in the Niskin bottles or sampling device. During the last three years several new tests and developments have been conducted and, therefore, these in-situ MS will most likely be the future technology for methane detection and investigations at cold seeps. But until this technology is ready to use, the developed method in this study represents a good alternative for rapid and accurate methane analysis in the water column.

ACKNOWLEDMENTS

First of all, I want to thank my supervisors Prof. Dr. Gerhard Bohrmann and Prof. Dr. Marta Torres. I want to thank Gerhard Bohrmann for giving me the opportunity to do a PhD in his working group. And that he always supported my work and scientific ideas during these three years and especially that he gave me the opportunity and the time to develop a novel method. The same thanks go to my second supervisor Marta Torres. I want to thank her for all her help and the time we spent together in Bremen and Oregon and her advices in how-to-write-a-paper. I really enjoyed working with her, especially because of her always positive attitude! Thank you so much for that.

I also want to thank the whole working group for the nice work atmosphere in Bremen and on expeditions. I want to thank especially Thomas Pape, Stefanie Buchheister, Paul Wintersteller and Christian Ferreira for their support. And in particular Susan Mau and Miriam Römer, who helped me, teached me and supported me a lot during the last year. And I want to thank my office mates Jeff and Markus for the nice conversations in-between science.

I'm indebted to Angelika Rinkel and Greta Ohling for their time and help and nice chats in the office or kitchen.

I want to thank all my friends Jenny, Max, Nicole, Timo, Chris, Sandra, Colin, Sina, Karo and Sebastian for so many nice, relaxed, funny, exciting, and also sometimes strange evenings, days, weekends, coffee breaks, mails and skype calls! You kept me balanced and made my life in the last three years so wonderful.

Und ganz herzlich möchte ich mich bei der besten Familie auf der Welt bedanken. Danke, dass ihr immer für mich da seid und meinen Lebensweg immer bedingungslos unterstützt. Danke für das viele Daumendrücken, für aufmunternde Telefonate, schöne Besuche, geschickte Bilder und ganz besonders für eure Liebe ☺. Ohne euch wäre das nicht möglich gewesen.

REFERENCES

Alperin, M. J., W. S. Reeburgh, and M. J. Whiticar (1988), Carbon and hydrogen isotope fractionation resulting from anaerobic methane oxidation, *Glob. Biochem. Cycles*, *2*, 279–288.

Archambeau, A., and C. Pierre (1998), Distributions of oxygen and carbon stable isotopes and CFC-12 in the water masses of the Southern Ocean at 30 E from South Africa to Antarctica: Results of the, *J. Mar. Syst.*, *17*(November), 25–38.

Archer, D., B. Buffett, and V. Brovkin (2009), Ocean methane hydrates as a slow tipping point in the global carbon cycle., *Proc. Natl. Acad. Sci. U. S. A.*, *106*(49), 20596–20601, doi:10.1073/pnas.0800885105.

Arévalo-Martínez, D. L., M. Beyer, M. Krumbholz, I. Piller, A. Kock, T. Steinhoff, A. Körtzinger, and H. W. Bange (2013), A new method for continuous measurements of oceanic and atmospheric N_2O, CO and CO_2: performance of off-axis integrated cavity output spectroscopy (OA-ICOS) coupled to non-dispersive infrared detection (NDIR), *Ocean Sci.*, *9*(6), 1071–1087, doi:10.5194/os-9-1071-2013.

Atkinson, A., M. Whitehouse, J. Priddle, G. Cripps, P. Ward, and M. Brandon (2001), South Georgia, Antarctica: a productive, cold water, pelagic ecosystem, *Mar. Ecol. Prog. Ser.*, *216*(JULY), 279–308, doi:10.3354/meps216279.

Badr, O., S. D. Probert, and P. W. O'Callaghan (1991), Atmospheric methane: Its contribution to global warming, *Appl. Energy*, *40*(4), 273–313, doi:10.1016/0306-2619(91)90021-O.

Baer, D. S., J. B. Paul, M. Gupta, and A. O'Keefe (2002), Sensitive absorption measurements in the near-infrared region using off-axis integrated-cavity-output spectroscopy, *Appl. Phys. B Lasers Opt.*, *75*(2-3), 261–265, doi:10.1007/s00340-002-0971-z.

Bange, H. W. (2006), Nitrous oxide and methane in European coastal waters, *Estuar. Coast. Shelf Sci.*, *70*(3), 361–374, doi:10.1016/j.ecss.2006.05.042.

Bange, H. W., U. H. Bartell, S. Rapsomanikis, and M. O. Andreae (1994), Methane in the Baltic and North Seas and a reassessment of the marine emissions of methane, *Global Biogeochem. Cycles*, *8*(4), 465–480, doi:10.1029/94GB02181.

Barber, A. J., S. Tjokrosapoetro, and T. R. Charlton (1986), Mud Volcanoes, Shale Diapirs, Wrench Faults, and Melanges in Accretionary Complexes, Eastern Indonesia, *Am. Assoc. Pet. Geol. Bull.*, *70*(11), 1729–1741.

Barry, J. P., H. G. Greene, D. L. Orange, C. H. Baxter, B. H. Robison, R. E. Kochevar, J. W. Nybakken, D. L. Reed, and C. M. McHugh (1996), Biologic and geologic characteristics of cold seeps in Monterey Bay, California, *Deep. Res. Part I Oceanogr. Res. Pap.*, *43*(11-12), 1739–1762, doi:10.1016/S0967-0637(96)00075-1.

Berman, E. S. F., M. Fladeland, J. Liem, R. Kolyer, and M. Gupta (2012), Greenhouse gas analyzer for measurements of carbon dioxide, methane, and water vapor aboard an unmanned aerial vehicle, *Sensors Actuators, B Chem.*, *169*, 128–135, doi:10.1016/j.snb.2012.04.036.

Bernard, B. B., J. M. Brooks, and W. M. Sackett (1978), Light hydrocarbons in recent Texas continental shelf and slope sediments, *J. Geophys. Res.*, *83*(C8), doi:10.1029/JC083iC08p04053.

Berndt, C. (2005), Focused fluid flow in passive continental margins., *Philos. Trans. R. Soc. A*, *363*(1837), 2855–71, doi:10.1098/rsta.2005.1666.

Berner, R. (1980), *Early diagenesis: A theoretical approach*, Princeton University Press.

Biastoch, A. et al. (2011), Rising Arctic Ocean temperatures cause gas hydrate destabilization and ocean acidification, *Geophys. Res. Lett.*, *38*(8), doi:10.1029/2011GL047222.

Björck, S., N. Malmer, C. Hjort, P. Sandgren, Ó. Ingólfsson, R. Ian, L. Smith, and B. L. Jónsson (1991), Stratigraphic and paleoclimatic studies of a 5500-year-old moss bank on Elephant Island, Antarctica, *Arct. Alp. Res.*, *24*(4), 361–374.

Boetius, A., and E. Suess (2004), Hydrate Ridge: a natural laboratory for the study of microbial life fueled by methane from near-surface gas hydrates, *Chem. Geol.*, *205*(3-4), 291–310, doi:10.1016/j.chemgeo.2003.12.034.

Boetius, A., K. Ravenschlag, C. J. Schubert, D. Rickert, F. Widdel, A. Gieseke, R. Amann, B. B. Jørgensen, U. Witte, and O. Pfannkuche (2000), A marine microbial consortium apparently mediating anaerobic oxidation of methane., *Nature*, *407*(6804), 623–626, doi:10.1038/35036572.

Bohrmann, G. (2013), *The expedition of the research vessel "Polarstern" to the Antarctic in 2013 (ANT-XXIX/4)*, Alfred Wegener Institute for Polar and Marine Research.

Bohrmann, G., and M. E. Torres (2006), Gas Hydrates in Marine Sediments, in *Marine Geochemistry*, edited by H. D. Schulz and M. Zabel, pp. 481–512, Springer-Verlag, Berlin/Heidelberg.

Bohrmann, G., J. Greinert, E. Suess, and M. Torres (1998), Authigenic carbonates from the Cascadia subduction zone and their relation to gas hydrate stability, *Geology*, *26*(7), 647–650, doi:10.1130/0091-7613(1998)026<0647:ACFTCS>2.3.CO.

Bohrmann, G. et al. (2003), Mud volcanoes and gas hydrates in the Black Sea: new data from Dvurechenskii and Odessa mud volcanoes, *Geo-Marine Lett.*, *23*(3-4), 239–249, doi:10.1007/s00367-003-0157-7.

Bohrmann, G., Alvarez, R., Biller, T., Buchheister, S., Büttner, H., Canoni, O., Dehning, K., T. Ferreira, C., Geprägs, P., Heinken, S., Hüttich, D., Johansen, C., Klar, S., Klüber, S., Leymann, D. Mai, H.A., Marcon, Y., Mary, F., Meinecke, G., Menapace, W., Nowald, N., Pape, T., Praeg, H. Raeke, A., Rehage, R., Renken, J., Reuter, C., Rohleder, C., Römer, M., Sahling, M. Sans i Coll, C., Schade, T., Seiter, C., Spalek, P., Spiesecke, U., Tamborrino, L., Torres, and M. von Wahl, T., Wiebe, M., Wintersteller, P., Zarrouk (2014), *Report and preliminary results of R/V METEOR cruise M112, Dynamic of Mud Volcanoes and Seeps in the Calabrian Accretionary Prism, Ionian Sea, Catania (Italy) – Catania (Italy), November 6 – December 15*.

Borowski, W. S., C. K. Paull, and W. I. Ussler (1996), Marine pore-water sulfate profiles indicate in situ methane flux from underlying gas hydrate, *Geology*, *24*(7), 655–658, doi:10.1130/0091-7613(1996)024.

Borowski, W. S., C. K. Paull, and W. Ussler (1997), Carbon cycling within the upper methanogenic zone of continental rise sediments; An example from the methane-rich sediments overlying the Blake Ridge gas hydrate deposits, *Mar. Chem.*, *57*(3-4), 299–311, doi:10.1016/S0304-4203(97)00019-4.

Borowski, W. S., C. K. Paull, and W. I. Ussler (1999), Global and local variations of interstitial sulfate gradients in deep-water, continental margin sediments: Sensitivity to underlying methane and gas hydrates, *Mar. Geol.*, *159*(1-4), 131–154, doi:10.1016/S0025-3227(99)00004-3.

Borrione, I., and R. Schlitzer (2013), Distribution and recurrence of phytoplankton blooms around South Georgia, Southern Ocean, *Biogeosciences*, *10*(1), 217–231, doi:10.5194/bg-10-217-2013.

Boudreau, B. P. (1997), *Diagenetic Models and Their Implementation*, Springer, Berlin, Heidelberg.

Brooks, J. M., H. B. Cox, W. R. Bryant, M. C. Kennicutt, R. G. Mann, and T. J. McDonald (1986), Association of gas hydrates and oil seepage in the Gulf of Mexico, *Org. Geochem.*, *10*(1-3), 221–234, doi:10.1016/0146-6380(86)90025-2.

Capelle, D. W., J. W. Dacey, and P. D. Tortell (2015), An automated, high through-put method for accurate and precise measurements of dissolved nitrous-oxide and methane concentrations in natural waters, *Limnol. Oceanogr. Methods*, n/a–n/a, doi:10.1002/lom3.10029.

Carlson, D. (2013), Polar science news in brief, *Environ. Earth Sci.*, 1813–1821, doi:10.1029/2012GL.

Casciotti, K. L. (2009), Inverse kinetic isotope fractionation during bacterial nitrite oxidation, *Geochim. Cosmochim. Acta*, *73*(7), 2061–2076, doi:10.1016/j.gca.2008.12.022.

Cathles, L. M., Z. Su, and D. Chen (2010), The physics of gas chimney and pockmark formation, with implications for assessment of seafloor hazards and gas sequestration, *Mar. Pet. Geol.*, *27*(1), 82–91, doi:10.1016/j.marpetgeo.2009.09.010.

Ceramicola, S., D. Praeg, A. Cova, D. Accettella, and M. Zecchin (2014), Seafloor distribution and last glacial to postglacial activity of mud volcanoes on the Calabrian accretionary prism, Ionian Sea, *Geo-Marine Lett.*, *34*(2-3), 111–129, doi:10.1007/s00367-013-0354-y.

Christensen, T. R. (2004), Thawing sub-arctic permafrost: Effects on vegetation and methane emissions, *Geophys. Res. Lett.*, *31*(4), doi:10.1029/2003GL018680.

Clark, J. F., I. Leifer, L. Washburn, and B. P. Luyendyk (2003), Compositional changes in natural gas bubble plumes: Observations from the coal oil Point marine hydrocarbon seep field, *Geo-Marine Lett.*, *23*(3-4), 187–193, doi:10.1007/s00367-003-0137-y.

Claypool, G., and K. Kvenvolden (1983), Methane and other hydrocarbon gases in marine sediment, *Annu. Rev. Earth Planet. Sci.*, *11*, 299–327.

Claypool, G., and C. Threlkeld (1983), Anoxic diagenesis and methane generation in sediments of the Blake Outer ridge, deep-sea drilling project site-533, Leg-76, *Initial reports Deep sea Drill. Proj.*, *76*, 391–402.

Crespo-Medina, M. et al. (2014), The rise and fall of methanotrophy following a deepwater oil-well blowout, *Nat. Geosci.*, *7*(6), 423–427, doi:10.1038/ngeo2156.

Cunningham, A. P., P. F. Barker, and J. S. Tomlinson (1998), Tectonics and sedimentary environment of the North Scotia Ridge region revealed by side-scan sonar, *J. Geol. Soc. London.*, *155*(6), 941–956, doi:10.1144/gsjgs.155.6.0941.

Currie, L. A. (1968), Limits for qualitative detection and quantitative determination. Application to radiochemistry, *Anal. Chem.*, *40*(3), 586–593, doi:10.1021/ac60259a007.

D'Agostino, N., A. Avallone, D. Cheloni, E. D'Anastasio, S. Mantenuto, and G. Selvaggi (2008), Active tectonics of the Adriatic region from GPS and earthquake slip vectors, *J. Geophys. Res.*, *113*(B12), B12413, doi:10.1029/2008JB005860.

Damm, E., and G. Budéus (2003), Fate of vent-derived methane in seawater above the Håkon Mosby mud volcano (Norwegian Sea), *Mar. Chem.*, *82*(1-2), 1–11, doi:10.1016/S0304-4203(03)00031-8.

Damm, E., A. Mackensen, G. Budéus, E. Faber, and C. Hanfland (2005), Pathways of methane in seawater: Plume spreading in an Arctic shelf environment (SW-Spitsbergen), *Cont. Shelf Res.*, *25*(12-13), 1453–1472, doi:10.1016/j.csr.2005.03.003.

Damm, E., E. Helmke, S. Thoms, U. Schauer, E. Nöthig, K. Bakker, and R. P. Kiene (2009), Methane production in aerobic oligotrophic surface water in the central Arctic Ocean, *Biogeosciences Discuss.*, *6*(6), 10355–10379, doi:10.5194/bgd-6-10355-2009.

Damm, E., B. Rudels, U. Schauer, S. Mau, and G. Dieckmann (2015), Methane excess in Arctic surface water- triggered by sea ice formation and melting, *Sci. Rep.*, *5*, 16179, doi:10.1038/srep16179.

Denman, K. L., and A. E. Gargett (1983), Time and space scales of vertical mixing and advection of phytoplankton in the upper ocean, *Limnol. Oceanogr.*, *28*, 801–815.

Deville, E., S.-H. Guerlais, Y. Callec, R. Griboulard, P. Huyghe, S. Lallemant, A. Mascle, M. Noble, and J. Schmitz (2006), Liquefied vs stratified sediment mobilization processes: Insight from the South of the Barbados accretionary prism, *Tectonophysics*, *428*(1-4), 33–47, doi:10.1016/j.tecto.2006.08.011.

Deville, E., S. H. Guerlais, S. Lallemant, and F. Schneider (2010), Fluid dynamics and subsurface sediment mobilization processes: an overview from Southeast Caribbean, *Basin Res.*, *22*(4), 361–379, doi:DOI 10.1111/j.1365-2117.2010.00474.x.

Devoti, R., F. Riguzzi, M. Cuffaro, and C. Doglioni (2008), New GPS constraints on the kinematics of the Apennines subduction, *Earth Planet. Sci. Lett.*, *273*(1-2), 163–174, doi:10.1016/j.epsl.2008.06.031.

Dimitrov, L. I. (2002), Mud volcanoes-the most important pathway for degassing deeply buried sediments, *Earth-Science Rev.*, *59*, 49–76, doi:10.1016/S0012-8252(02)00069-7.

Dimitrov, L. I. (2003), Mud volcanoes - A significant source of atmospheric methane, *Geo-Marine Lett.*, *23*(3-4), 155–161, doi:10.1007/s00367-003-0140-3.

Etiope, G., and G. Martinelli (2002), Migration of carrier and trace gases in the geosphere: an overview, *Phys. Earth Planet. Inter.*, *129*(3-4), 185–204, doi:10.1016/S0031-9201(01)00292-8.

Etiope, G., K. R. Lassey, R. W. Klusman, and E. Boschi (2008), Reappraisal of the fossil methane budget and related emission from geologic sources, *Geophys. Res. Lett.*, *35*(9), doi:10.1029/2008GL033623.

Faber, E., R. Botz, J. Poggenburg, M. Schmidt, P. Stoffers, and M. Hartmann (1998), Methane in Red Sea brines, *Org. Geochem.*, *29*(1–3), 363–379, doi:http://dx.doi.org/10.1016/S0146-6380(98)00155-7.

Feseker, T., J. P. Foucher, and F. Harmegnies (2008), Fluid flow or mud eruptions? Sediment temperature distributions on H??kon Mosby mud volcano, SW Barents Sea slope, *Mar. Geol.*, *247*(3-4), 194–207, doi:10.1016/j.margeo.2007.09.005.

Feseker, T., A. Dählmann, J. P. Foucher, and F. Harmegnies (2009), In-situ sediment temperature measurements and geochemical porewater data suggest highly dynamic fluid flow at Isis mud volcano, eastern Mediterranean Sea, *Mar. Geol.*, *261*(1-4), 128–137, doi:10.1016/j.margeo.2008.09.003.

Fischer, J., and M. Visbeck (1993), Deep Velocity Profiling with Self-contained ADCPs, *J. Atmos. Ocean. Technol.*, *10*(5), 764–773.

Floodgate, G. D., and A. G. Judd (1992), The origins of shallow gas, *Cont. Shelf Res.*, *12*(10), 1145–1156, doi:10.1016/0278-4343(92)90075-U.

Froelich, P. N., G. P. Klinkhammer, M. L. Bender, N. A. Luedtke, G. R. Heath, D. Cullen, P. Dauphin, D. Hammond, B. Hartman, and V. Maynard (1979), Early oxidation of organic matter in pelagic sediments of the eastern equatorial Atlantic: suboxic diagenesis, *Geochim. Cosmochim. Acta*, *43*(7), 1075–1090, doi:10.1016/0016-7037(79)90095-4.

Gentz, T., E. Damm, J. Schneider von Deimling, S. Mau, D. F. McGinnis, and M. Schlüter (2014), A water column study of methane around gas flares located at the West Spitsbergen continental margin, *Cont. Shelf Res.*, *72*, 107–118, doi:10.1016/j.csr.2013.07.013.

Graham, A. G. C., P. T. Fretwell, R. D. Larter, D. A. Hodgson, C. K. Wilson, A. J. Tate, and P. Morris (2008), A new bathymetric compilation highlighting extensive paleo-ice sheet drainage on the continental shelf, South Georgia, sub-Antarctica, *Geochemistry, Geophys. Geosystems*, *9*(7), doi:10.1029/2008GC001993.

Greinert, J., and D. F. McGinnis (2009), Single bubble dissolution model - The graphical user interface SiBu-GUI, *Environ. Model. Softw.*, *24*(8), 1012–1013, doi:10.1016/j.envsoft.2008.12.011.

Greinert, J., Y. Artemov, V. Egorov, M. Debatist, and D. McGinnis (2006), 1300-m-high rising bubbles from mud volcanoes at 2080m in the Black Sea: Hydroacoustic characteristics and temporal variability, *Earth Planet. Sci. Lett.*, *244*(1-2), 1–15, doi:10.1016/j.epsl.2006.02.011.

Guinasso, N., and D. Schink (1973), *A simple physicochemical acoustic model of methane bubbles rising in the sea*, A&M University Texas.

Gülzow, W., G. Rehder, B. Schneider, J. S. V. Deimling, and B. Sadkowiak (2011), A new method for continuous measurement of methane and carbon dioxide in surface waters using off-axis integrated cavity output spectroscopy (ICOS): An example from the Baltic Sea, *Limnol. Oceanogr. Methods*, *9*, 176–184, doi:10.4319/lom.2011.9.176.

Gülzow, W., G. Rehder, J. Schneider v. Deimling, T. Seifert, and Z. Tóth (2013), One year of continuous measurements constraining methane emissions from the Baltic Sea to the atmosphere using a ship of opportunity, *Biogeosciences*, *10*(1), 81–99, doi:10.5194/bg-10-81-2013.

Haese, R. R., C. Meile, P. Van Cappellen, and G. J. De Lange (2003), Carbon geochemistry of cold seeps: Methane fluxes and transformation in sediments from Kazan mud volcano, eastern Mediterranean Sea, *Earth Planet. Sci. Lett.*, *212*, 361–375, doi:10.1016/S0012-821X(03)00226-7.

Han, X., E. Suess, Y. Huang, N. Wu, and G. Bohrmann (2008), Jiulong methane reef: microbial mediation of seep carbonates in the South China Sea, *Mar. Geol.*

Heeschen, K. U., A. M. Tréhu, R. W. Collier, E. Suess, and G. Rehder (2003), Distribution and height of methane bubble plumes on the Cascadia Margin characterized by acoustic imaging, *Geophys. Res. Lett.*, *30*(12), doi:10.1029/2003GL016974.

Heeschen, K. U., R. S. Keir, G. Rehder, O. Klatt, and E. Suess (2004), Methane dynamics in the Weddell Sea determined via stable isotope ratios and CFC-11, *Global Biogeochem. Cycles*, *18*(2), doi:10.1029/2003GB002151.

Heintz, M. B., S. Mau, and D. L. Valentine (2012), Physical control on methanotrophic potential in waters of the Santa Monica Basin, Southern California, *Limnol. Oceanogr.*, *57*(2), 420–432, doi:10.4319/lo.2012.57.2.0420.

Hensen, C., M. Zabel, K. Pfeifer, T. Schwenk, S. Kasten, N. Riedinger, H. D. Schulz, and A. Boetius (2003), Control of sulfate pore-water profiles by sedimentary events and the significance of anaerobic oxidation of methane for the burial of sulfur in marine sediments, *Geochim. Cosmochim. Acta*, *67*(14), 2631–2647, doi:10.1016/S0016-7037(03)00199-6.

Hinrichs, K., J. M. Hayes, S. P. Sylva, P. G. Brewer, and E. F. DeLong (1999), Methane-consuming archaebacteria in marine sediments, *Nature*, *398*(6730), 802–805, doi:10.1038/19751.

Hodgson, D. A., A. G. C. Graham, H. J. Griffiths, S. J. Roberts, C. Ó. Cofaigh, M. J. Bentley, and D. J. A. Evans (2014), Glacial history of sub-Antarctic South Georgia based on the submarine geomorphology of its fjords, *Quat. Sci. Rev.*, *89*, 129–147, doi:10.1016/j.quascirev.2013.12.005.

Hoehler, T. M., M. J. Alperin, D. B. Albert, and C. S. Martens (1994), Field and laboratory studies of methane oxidation in an anoxic marine sediment: Evidence for a methanogen-sulfate reducer consortium, *Global Biogeochem. Cycles*, *8*(4), 451, doi:10.1029/94GB01800.

Holler, T., G. Wegener, H. Niemann, C. Deusner, T. G. Ferdelman, a. Boetius, B. Brunner, and F. Widdel (2011), PNAS Plus: Carbon and sulfur back flux during anaerobic microbial oxidation of methane and coupled sulfate reduction, *Proc. Natl. Acad. Sci.*, *108*(52), E1484–E1490, doi:10.1073/pnas.1106032108.

Holmes, M. E., F. J. Sansone, T. M. Rust, and B. N. Popp (2000), Methane production, consumption, and air-sea exchange in the open ocean: An Evaluation based on carbon isotopic ratios, *Global Biogeochem. Cycles*, *14*(1), 1–10, doi:10.1029/1999GB001209.

Hong, W. L., M. E. Torres, J. H. Kim, J. Choi, and J. J. Bahk (2013), Carbon cycling within the sulfate-methane-transition-zone in marine sediments from the Ulleung Basin, *Biogeochemistry*, *115*(1-3), 129–148, doi:10.1007/s10533-012-9824-y.

Hong, W.-L., M. E. Torres, J. Kim, J. Choi, and J.-J. Bahk (2014), ScienceDirect Towards quantifying the reaction network around the sulfate – methane-transition-zone in the Ulleung Basin , East Sea , with a kinetic modeling approach, *Geochim. Cosmochim. Acta*, *140*, 127–141, doi:10.1016/j.gca.2014.05.032.

Hovland, M., and H. Svensen (2006), Submarine pingoes: Indicators of shallow gas hydrates in a pockmark at Nyegga, Norwegian Sea, *Mar. Geol.*, *228*(1-4), 15–23, doi:10.1016/j.margeo.2005.12.005.

Hovland, M., A. G. Judd, and R. A. Burke (1993), The global flux of methane from shallow submarine sediments, *Chemosphere*, *26*(1-4), 559–578, doi:10.1016/0045-6535(93)90442-8.

Hovland, M., H. Svensen, C. F. Forsberg, H. Johansen, C. Fichler, J. H. Fosså, R. Jonsson, and H. Rueslåtten (2005), Complex pockmarks with carbonate-ridges off mid-Norway: Products of sediment degassing, *Mar. Geol.*, *218*(1-4), 191–206, doi:10.1016/j.margeo.2005.04.005.

Hovland, M., R. Heggland, M. H. De Vries, and T. I. Tjelta (2010), Unit-pockmarks and their potential significance for predicting fluid flow, *Mar. Pet. Geol.*, *27*(6), 1190–1199, doi:10.1016/j.marpetgeo.2010.02.005.

von Huene, R., and D. W. Scholl (1991), Observations at convergent margins concerning sediment subduction, subduction erosion, and the growth of continental crust, *Rev. Geophys.*, *29*(3), 279, doi:10.1029/91RG00969.

Hunt, J. M. (1979), *Petrolium Geochemistry and Geology*, Freeman, San Franscisco.

Hunt, J. M. (1990), Generation and Migration of Petroleum from Abnormally Pressured Fluid Compartments (1), *Am. Assoc. Pet. Geol. Bull.*, *74*(1), 1–12.

Hunt, J. M. (1991), Generation of gas and oil from coal and other terrestrial organic matter, *Org. Geochem.*, *17*(6), 673–680, doi:10.1016/0146-6380(91)90011-8.

IPCC (2007), *Climate Change 2007: The Physical Science Basis. Contribution of Working Group I to the Fourth Assessment Report of the Intergovernmental Panel on Climate Change*, edited by K. B. A. Solomon, S., D. Qin, M. Manning, Z. Chen, M. Marquis and M. T. and H. L. Miller, Cambridge University Press, Cambridge, United Kingdom and New York, NY, USA.

IPCC (2013), *Climate Change 2013: The Physical Science Basis. Contribution of Working Group I to the Fifth Assessment Report of the Intergovernmental Panel on Climate Change*, edited by V. B. and P. M. M. Stocker, T.F., D. Qin, G.-K. Plattner, M. Tignor, S.K. Allen, J. Boschung, A. Nauels, Y. Xia, Cambridge University Press, Cambridge, United Kingdom and New York, NY, USA.

Judd, A., and M. Hovland (2007), *Seabed Fluid Flow: The Impact on Geology, Biology and the Marine Environment*, Cambridge University Press, Cambridge.

Judd, A. G. (2003), The global importance and context of methane escape from the seabed, *Geo-Marine Lett.*, *23*(3-4), 147–154, doi:10.1007/s00367-003-0136-z.

Jung, W. Y., and P. R. Vogt (2004), Effects of bottom water warming and sea level rise on Holocene hydrate dissociation and mass wasting along the Norwegian-Barents Continental Margin, *J. Geophys. Res. B Solid Earth*, *109*(6), 1–18, doi:10.1029/2003JB002738.

Kara, A. B. (2003), Mixed layer depth variability over the global ocean, *J. Geophys. Res.*, *108*(C3), doi:10.1029/2000JC000736.

Keir, R. S., J. Greinert, M. Rhein, G. Petrick, J. Sültenfuß, and K. Fürhaupter (2005), Methane and methane carbon isotope ratios in the Northeast Atlantic including the Mid-Atlantic Ridge (50°N), *Deep. Res. Part I Oceanogr. Res. Pap.*, *52*(6), 1043–1070, doi:10.1016/j.dsr.2004.12.006.

Keir, R. S., O. Schmale, R. Seifert, and J. Sültenfuß (2009), Isotope fractionation and mixing in methane plumes from the Logatchev hydrothermal field, *Geochemistry, Geophys. Geosystems*, *10*(5), doi:10.1029/2009GC002403.

Kessler, J. D. et al. (2011), A persistent oxygen anomaly reveals the fate of spilled methane in the deep Gulf of Mexico., *Science*, *331*(6015), 312–5, doi:10.1126/science.1199697.

Kopf, A. (1999), Fate of sediment during plate convergence at the Mediterranean Ridge accretionary complex: Volume balance of mud extrusion versus subduction and/or accretion, *Geology*, *27*(1), 87, doi:10.1130/0091-7613(1999)027<0087:FOSDPC>2.3.CO;2.

Kopf, A., and J. H. Behrmann (2000), Extrusion dynamics of mud volcanoes on the Mediterranean Ridge accretionary complex, *Geol. Soc. London, Spec. Publ.*, *174*(1), 169–204, doi:10.1144/GSL.SP.1999.174.01.10.

Kopf, A. J. (2002), Significance of mud volcanism, *Rev. Geophys.*, *40*(May), 1005, doi:10.1029/2000RG000093.

Kopf, A. J. (2003), Global methane emission through mud volcanoes and its past and present impact on the Earth's climate, *Int. J. Earth Sci.*, *92*(5), 806–816, doi:10.1007/s00531-003-0341-z.

Korb, R. E., M. J. Whitehouse, and P. Ward (2004), SeaWiFS in the southern ocean: spatial and temporal variability in phytoplankton biomass around South Georgia, *Deep Sea Res. Part II Top. Stud. Oceanogr.*, *51*(1-3), 99, doi:10.1016/j.dsr2.2003.04.002.

Kretschmer, K., A. Biastoch, L. Rüpke, and E. Burwicz (2015), Modeling the fate of methane hydrates under global warming, *Glob. Biogeochem. Cycles*, *29*, 1–16, doi:10.1002/2014GB005011.Received.

Krooss, B. M., and D. Leythaeuser (1996), Molecular Diffusion of Light Hydrocarbons in Sedimentary Rocks and Its Role in Migration and Dissipation of Natural Gas, , 173–183.

Kutterolf, S., V. Liebetrau, T. Mörz, A. Freundt, T. Hammerich, and D. Garbe-Schönberg (2008), Lifetime and cyclicity of fluid venting at forearc mound structures determined by tephrostratigraphy and radiometric dating of authigenic carbonates, *Geology*, *36*(9), 707, doi:10.1130/G24806A.1.

Kvenvolden, K., and T. McDonald (1986), *Organic Geochemistry on the Joides Resolution - An Assay*, College Station.

Kvenvolden, K. A., and G. E. Claypool (1988), *Gas Hydrates in Oceanic Sediment*.

Lammers, S., and E. Suess (1994), An improved head-space analysis method for methane in seawater, *Mar. Chem.*, *47*(2), 115–125, doi:10.1016/0304-4203(94)90103-1.

Largier, J. L. (2003), Considerations in Estimating Larval Dispersal Distances From Oceanographic Data, *Ecol. Appl.*, *13*(sp1), 71–89, doi:10.1890/1051-0761(2003)013[0071:CIELDD]2.0.CO;2.

Lascaratos, A., W. Roether, K. Nittis, and B. Klein (1999), Recent changes in deep water formation and spreading in the eastern Mediterranean Sea: a review, *Prog. Oceanogr.*, *44*(1-3), 5–36, doi:10.1016/S0079-6611(99)00019-1.

Leifer, I., and A. Judd (2015), The UK22/4b blowout 20 years on: Investigations of continuing methane emissions from sub-seabed to the atmosphere in a North Sea context, *Mar. Pet. Geol.*, *68*, 706–717, doi:10.1016/j.marpetgeo.2015.11.012.

Leifer, I., and A. G. Judd (2002), Oceanic methane layers: the hydrocarbon seep bubble deposition hypothesis, *Terra Nov.*, *14*(6), 417–424, doi:10.1046/j.1365-3121.2002.00442.x.

Leifer, I., B. P. Luyendyk, J. Boles, and J. F. Clark (2006), Natural marine seepage blowout: Contribution to atmospheric methane, *Global Biogeochem. Cycles*, *20*(3), 1–9, doi:10.1029/2005GB002668.

Leifer, I., E. Solomon, J. Schneider von Deimling, G. Rehder, R. Coffin, and P. Linke (2015), The fate of bubbles in a large, intense bubble megaplume for stratified and unstratified water: Numerical simulations of 22/4b expedition field data, *Mar. Pet. Geol.*, *68*(February 2016), 806–823, doi:10.1016/j.marpetgeo.2015.07.025.

Li, Y., L. Zhan, J. Zhang, and L. Chen (2015), Equilibrator-based measurements of dissolved methane in the surface ocean using an integrated cavity output laser absorption spectrometer, *Acta Oceanol. Sin.*, *34*(6), 34–41, doi:10.1007/s13131-015-0685-9.

Linke, P., S. Sommer, L. Rovelli, and D. F. McGinnis (2010), Physical limitations of dissolved methane fluxes: The role of bottom-boundary layer processes, *Mar. Geol.*, *272*(1-4), 209–222, doi:10.1016/j.margeo.2009.03.020.

Luff, R., K. Wallmann, and G. Aloisi (2004), Numerical modeling of carbonate crust formation at cold vent sites: significance for fluid and methane budgets and chemosynthetic biological communities, *Earth Planet. Sci. Lett.*, *221*(1-4), 337–353, doi:10.1016/S0012-821X(04)00107-4.

MacDonald, I. R., and M. B. Peccini (2009), Distinct activity phases during the recent geologic history of a Gulf of Mexico mud volcano, *Mar. Pet. Geol.*, *26*(9), 1824–1830, doi:10.1016/j.marpetgeo.2008.12.005.

MacDonald, I. R., N. L. Guinasso, Jr., R. Sassen, J. M. Brooks, L. Lee, and K. T. Scott (1994), Gas hydrate that breaches the sea floor on the continental slope of the Gulf of Mexico, *Geology*, *22*(8), 699, doi:10.1130/0091-7613(1994)022<0699:GHTBTS>2.3.CO;2.

MacDonald, I. R., I. Leifer, R. Sassen, P. Stine, R. Mitchell, and N. Guinasso (2002), Transfer of hydrocarbons from natural seeps to the water column and atmosphere, *Geofluids*, *2*(2), 95–107, doi:10.1046/j.1468-8123.2002.00023.x.

Magen, C., L. L. Lapham, J. W. Pohlman, K. Marshall, S. Bosman, M. Casso, and J. P. Chanton (2014), A simple headspace equilibration method for measuring dissolved methane, *Limnol. Oceanogr. Methods*, *12*, 637–650, doi:10.4319/lom.2014.12.637.

Malinverno, A., and J. W. Pohlman (2011), Modeling sulfate reduction in methane hydrate-bearing continental margin sediments: Does a sulfate-methane transition require anaerobic oxidation of methane?, *Geochemistry, Geophys. Geosystems*, *12*(7), doi:10.1029/2011GC003501.

Mascle, J., F. Mary, D. Praeg, L. Brosolo, L. Camera, S. Ceramicola, and S. Dupré (2014), Distribution and geological control of mud volcanoes and other fluid/free gas seepage features in the Mediterranean Sea and nearby Gulf of Cadiz, *Geo-Marine Lett.*, *34*(2-3), 89–110, doi:10.1007/s00367-014-0356-4.

Mau, S., D. L. Valentine, J. F. Clark, J. Reed, R. Camilli, and L. Washburn (2007), Dissolved methane distributions and air-sea flux in the plume of a massive seep field, Coal Oil Point, California, *Geophys. Res. Lett.*, *34*(22), doi:10.1029/2007GL031344.

Mau, S., M. B. Heintz, and D. L. Valentine (2012), Quantification of CH4 loss and transport in dissolved plumes of the Santa Barbara Channel, California, *Cont. Shelf Res.*, *32*, 110–120, doi:10.1016/j.csr.2011.10.016.

Mau, S., J. Blees, E. Helmke, H. Niemann, and E. Damm (2013), Vertical distribution of methane oxidation and methanotrophic response to elevated methane concentrations in stratified waters of the Arctic fjord Storfjorden (Svalbard, Norway), *Biogeosciences*, *10*(10), 6267–6268, doi:10.5194/bg-10-6267-2013.

Mau, S., T. Gentz, J.-H. Körber, M. E. Torres, M. Römer, H. Sahling, P. Wintersteller, R. Martinez, M. Schlüter, and E. Helmke (2015), Seasonal methane accumulation and release from a gas emission site in the central North Sea, *Biogeosciences*, *12*(18), 5261–5276, doi:10.5194/bg-12-5261-2015.

McGinnis, D. F., J. Greinert, Y. Artemov, S. E. Beaubien, and A. Wüest (2006), Fate of rising methane bubbles in stratified waters: How much methane reaches the atmosphere?, *J. Geophys. Res.*, *111*(C9), doi:10.1029/2005JC003183.

Meisel, O., A. Graham, and G. Kuhn (2014), A new record of post-glacial sedimentation in a glacial trough, offshore sub-Antarctic South Georgia, *EGU Gen. Assem. 2014*.

Meredith, M. P. (2003a), An anticyclonic circulation above the Northwest Georgia Rise, Southern Ocean, *Geophys. Res. Lett.*, *30*(20), doi:10.1029/2003GL018039.

Meredith, M. P. (2003b), Southern ACC Front to the northeast of South Georgia: Pathways, characteristics, and fluxes, *J. Geophys. Res.*, *108*(C5), doi:10.1029/2001JC001227.

Mienert, J., M. Vanneste, S. Bünz, K. Andreassen, H. Haflidason, and H. P. Sejrup (2005), Ocean warming and gas hydrate stability on the mid-Norwegian margin at the Storegga Slide, *Mar. Pet. Geol.*, *22*(1-2), 233–244, doi:10.1016/j.marpetgeo.2004.10.018.

Milkov, A. V. (2000), Worldwide distribution of submarine mud volcanoes and associated gas hydrates, *Mar. Geol.*, *167*(1-2), 29–42, doi:10.1016/S0025-3227(00)00022-0.

Milkov, A. V. (2003), Global gas flux from mud volcanoes: A significant source of fossil methane in the atmosphere and the ocean, *Geophys. Res. Lett.*, *30*(2), 1037, doi:10.1029/2002GL016358.

Mottl, M. J., C. G. Wheat, P. Fryer, J. Gharib, and J. B. Martin (2004), Chemistry of springs across the Mariana forearc shows progressive devolatilization of the subducting plate, *Geochim. Cosmochim. Acta*, *68*(23), 4915–4933, doi:10.1016/j.gca.2004.05.037.

Murphy, E. J., J. L. Watkins, M. P. Meredith, P. Ward, P. N. Trathan, and S. E. Thorpe (2004), Southern Antarctic Circumpolar Current Front to the northeast of South Georgia: horizontal advection of krill and its role in the ecosystem, , *109*, 1–10, doi:10.1029/2002JC001522.

Murphy, E. J. et al. (2013), Comparison of the structure and function of Southern Ocean regional ecosystems: The Antarctic Peninsula and South Georgia, *J. Mar. Syst.*, *109-110*, 22–42, doi:10.1016/j.jmarsys.2012.03.011.

Naehr, T. H., P. Eichhubl, V. J. Orphan, M. Hovland, C. K. Paull, W. Ussler, T. D. Lorenson, and H. G. Greene (2007), Authigenic carbonate formation at hydrocarbon seeps in continental margin sediments: A comparative study, *Deep Sea Res. Part II Top. Stud. Oceanogr.*, *54*(11-13), 1268–1291, doi:10.1016/j.dsr2.2007.04.010.

Niewöhner, C., C. Hensen, S. Kasten, M. Zabel, and H. . Schulz (1998), Deep Sulfate Reduction Completely Mediated by Anaerobic Methane Oxidation in Sediments of the Upwelling Area off Namibia, *Geochim. Cosmochim. Acta*, *62*(3), 455–464, doi:10.1016/S0016-7037(98)00055-6.

Nöthen, K., and S. Kasten (2011), Reconstructing changes in seep activity by means of pore water and solid phase Sr/Ca and Mg/Ca ratios in pockmark sediments of the Northern Congo Fan, *Mar. Geol.*, *287*(1-4), 1–13, doi:10.1016/j.margeo.2011.06.008.

Nunn, J. A., and P. Meulbroek (2002), Kilometer-scale upward migration of hydrocarbons in geopressured sediments by buoyancy-driven propagation of methane-filled fractures, *Am. Assoc. Pet. Geol. Bull.*, *86*(5), 907–918.

Orsi, A. H., T. Whitworth, and W. D. Nowlin (1995), On the meridional extent and fronts of the Antarctic Circumpolar Current, *Deep Sea Res. Part I Oceanogr. Res. Pap.*, *42*(5), 641–673, doi:10.1016/0967-0637(95)00021-W.

Palmer, M. R., T. P. Rippeth, and J. H. Simpson (2008), An investigation of internal mixing in a seasonally stratified shelf sea, *J. Geophys. Res.*, *113*(C12), doi:10.1029/2007JC004531.

Panieri, G., A. Polonia, R. G. Lucchi, S. Zironi, L. Capotondi, A. Negri, and L. Torelli (2013), Mud volcanoes along the inner deformation front of the Calabrian Arc accretionary wedge (Ionian Sea), *Mar. Geol.*, *336*, 84–98, doi:10.1016/j.margeo.2012.11.003.

Pape, T., S. Kasten, M. Zabel, A. Bahr, F. Abegg, H.-J. J. Hohnberg, and G. Bohrmann (2010a), Gas hydrates in shallow deposits of the Amsterdam mud volcano, Anaximander Mountains, Northeastern Mediterranean Sea, *Geo-Marine Lett.*, *30*(3-4), 187–206, doi:10.1007/s00367-010-0197-8.

Pape, T., A. Bahr, J. Rethemeyer, J. D. Kessler, H. Sahling, K. U. Hinrichs, S. a. Klapp, W. S. Reeburgh, and G. Bohrmann (2010b), Molecular and isotopic partitioning of low-molecular-weight hydrocarbons during migration and gas hydrate precipitation in deposits of a high-flux seepage site, *Chem. Geol.*, *269*(3-4), 350–363, doi:10.1016/j.chemgeo.2009.10.009.

Pape, T., A. Bahr, S. A. Klapp, F. Abegg, and G. Bohrmann (2011), High-intensity gas seepage causes rafting of shallow gas hydrates in the southeastern Black Sea, *Earth Planet. Sci. Lett.*, *307*(1-2), 35–46, doi:10.1016/j.epsl.2011.04.030.

Pape, T., P. Geprägs, S. Hammerschmidt, P. Wintersteller, J. Wei, T. Fleischmann, G. Bohrmann, and A. J. Kopf (2014), Hydrocarbon seepage and its sources at mud volcanoes of the Kumano forearc basin, Nankai Trough subduction zone, *Geochemistry, Geophys. Geosystems*, *15*(6), doi:10.1002/2013GC005057.

Paull, C. K., W. I. Ussler, W. S. Borowski, and F. N. Spiess (1995), Methane-rich plumes on the Carolina continental rise: Associations with gas hydrates, *Geology*, *23*(1), 89–92, doi:10.1130/0091-7613(1995)023.

Paull, C. K., T. D. Lorenson, W. S. Borowski, W. I. Ussler, K. Olsen, and N. M. Rodriguez (2000), Isotopic composition of CH4, CO2 species, and sedimentary organic matter within samples from the Blake Ridge: gas source implications, in *Proceedings of the Ocean Drilling Program, 164 Scientific Results*, vol. 164, pp. 67–78, Ocean Drilling Program.

Paull, C. K., W. R. Normark, W. Ussler, D. W. Caress, and R. Keaten (2008), Association among active seafloor deformation, mound formation, and gas hydrate growth and accumulation within the seafloor of the Santa Monica Basin, offshore California, *Mar. Geol.*, *250*(3-4), 258–275, doi:10.1016/j.margeo.2008.01.011.

Pinardi, N., and E. Masetti (2000), Variability of the large scale general circulation of the Mediterranean Sea from observations and modelling: A review, *Palaeogeogr. Palaeoclimatol. Palaeoecol.*, *158*, 153–174, doi:10.1016/S0031-0182(00)00048-1.

Platt, H. M. (1979), Sedimentation and the distribution of organic matter in a sub-Antarctic marine bay, *Estuar. Coast. Mar. Sci.*, *9*(1), 51–63, doi:10.1016/0302-3524(79)90006-9.

Pohlman, J. W., C. Ruppel, D. R. Hutchinson, R. Downer, and R. B. Coffin (2008), Assessing sulfate reduction and methane cycling in a high salinity pore water system in the northern Gulf of Mexico, *Mar. Pet. Geol.*, *25*(9), 942–951, doi:10.1016/j.marpetgeo.2008.01.016.

Pohlman, J. W., M. Riedel, J. E. Bauer, E. A. Canuel, C. K. Paull, L. Lapham, K. S. Grabowski, R. B. Coffin, and G. D. Spence (2013), Anaerobic methane oxidation in low-organic content methane seep sediments, *Geochim. Cosmochim. Acta*, *108*, 184–201, doi:10.1016/j.gca.2013.01.022.

Polonia, A., L. Torelli, P. Mussoni, L. Gasperini, A. Artoni, and D. Klaeschen (2011), The Calabrian Arc subduction complex in the Ionian Sea: Regional architecture, active deformation, and seismic hazard, *Tectonics*, *30*(5), 1–28, doi:10.1029/2010TC002821.

Popp, B. N., F. J. Sansone, T. M. Rust, and D. a Merrittt (1995), Determination of Concentration and Carbon Isotopic Composition of Dissolved Methane in Sediments and Nearshore Waters, *Anal. Chem.*, *67*(2), 405–411, doi:10.1021/ac00098a028.

Praeg, D., S. Ceramicola, and R. Barbieri (2009), Tectonically-driven mud volcanism since the late Pliocene on the Calabrian accretionary prism, central Mediterranean Sea, *Mar. Pet. …*.

Prinzhofer, A. A., and A. Y. Huc (1995), Genetic and post-genetic molecular and isotopic fractionations in natural gases, *Chem. Geol.*, *126*(3-4), 281–290, doi:10.1016/0009-2541(95)00123-9.

Proskurowski, G., M. D. Lilley, J. S. Seewald, G. L. Früh-Green, E. J. Olson, J. E. Lupton, S. P. Sylva, and D. S. Kelley (2008), Abiogenic hydrocarbon production at lost city hydrothermal field., *Science*, *319*(5863), 604–7, doi:10.1126/science.1151194.

Van Der Putten, N., and C. Verbruggen (2005), The onset of deglaciation of Cumberland Bay and Stromness Bay, South Georgia, *Antarct. Sci.*, *17*(1), 29–32, doi:10.1017/S0954102005002397.

Ranero, C. R., I. Grevemeyer, H. Sahling, U. Barckhausen, C. Hensen, K. Wallmann, W. Weinrebe, P. Vannucchi, R. von Huene, and K. McIntosh (2008), Hydrogeological system of erosional convergent margins and its influence on tectonics and interplate seismogenesis, *Geochemistry, Geophys. Geosystems*, *9*(3), doi:10.1029/2007GC001679.

Reeburgh, W. (2007), Oceanic methane biogeochemistry, *Chem. Rev.*, *107*, 486–513, doi:10.1021/cr050362v.

Reeburgh, W. S. (1976), Methane consumption in Cariaco Trench waters and sediments, *Earth Planet. Sci. Lett.*, *28*(3), 337–344, doi:10.1016/0012-821X(76)90195-3.

Reeburgh, W. S., B. B. Ward, S. C. Whalen, K. A. Sandbeck, K. A. Kilpatrickt, and L. J. Kerkhof (1991), Black Sea methane geochemistry, *Deep Sea Res. Part A. Oceanogr. Res. Pap.*, *38*, S1189–S1210, doi:10.1016/S0198-0149(10)80030-5.

Rehder, G., R. S. Keir, E. Suess, and M. Rhein (1999), Methane in the northern Atlantic controlled by microbial oxidation and atmospheric history, *Geophys. Res. Lett.*, *26*(5), doi:10.1029/1999GL900049.

Rehder, G., P. W. Brewer, E. T. Peltzer, and G. Friederich (2002), Enhanced lifetime of methane bubble streams within the deep ocean, *Geophys. Res. Lett.*, *29*(15), doi:10.1029/2001GL013966.

Rehder, G., I. Leifer, P. G. Brewer, G. Friederich, and E. T. Peltzer (2009), Controls on methane bubble dissolution inside and outside the hydrate stability field from open ocean field experiments and numerical modeling, *Mar. Chem.*, *114*(1-2), 19–30, doi:10.1016/j.marchem.2009.03.004.

Rella, C. W. et al. (2013), High accuracy measurements of dry mole fractions of carbon dioxide and methane in humid air, *Atmos. Meas. Tech.*, *6*(3), 837–860, doi:10.5194/amt-6-837-2013.

Van Rensbergen, P., R. R. Hillis, A. J. Maltman, and C. K. Morley (2003), Subsurface sediment mobilization: introduction, *Geol. Soc. London, Spec. Publ.*, *216*(1), 1–8, doi:10.1144/GSL.SP.2003.216.01.01.

Rice, D. D., and G. E. Claypool (1981), Generation, Accumulation, and Resource Potential of Biogenic Gas, *Am. Assoc. Pet. Geol. Bull.*, *65*(1), 5–25.

Roberts, H. H., B. A. Hardage, W. W. Shedd, and J. Hunt (2006), Seafloor reflectivity—An important seismic property for interpreting fluid/gas expulsion geology and the presence of gas hydrate, *Lead. Edge*, *25*(5), 620–628, doi:10.1190/1.2202667.

Roberts, P. J. W., and D. R. Webster (2002), Turbulent diffusion, in *Environmental Fluid Mechanics: Theories and Applications*, edited by H. Shen, A. Cheng, K.-H. Wang, M. H. Teng, and C. Liu, Amer. Soc. Civil Eng. Press, Reston, Virginia.

Römer, M., H. Sahling, T. Pape, G. Bohrmann, and V. Spieß (2012), Quantification of gas bubble emissions from submarine hydrocarbon seeps at the Makran continental margin (offshore Pakistan), *J. Geophys. Res. Ocean.*, *117*(10), doi:10.1029/2011JC007424.

Römer, M. et al. (2014a), First evidence of widespread active methane seepage in the Southern Ocean, off the sub-Antarctic island of South Georgia, *Earth Planet. Sci. Lett.*, *403*, 166–177, doi:10.1016/j.epsl.2014.06.036.

Römer, M., H. Sahling, T. Pape, C. dos Santos Ferreira, F. Wenzhöfer, A. Boetius, and G. Bohrmann (2014b), Methane fluxes and carbonate deposits at a cold seep area of the Central Nile Deep Sea Fan, Eastern Mediterranean Sea, *Mar. Geol.*, *347*, 27–42, doi:10.1016/j.margeo.2013.10.011.

Rossi, S., and R. Sartori (1981), A seismic reflection study of the external Calabrian Arc in the Northern Ionian Sea (Eastern Mediterranean), *Mar. Geophys. Res.*, *4*(4), 403–426, doi:10.1007/BF00286036.

Sahling, H., D. Rickert, R. Lee, P. Linke, and E. Suess (2002), Macrofaunal community structure and sulfide flux at gas hydrate deposits from the Cascadia convergent margin, NE Pacific, *Mar. Ecol. Prog. Ser.*, *231*, 121–138, doi:10.3354/meps231121.

Sahling, H., S. V Galkin, A. Salyuk, J. Greinert, H. Foerstel, D. Piepenburg, and E. Suess (2003), Depth-related structure and ecological significance of cold-seep communities—a case study from the Sea of Okhotsk, *Deep Sea Res. Part I Oceanogr. Res. Pap.*, *50*(12), 1391–1409, doi:10.1016/j.dsr.2003.08.004.

Sahling, H., G. Bohrmann, V. Spiess, J. Bialas, M. Breitzke, M. Ivanov, S. Kasten, S. Krastel, and R. Schneider (2008), Pockmarks in the Northern Congo Fan area, SW Africa: Complex seafloor features shaped by fluid flow, *Mar. Geol.*, *249*(3-4), 206–225, doi:10.1016/j.margeo.2007.11.010.

Sansone, F. J., and C. S. Martens (1978), Methane oxidation in Cape Lookout Bight, North Carolina, *Limnol. Oceanogr.*, *23*(2), 349–355, doi:10.4319/lo.1978.23.2.0349.

Sansone, F. J., B. N. Popp, and T. M. Rust (1997), Stable Carbon Isotopic Analysis of Low-Level Methane in Water and Gas, *Anal. Chem.*, *69*(1), 40–44, doi:10.1021/ac960241i.

Sartori, R. (2003), The Tyrrhenian back-arc basin and subduction of the Ionian lithosphere, *Episodes*, *26*(3), 217–221.

Sauter, E. J., S. I. Muyakshin, J.-L. Charlou, M. Schlüter, A. Boetius, K. Jerosch, E. Damm, J.-P. Foucher, and M. Klages (2006), Methane discharge from a deep-sea submarine mud volcano into the upper water column by gas hydrate-coated methane bubbles, *Earth Planet. Sci. Lett.*, *243*(3-4), 354–365, doi:10.1016/j.epsl.2006.01.041.

Schlitzer, R. (2002), Carbon export fluxes in the Southern Ocean: Results from inverse modeling and comparison with satellite-based estimates, *Deep. Res. Part II Top. Stud. Oceanogr.*, *49*(9-10), 1623–1644, doi:10.1016/S0967-0645(02)00004-8.

Schlitzer, R., W. Roether, H. Oster, H. G. Junghans, M. Hausmann, H. Johannsen, and A. Michelato (1991), Chlorofluoromethane and oxygen in the Eastern Mediterranean, *Deep Sea Res. Part A, Oceanogr. Res. Pap.*, *38*(12), 1531–1551, doi:10.1016/0198-0149(91)90088-W.

Schmale, O., J. Greinert, and G. Rehder (2005), Methane emission from high-intensity marine gas seeps in the Black Sea into the atmosphere, *Geophys. Res. Lett.*, *32*(7), doi:10.1029/2004GL021138.

Schmale, O., J. Schneider von Deimling, W. Gülzow, G. Nausch, J. J. Waniek, and G. Rehder (2010), Distribution of methane in the water column of the Baltic Sea, *Geophys. Res. Lett.*, *37*(12), doi:10.1029/2010GL043115.

Schneider von Deimling, J., P. Linke, M. Schmidt, and G. Rehder (2015), Ongoing methane discharge at well site 22/4b (North Sea) and discovery of a spiral vortex bubble plume motion, *Mar. Pet. Geol.*, *68*, 718–730, doi:10.1016/j.marpetgeo.2015.07.026.

Scholl, D. W., and R. von Huene (2007), *4-D Framework of Continental Crust*, Geological Society of America Memoirs, Geological Society of America.

Schulz, H. D. (2000), Quantification of early diagenesis: Dissolved constituents in marine pore water, in *Marine Geochemistry*, edited by H. D. Schulz and M. Zabel, pp. 85–128, Springer-Verlag, Berlin.

Schuur, E., and J. Bockheim (2008), Vulnerability of permafrost carbon to climate change: Implications for the global carbon cycle, *Bioscience*, *58*(September), 701–714, doi:10.1641/B580807.

Seeberg-Elverfeldt, J., M. Schlüter, T. Feseker, and M. Kölling (2005), Rhizon sampling of pore waters near the sediment/water interface of aquatic systems, *Limnol. Oceanogr. Methods*, *3*, 361–371, doi:10.4319/lom.2005.3.361.

Sellschopp, J., and A. Alvarez (2003), Dense low-salinity outflow from the Adriatic Sea under mild (2001) and strong (1999) winter conditions, *J. Geophys. Res.*, *108*(C9), 1–12, doi:10.1029/2002JC001562.

Sivan, O., D. P. Schrag, and R. W. Murray (2007), Rates of methanogenesis and methanotrophy in deep-sea sediments, *Geobiology*, *5*(2), 141–151, doi:10.1111/j.1472-4669.2007.00098.x.

Sloan, E. D. (2003), Fundamental principles and applications of natural gas hydrates., *Nature*, *426*(6964), 353–63, doi:10.1038/nature02135.

Smith, R. I. L. (1981), Types of peat and peat-forming vegetation on South Georgia., *Br. Antarct. Surv. Bull.*, (53), 119–139.

Snyder, G. T., A. Hiruta, R. Matsumoto, G. R. Dickens, H. Tomaru, R. Takeuchi, J. Komatsubara, Y. Ishida, and H. Yu (2007), Pore water profiles and authigenic mineralization in shallow marine sediments above the methane-charged system on Umitaka Spur, Japan Sea, *Deep. Res. Part II Top. Stud. Oceanogr.*, *54*(11-13), 1216–1239, doi:10.1016/j.dsr2.2007.04.001.

Solomon, E. A., M. Kastner, I. R. MacDonald, and I. Leifer (2009), Considerable methane fluxes to the atmosphere from hydrocarbon seeps in the Gulf of Mexico, *Nat. Geosci.*, *2*(8), 561–565, doi:10.1038/ngeo574.

Sommer, S., O. Pfannkuche, P. Linke, R. Luff, J. Greinert, M. Drews, S. Gubsch, M. Pieper, M. Poser, and T. Viergutz (2006), Efficiency of the benthic filter: Biological control of the emission of dissolved methane from sediments containing shallow gas hydrates at Hydrate Ridge, *Global Biogeochem. Cycles*, *20*(2), doi:10.1029/2004GB002389.

Steinle, L. et al. (2015), Water column methanotrophy controlled by a rapid oceanographic switch, *Nat. Geosci.*, *8*(5), 378–382, doi:10.1038/ngeo2420.

Suess, E. (1980), Particulate organic carbon flux in the oceans—surface productivity and oxygen utilization, *Nature*, *288*(5788), 260–263, doi:10.1038/288260a0.

Suess, E. (2014), Marine cold seeps and their manifestations: geological control, biogeochemical criteria and environmental conditions, *Int. J. Earth Sci.*, 1889–1916, doi:10.1007/s00531-014-1010-0.

Sundermeyer, M. A., and J. F. Price (1998), Lateral mixing and the North Atlantic Tracer Release Experiment: Observations and numerical simulations of Lagrangian particles and a passive tracer, *J. Geophys. Res. Ocean.*, *103*(C10), 21481–21497, doi:10.1029/98JC01999.

Talukder, A. R. (2012), Review of submarine cold seep plumbing systems: Leakage to seepage and venting, *Terra Nov.*, *24*, 255–272, doi:10.1111/j.1365-3121.2012.01066.x.

Teichert, B. M. A., G. Bohrmann, and E. Suess (2005), Chemoherms on Hydrate Ridge — Unique microbially-mediated carbonate build-ups growing into the water column, *Palaeogeogr. Palaeoclimatol. Palaeoecol.*, *227*(1-3), 67–85, doi:10.1016/j.palaeo.2005.04.029.

Tissot, B. P., and D. H. Welte (2013), *Petroleum Formation and Occurrence*, Springer Berlin Heidelberg.

Torres, M. E., and M. Kastner (2009), Data report : clues about carbon cycling in methane-bearing sediments using stable isotopes of the dissolved inorganic carbon , IODP Expedition 311 1, *Proc. Integr. Ocean Drill. Program, Vol. 311*, *311*, 1–8, doi:10.2204/iodp.proc.311.206.2009.

Torres, M. E., J. McManus, D. E. Hammond, M. A. de Angelis, K. U. Heeschen, S. L. Colbert, M. D. Tryon, K. M. Brown, and E. Suess (2002), Fluid and chemical fluxes in and out of sediments hosting methane hydrate deposits on Hydrate Ridge, OR, I: Hydrological provinces, *Earth Planet. Sci. Lett.*, *201*(3-4), 525–540, doi:10.1016/S0012-821X(02)00733-1.

Torres, M. E., A. C. Mix, and W. D. Rugh (2005), Precise δ13C analysis of dissolved inorganic carbon in natural waters using automated headspace sampling and continuous-flow mass spectrometry., *Limnol. Oceanogr. Methods*, *3*, 349–360, doi:10.4319/lom.2005.3.349.

Traganza, E. D., J. W. Swinnerton, and C. H. Cheek (1979), Methane supersaturation and ATP-zooplankton blooms in near-surface waters of the Western Mediterranean and the subtropical North Atlantic Ocean, *Deep Sea Res. Part A. Oceanogr. Res. Pap.*, *26*(11), 1237–1245, doi:10.1016/0198-0149(79)90066-9.

Tréhu, A. M., P. B. Flemings, N. L. Bangs, J. Chevallier, E. Gràcia, J. E. Johnson, C.-S. Liu, X. Liu, M. Riedel, and M. E. Torres (2004), Feeding methane vents and gas hydrate deposits at south Hydrate Ridge, *Geophys. Res. Lett.*, *31*(23), n/a–n/a, doi:10.1029/2004GL021286.

Treude, T., S. Krause, J. Maltby, A. W. Dale, R. Coffin, and L. J. Hamdan (2014), Sulfate reduction and methane oxidation activity below the sulfate-methane transition zone in Alaskan Beaufort Sea continental margin sediments: Implications for deep sulfur cycling, *Geochim. Cosmochim. Acta*, *144*, 217–237, doi:10.1016/j.gca.2014.08.018.

Tsurushima, N., S. Watanabe, and S. Tsunogai (1996), Methane in the East China Sea water, *J. Oceanogr.*, *52*(2), 221–233, doi:10.1007/BF02235671.

Valentine, D. L. (2002), Thermodynamic Ecology of Hydrogen-Based Syntrophy, in *Symbiosis - Mechanism and Model Systems*, vol. 4, edited by J. Seckbach, pp. 147–161, Springer Netherlands, Dordrecht.

Valentine, D. L. (2011), Emerging topics in marine methane biogeochemistry., *Ann. Rev. Mar. Sci.*, *3*, 147–171, doi:10.1146/annurev-marine-120709-142734.

Valentine, D. L., and W. S. Reeburgh (2000), New perspectives on anaerobic methane oxidation, *Env. Microbiol*, *2*(5), 477–484.

Valentine, D. L., D. C. Blanton, W. S. Reeburgh, and M. Kastner (2001), Water column methane oxidation adjacent to an area of active hydrate dissociation, Eel River Basin, *Geochim. Cosmochim. Acta*, *65*(16), 2633–2640, doi:10.1016/S0016-7037(01)00625-1.

Vanneste, H., B. A. Kelly-Gerreyn, D. P. Connelly, R. H. James, M. Haeckel, R. E. Fisher, K. Heeschen, and R. A. Mills (2011), Spatial variation in fluid flow and geochemical fluxes across the sediment–seawater interface at the Carlos Ribeiro mud volcano (Gulf of Cadiz), *Geochim. Cosmochim. Acta*, *75*(4), 1124–1144, doi:10.1016/j.gca.2010.11.017.

Visbeck, M. (1995), Sea Surface Conditions remotely sensed by Upward-Looking ADCPs, *J. Atmos. Ocean. Technol.*, *1*(2), 141–149.

de Visscher, A., I. de Pourcq, and J. Chanton (2004), Isotope fractionation effects by diffusion and methane oxidation in landfill cover soils, *J. Geophys. Res. Atmos.*, *109*, 1–8, doi:10.1029/2004JD004857.

Wadham, J. L. et al. (2012), Potential methane reservoirs beneath Antarctica, *Nature*, *488*(7413), 633–637, doi:10.1038/nature11374.

Wallmann, K., M. Drews, G. Aloisi, and G. Bohrmann (2006), Methane discharge into the Black Sea and the global ocean via fluid flow through submarine mud volcanoes, *Earth Planet. Sci. Lett.*, *248*(1-2), 544–559, doi:10.1016/j.epsl.2006.06.026.

Walter, K. M., S. A. Zimov, J. P. Chanton, D. Verbyla, and F. S. Chapin (2006), Methane bubbling from Siberian thaw lakes as a positive feedback to climate warming, *Nature*, *443*(7107), 71–75, doi:10.1038/nature05040.

Wanninkhof, R., W. E. Asher, D. T. Ho, C. Sweeney, and W. R. McGillis (2009), Advances in Quantifying Air-Sea Gas Exchange and Environmental Forcing*, *Ann. Rev. Mar. Sci.*, *1*(1), 213–244, doi:10.1146/annurev.marine.010908.163742.

Ward, P. et al. (2002), The Southern Antarctic Circumpolar Current Front: Physical and biological coupling at South Georgia, *Deep. Res. Part I Oceanogr. Res. Pap.*, *49*(12), 2183–2202, doi:10.1016/S0967-0637(02)00119-X.

Welp, L. R., R. F. Keeling, R. F. Weiss, W. Paplawsky, and S. Heckman (2013), Design and performance of a Nafion dryer for continuous operation at CO2and CH4 air monitoring sites, *Atmos. Meas. Tech.*, *6*(5), 1217–1226, doi:10.5194/amt-6-1217-2013.

Westbrook, G. K. et al. (2009), Escape of methane gas from the seabed along the West Spitsbergen continental margin, *Geophys. Res. Lett.*, *36*(15), doi:10.1029/2009GL039191.

Whitehouse, M. J., J. Priddle, and C. Symon (1996), Seasonal and annual change in seawater temperature, salinity, nutrient and chlorophyll a distributions around South Georgia, South Atlantic, *Deep. Res. Part I Oceanogr. Res. Pap.*, *43*(4), 425–443, doi:10.1016/0967-0637(96)00020-9.

Whiticar, M. J. (1999), Carbon and hydrogen isotope systematics of bacterial formation and oxidation of methane, *Chem. Geol.*, *161*(1-3), 291–314, doi:10.1016/S0009-2541(99)00092-3.

Wiesenburg, D. A., and N. L. Guinasso (1979), Equilibrium solubilities of methane, carbon monoxide, and hydrogen in water and sea water, *J. Chem. Eng. Data*, *24*(4), 356–360, doi:10.1021/je60083a006.

Wunsch, C., and R. Ferrari (2004), Vertical Mixing, Energy, and the General Circulation of the Oceans, *Annu. Rev. Fluid Mech.*, *36*(1), 281–314, doi:10.1146/annurev.fluid.36.050802.122121.

Yamamoto, S., J. B. Alcauskas, and T. E. Crozier (1976), Solubility of methane in distilled water and sea water, *J. Chem. Eng. Data*, *21*(1), 78–80, doi:10.1021/je60068a029.

Yoshida, O., H. Y. Inoue, S. Watanabe, K. Suzuki, and S. Noriki (2011), Dissolved methane distribution in the South Pacific and the Southern Ocean in austral summer, *J. Geophys. Res. Ocean.*, *116*(7), 1–9, doi:10.1029/2009JC006089.

Yoshinaga, M. Y., T. Holler, T. Goldhammer, G. Wegener, J. W. Pohlman, B. Brunner, M. M. M. Kuypers, K. Hinrichs, and M. Elvert (2014), Carbon isotope equilibration during sulphate-limited anaerobic oxidation of methane, *Nat. Geosci.*, *7*(3), 190–194, doi:10.1038/ngeo2069.

Zhang, T., and B. M. Krooss (2001), Experimental investigation on the carbon isotope fractionation of methane during gas migration by diffusion through sedimentary rocks at elevated temperature and pressure, *Geochim. Cosmochim. Acta*, *65*(16), 2723–2741, doi:10.1016/S0016-7037(01)00601-9.

DECLARATION/ERKLÄRUNG

Name : Patrizia Geprägs

Anschrift : Besselstr. 73

28203 Bremen - Deutschland

Hiermit versichere ich, dass ich

1. die Arbeit ohne unerlaubte fremde Hilfe angefertigt habe,

2. keine anderen als die von mir angegebenen Quellen und Hilfsmittel benutzt habe und

3. die den benutzten Werken wörtlich oder inhaltlich entnommenen Stellen als solche kenntlich gemacht habe.

Bremen, den 29. Februar 2016

……

Patrizia Geprägs

APPENDIX

APPENDIX CHAPTER 3: CASE STUDY 1: SEEPAGE IN ANTARTICA

"Carbon cycling fed by methane seepage at the shallow Cumberland Bay, South Georgia, Subantarctic"

- Table S1
- Table S2

Table S1. Methane, sulfate and DIC concentrations in pore water. PART I-A

Station	Depth [cm]	Sulfate [mM]	Depth [cm]	CH_4 [mM]	Depth [cm]	DIC [mM]
PS81/258-1	1	25.79	75	0.003	45	8.67
PS81/258-1	25	23.93	175	0.004	125	18.57
PS81/258-1	45	22.54	275	0.003	205	22.14
PS81/258-1	65	20.33	375	0.003	285	22.04
PS81/258-1	85	18.31	475	0.003	405	25.14
PS81/258-1	105	16.60	575	0.003	525	29.39
PS81/258-1	125	15.24	675	0.004	685	27.01
PS81/258-1	145	14.40				
PS81/258-1	165	14.45				
PS81/258-1	185	14.64				
PS81/258-1	205	14.60				
PS81/258-1	225	14.33				
PS81/258-1	245	13.85				
PS81/258-1	265	13.35				
PS81/258-1	285	12.67				
PS81/258-1	305	12.41				
PS81/258-1	325	12.03				
PS81/258-1	345	11.51				
PS81/258-1	365	11.09				
PS81/258-1	385	10.69				
PS81/258-1	405	10.20				
PS81/258-1	425	9.58				
PS81/258-1	445	9.22				

Table S1. Methane, sulfate and DIC concentrations in pore water. PART I-B

Station	Depth [cm]	Sulfate [mM]
PS81/258-1	465	8.83
PS81/258-1	485	8.35
PS81/258-1	505	7.97
PS81/258-1	525	7.64
PS81/258-1	545	7.24
PS81/258-1	565	6.96
PS81/258-1	585	6.74
PS81/258-1	605	6.26
PS81/258-1	625	6.29
PS81/258-1	645	6.15
PS81/258-1	665	6.08

Table S1. Methane, sulfate and DIC concentrations in pore water. PART II-A

Station	Depth [cm]	Sulfate [mM]	Depth [m]	CH_4 [mM]	Depth [cm]	DIC [mM]
PS81/280-1	7	26.94	9	0.001	63	5.55
PS81/280-1	23	25.83	109	0.004	143	9.93
PS81/280-1	43	24.80	209	0.005	243	12.71
PS81/280-1	63	23.83	309	0.012	363	22.25
PS81/280-1	83	22.87	409	0.024	423	25.49
PS81/280-1	103	21.98	509	0.395	483	28.92
PS81/280-1	123	21.11	609	3.589	538	29.61
PS81/280-1	143	20.17	709	5.795	718	33.00
PS81/280-1	163	19.01	809	10.752	838	40.38
PS81/280-1	183	18.36				
PS81/280-1	203	17.22				
PS81/280-1	223	16.17				
PS81/280-1	243	15.23				
PS81/280-1	263	13.38				
PS81/280-1	283	11.95				
PS81/280-1	303	10.90				
PS81/280-1	323	9.88				
PS81/280-1	343	9.28				
PS81/280-1	363	7.90				
PS81/280-1	383	7.23				
PS81/280-1	403	5.90				
PS81/280-1	423	5.44				
PS81/280-1	443	3.41				
PS81/280-1	463	2.83				
PS81/280-1	483	1.95				

Table S1. Methane, sulfate and DIC concentrations in pore water. PART II-B

Station	Depth [cm]	Sulfate [mM]
PS81/280-1	503	0.99
PS81/280-1	518	1.17
PS81/280-1	538	1.03
PS81/280-1	558	1.06
PS81/280-1	578	1.52
PS81/280-1	598	1.54
PS81/280-1	618	1.03
PS81/280-1	638	1.08
PS81/280-1	658	0.99
PS81/280-1	678	1.07
PS81/280-1	698	1.16
PS81/280-1	718	1.12
PS81/280-1	738	1.13
PS81/280-1	758	1.30
PS81/280-1	778	0.84
PS81/280-1	798	1.07
PS81/280-1	818	0.91
PS81/280-1	838	0.96
PS81/280-1	858	1.11
PS81/280-1	878	0.97
PS81/280-1	898	0.83

Table S1. Methane, sulfate and DIC concentrations in pore water. PART III-A

Station	Depth [cm]	Sulfate [mM]	Depth [m]	CH_4 [mM]	Depth [cm]	DIC [mM]
PS81/281-2	20	20.20	64	0.326	20	8.08
PS81/281-2	20	20.27	164	14.346	60	24.17
PS81/281-2	40	13.57	264	14.574	100	19.89
PS81/281-2	60	5.48	364	10.059	140	28.58
PS81/281-2	80	0.57	464	2.846	180	28.25
PS81/281-2	100	0.43	564	4.741	240	28.48
PS81/281-2	120	0.51	664	2.796	300	26.65
PS81/281-2	140	0.61	764	4.025	360	27.74
PS81/281-2	160	0.09	864	2.763	440	25.47
PS81/281-2	180	0.29			520	24.08
PS81/281-2	200	0.07			620	24.37
PS81/281-2	220	0.44			820	20.68
PS81/281-2	240	0.00				
PS81/281-2	260	0.10				
PS81/281-2	280	0.01				

Table S1. Methane, sulfate and DIC concentrations in pore water. PART III-B

Station	Depth [cm]	Sulfate [mM]
PS81/281-2	300	0.01
PS81/281-2	320	0.00
PS81/281-2	340	0.03
PS81/281-2	360	0.00
PS81/281-2	380	0.00
PS81/281-2	400	0.00
PS81/281-2	420	0.00
PS81/281-2	440	0.02
PS81/281-2	460	0.03
PS81/281-2	480	0.00
PS81/281-2	500	0.03
PS81/281-2	520	0.00
PS81/281-2	540	0.02
PS81/281-2	560	0.00
PS81/281-2	580	0.00
PS81/281-2	600	0.00
PS81/281-2	620	0.00
PS81/281-2	640	0.00
PS81/281-2	660	0.00
PS81/281-2	680	0.00
PS81/281-2	700	0.00
PS81/281-2	720	0.00
PS81/281-2	740	0.00
PS81/281-2	760	0.00
PS81/281-2	780	0.02
PS81/281-2	800	0.00
PS81/281-2	820	0.00
PS81/281-2	840	0.00

Table S2. Methane concentrations in the water column

CTD-Station	Depth [mbsl]	CH_4 [nM]
PS81/281-1	10	5.5
PS81/281-1	20	3.4
PS81/281-1	75	2.9
PS81/281-1	115	5.1
PS81/281-1	140	4.0
PS81/281-1	160	4.8
PS81/281-1	180	5.2
PS81/281-1	200	10.7
PS81/281-1	215	14.1
PS81/281-1	225	15.0
PS81/281-1	233	25.4
PS81/281-1	239	23.8
PS81/281-1	244	24.2
PS81/281-1	247	17.3
PS81/281-1	249	22.2
PS81/282-1	10	3.8
PS81/282-1	20	4.0
PS81/282-1	50	8.5
PS81/282-1	75	5.5
PS81/282-1	85	6.3
PS81/282-1	90	4.8
PS81/282-1	95	6.7

CTD-Station	Depth [mbsl]	CH_4 [nM]
PS81/284-3	10	5.0
PS81/284-3	100	3.8
PS81/284-3	140	4.4
PS81/284-3	160	8.2
PS81/284-3	180	10.8
PS81/284-3	200	27.8
PS81/284-3	225	41.4
PS81/284-3	235	42.9
PS81/284-3	245	50.9
PS81/284-3	250	57.7
PS81/284-3	254	55.6
PS81/286-1	10	3.9
PS81/286-1	50	2.9
PS81/286-1	100	4.0
PS81/286-1	140	3.8
PS81/286-1	160	4.6
PS81/286-1	200	4.5
PS81/286-1	210	9.5
PS81/286-1	230	5.2
PS81/286-1	250	3.6
PS81/286-1	263	4.6

APPENDIX CHAPTER 3: CASE STUDY 2: SEEPAGE IN THE MEDITERRANEAN

"Methane in the water column above an active mud volcano in the Calabrian margin"

- Table S1

Table S1. Methane concentrations in the water column. PART I

Station	CTD	Niskin	Water depth	CH4 [nM]
GeoB 19204	CTD-1	1	1554	1754.1
GeoB 19204	CTD-1	2	1543	1031.3
GeoB 19204	CTD-1	3	1533	369.8
GeoB 19204	CTD-1	4	1513	43.7
GeoB 19204	CTD-1	5	1463	12.5
GeoB 19204	CTD-1	6	1361	3.5
GeoB 19204	CTD-1	7	1262	2.2
GeoB 19204	CTD-1	8	1163	2.1
GeoB 19204	CTD-1	9	1063	3.2
GeoB 19210	CTD-3	1	1562	13.2
GeoB 19210	CTD-3	2	1561	14.7
GeoB 19210	CTD-3	3	1559	15.8
GeoB 19210	CTD-3	4	1556	18.2
GeoB 19210	CTD-3	5	1556	16.3
GeoB 19210	CTD-3	6	1551	17.5
GeoB 19210	CTD-3	8	1536	6.2
GeoB 19210	CTD-3	9	1526	267.0
GeoB 19210	CTD-3	10	1506	13.0
GeoB 19210	CTD-3	11	1486	11.8
GeoB 19210	CTD-3	12	1466	20.2
GeoB 19210	CTD-3	13	1446	7.8
GeoB 19210	CTD-3	14	1426	1.9
GeoB 19210	CTD-3	15	1366	1.8

Table S1. Methane concentrations in the water column. PART II

Station	CTD	Niskin	Water depth	CH4 [nM]
GeoB 19216	CTD-5	1	1540	17.8
GeoB 19216	CTD-5	2	1531	3.8
GeoB 19216	CTD-5	3	1522	3.6
GeoB 19216	CTD-5	4	1515	3.2
GeoB 19216	CTD-5	5	1515	3.9
GeoB 19216	CTD-5	6	1495	3.0
GeoB 19216	CTD-5	7	1475	2.2
GeoB 19216	CTD-5	8	1552	658.1
GeoB 19216	CTD-5	9	1542	9714.6
GeoB 19216	CTD-5	10	1532	2485.2
GeoB 19216	CTD-5	11	1522	789.0
GeoB 19216	CTD-5	12	1512	193.0
GeoB 19216	CTD-5	14	1482	614.9
GeoB 19216	CTD-5	15	1552	2923.9
GeoB 19216	CTD-5	16	1542	18.6
GeoB 19216	CTD-5	17	1531	8.9
GeoB 19216	CTD-5	18	1521	6.1
GeoB 19216	CTD-5	19	1510	6.5
GeoB 19216	CTD-5	20	1500	5.2
GeoB 19216	CTD-5	21	1480	9.5
GeoB 19220	CTD-6	2	1582	50.4
GeoB 19220	CTD-6	3	1582	43.0
GeoB 19220	CTD-6	4	1572	42.2
GeoB 19220	CTD-6	5	1562	35.0
GeoB 19220	CTD-6	6	1552	23.7
GeoB 19220	CTD-6	7	1542	23.6
GeoB 19220	CTD-6	8	1532	62.4
GeoB 19220	CTD-6	9	1522	37.7
GeoB 19220	CTD-6	10	1512	7.4
GeoB 19220	CTD-6	11	1502	3.5
GeoB 19220	CTD-6	12	1492	2.8
GeoB 19220	CTD-6	13	1482	2.0
GeoB 19220	CTD-6	14	1472	2.2
GeoB 19220	CTD-6	15	1452	2.0
GeoB 19220	CTD-6	16	1432	2.7
GeoB 19220	CTD-6	17	1412	2.3
GeoB 19220	CTD-6	18	1392	4.7

Table S1. Methane concentrations in the water column. PART III

Station	CTD	Niskin	Water depth	CH4 [nM]
GeoB 19223	CTD-7	1	1550	102.8
GeoB 19223	CTD-7	2	1540	251.9
GeoB 19223	CTD-7	3	1530	39.4
GeoB 19223	CTD-7	4	1520	0.9
GeoB 19223	CTD-7	5	1510	2.8
GeoB 19223	CTD-7	6	1500	30.2
GeoB 19223	CTD-7	7	1480	58.6
GeoB 19223	CTD-7	8	1552	64.4
GeoB 19223	CTD-7	9	1542	58.9
GeoB 19223	CTD-7	10	1532	44.3
GeoB 19223	CTD-7	11	1522	26.7
GeoB 19223	CTD-7	12	1512	24.3
GeoB 19223	CTD-7	13	1502	18.3
GeoB 19223	CTD-7	14	1482	16.7
GeoB 19223	CTD-7	18	1552	18.7
GeoB 19223	CTD-7	19	1542	12.2
GeoB 19223	CTD-7	20	1532	8.1
GeoB 19223	CTD-7	21	1522	7.1
GeoB 19223	CTD-7	23	1512	8.6
GeoB 19223	CTD-7	25	1502	8.2
GeoB 19223	CTD-7	28	1482	4.2
GeoB 19231-1	CTD-9	1	1503	2.3
GeoB 19231-1	CTD-9	2	1498	2.0
GeoB 19231-1	CTD-9	3	1493	1.5
GeoB 19231-1	CTD-9	4	1488	1.5
GeoB 19231-1	CTD-9	5	1483	1.4
GeoB 19231-1	CTD-9	6	1478	1.4
GeoB 19231-1	CTD-9	7	1473	1.9
GeoB 19231-1	CTD-9	8	1468	2.3
GeoB 19231-1	CTD-9	9	1463	2.4
GeoB 19231-1	CTD-9	10	1458	2.3
GeoB 19231-1	CTD-9	11	1453	2.1
GeoB 19231-1	CTD-9	12	1448	2.2
GeoB 19231-1	CTD-9	13	1443	2.1
GeoB 19231-1	CTD-9	14	1438	2.2
GeoB 19231-1	CTD-9	18	1433	2.2
GeoB 19231-1	CTD-9	19	1428	2.0
GeoB 19231-1	CTD-9	20	1423	2.0
GeoB 19231-1	CTD-9	21	1418	1.7
GeoB 19231-1	CTD-9	23	1408	1.6
GeoB 19231-1	CTD-9	25	1398	1.5
GeoB 19231-1	CTD-9	28	1388	1.7

Table S1. Methane concentrations in the water column. PART IV

Station	CTD	Niskin	Water depth	CH4 [nM]
GeoB 19233-1	CTD-10	1	1503	3.7
GeoB 19233-1	CTD-10	2	1498	3.0
GeoB 19233-1	CTD-10	3	1493	2.1
GeoB 19233-1	CTD-10	4	1488	2.1
GeoB 19233-1	CTD-10	6	1473	1.9
GeoB 19233-1	CTD-10	7	1463	2.0
GeoB 19233-1	CTD-10	8	1508	9.6
GeoB 19233-1	CTD-10	9	1503	8.3
GeoB 19233-1	CTD-10	10	1498	6.1
GeoB 19233-1	CTD-10	11	1493	3.4
GeoB 19233-1	CTD-10	12	1488	3.8
GeoB 19233-1	CTD-10	13	1483	2.7
GeoB 19233-1	CTD-10	14	1473	2.5
GeoB 19233-1	CTD-10	18	1511	8.3
GeoB 19233-1	CTD-10	19	1506	6.0
GeoB 19233-1	CTD-10	20	1501	3.9
GeoB 19233-1	CTD-10	21	1496	3.6
GeoB 19233-1	CTD-10	23	1491	2.2
GeoB 19233-1	CTD-10	25	1486	2.0
GeoB 19233-1	CTD-10	28	1476	1.9
GeoB 19239-1	CTD-11	1	1598	32.4
GeoB 19239-1	CTD-11	2	1593	33.1
GeoB 19239-1	CTD-11	3	1588	24.6
GeoB 19239-1	CTD-11	4	1583	29.6
GeoB 19239-1	CTD-11	5	1578	10.4
GeoB 19239-1	CTD-11	6	1568	3.6
GeoB 19239-1	CTD-11	7	1558	3.1
GeoB 19239-1	CTD-11	8	1598	3.0
GeoB 19239-1	CTD-11	9	1593	26.6
GeoB 19239-1	CTD-11	11	1583	16.9
GeoB 19239-1	CTD-11	12	1578	10.6
GeoB 19239-1	CTD-11	13	1568	4.2
GeoB 19239-1	CTD-11	14	1558	2.9
GeoB 19239-1	CTD-11	18	1598	331.0
GeoB 19239-1	CTD-11	19	1593	248.4
GeoB 19239-1	CTD-11	20	1588	206.3
GeoB 19239-1	CTD-11	21	1583	45.5
GeoB 19239-1	CTD-11	23	1578	22.4
GeoB 19239-1	CTD-11	25	1568	7.7
GeoB 19239-1	CTD-11	28	1558	62.4

Table S1. Methane concentrations in the water column. PART V

Station	CTD	Niskin	Water depth	CH4 [nM]
GeoB 19241-1	CTD-12	1	1598	54.8
GeoB 19241-1	CTD-12	2	1593	60.6
GeoB 19241-1	CTD-12	3	1588	55.8
GeoB 19241-1	CTD-12	4	1583	43.9
GeoB 19241-1	CTD-12	5	1573	23.2
GeoB 19241-1	CTD-12	6	1563	13.0
GeoB 19241-1	CTD-12	7	1553	9.9
GeoB 19241-1	CTD-12	8	1598	44.4
GeoB 19241-1	CTD-12	9	1593	42.6
GeoB 19241-1	CTD-12	10	1588	36.8
GeoB 19241-1	CTD-12	11	1583	24.6
GeoB 19241-1	CTD-12	12	1573	19.6
GeoB 19241-1	CTD-12	13	1563	12.9
GeoB 19241-1	CTD-12	14	1553	12.3
GeoB 19241-1	CTD-12	18	1598	44.3
GeoB 19241-1	CTD-12	19	1593	42.5
GeoB 19241-1	CTD-12	20	1588	40.7
GeoB 19241-1	CTD-12	21	1583	38.2
GeoB 19241-1	CTD-12	23	1573	28.8
GeoB 19241-1	CTD-12	25	1563	13.8
GeoB 19241-1	CTD-12	28	1553	19.3
GeoB 19247-1	CTD-13	1	1597	23.0
GeoB 19247-1	CTD-13	2	1592	19.7
GeoB 19247-1	CTD-13	3	1587	8.5
GeoB 19247-1	CTD-13	4	1583	4.5
GeoB 19247-1	CTD-13	5	1572	5.4
GeoB 19247-1	CTD-13	6	1562	12.4
GeoB 19247-1	CTD-13	7	1552	14.3
GeoB 19247-1	CTD-13	8	1532	2.2
GeoB 19247-1	CTD-13	9	1512	5.0
GeoB 19247-1	CTD-13	10	1492	3.6
GeoB 19247-1	CTD-13	11	1452	3.7
GeoB 19247-1	CTD-13	12	1595	82.1
GeoB 19247-1	CTD-13	13	1591	19.6
GeoB 19247-1	CTD-13	14	1586	14.6
GeoB 19247-1	CTD-13	18	1581	10.0
GeoB 19247-1	CTD-13	19	1571	4.9
GeoB 19247-1	CTD-13	20	1561	16.8
GeoB 19247-1	CTD-13	21	1551	15.7
GeoB 19247-1	CTD-13	23	1531	8.4
GeoB 19247-1	CTD-13	25	1511	3.0
GeoB 19247-1	CTD-13	28	1491	4.4

Table S1. Methane concentrations in the water column. PART VI

Station	CTD	Niskin	Water depth	CH4 [nM]
GeoB 19250-1	CTD-14	1	1494	12.2
GeoB 19250-1	CTD-14	2	1492	1.8
GeoB 19250-1	CTD-14	3	1490	1.7
GeoB 19250-1	CTD-14	4	1493	1.7
GeoB 19250-1	CTD-14	5	1491	1.8
GeoB 19250-1	CTD-14	6	1489	1.6
GeoB 19250-1	CTD-14	7	1493	1.7
GeoB 19250-1	CTD-14	8	1491	1.7
GeoB 19250-1	CTD-14	9	1489	1.5
GeoB 19250-1	CTD-14	10	1493	1.6
GeoB 19250-1	CTD-14	11	1491	1.6
GeoB 19250-1	CTD-14	12	1489	23.4
GeoB 19250-1	CTD-14	13	1494	1.8
GeoB 19250-1	CTD-14	14	1491	1.8
GeoB 19250-1	CTD-14	18	1489	1.6
GeoB 19250-1	CTD-14	19	1495	1.9
GeoB 19250-1	CTD-14	20	1493	1.8
GeoB 19250-1	CTD-14	21	1491	1.8
GeoB 19250-1	CTD-14	23	1496	1.8
GeoB 19250-1	CTD-14	25	1494	1.9
GeoB 19250-1	CTD-14	28	1491	1.7
GeoB 19256-1	CTD-15	1	1590	27.5
GeoB 19256-1	CTD-15	2	1585	13.1
GeoB 19256-1	CTD-15	3	1580	17.9
GeoB 19256-1	CTD-15	4	1575	15.3
GeoB 19256-1	CTD-15	5	1565	4.9
GeoB 19256-1	CTD-15	6	1555	3.4
GeoB 19256-1	CTD-15	7	1545	2.1
GeoB 19256-1	CTD-15	8	1587	6.6
GeoB 19256-1	CTD-15	9	1582	8.8
GeoB 19256-1	CTD-15	10	1577	6.5
GeoB 19256-1	CTD-15	11	1572	4.1
GeoB 19256-1	CTD-15	12	1562	2.5
GeoB 19256-1	CTD-15	13	1552	2.0
GeoB 19256-1	CTD-15	14	1542	2.6
GeoB 19256-1	CTD-15	18	1588	33.5
GeoB 19256-1	CTD-15	19	1583	24.2
GeoB 19256-1	CTD-15	20	1578	9.7
GeoB 19256-1	CTD-15	21	1573	4.4
GeoB 19256-1	CTD-15	23	1563	3.3
GeoB 19256-1	CTD-15	25	1553	3.1
GeoB 19256-1	CTD-15	28	1543	3.7

Table S1. Methane concentrations in the water column. PART VII

Station	CTD	Niskin	Water depth	CH4 [nM]
GeoB 19262-1	CTD-16	1	1523	1.7
GeoB 19262-1	CTD-16	2	1518	1.7
GeoB 19262-1	CTD-16	3	1513	5.7
GeoB 19262-1	CTD-16	4	1508	1.6
GeoB 19262-1	CTD-16	5	1498	8.9
GeoB 19262-1	CTD-16	6	1488	8.2
GeoB 19262-1	CTD-16	7	1478	1.3
GeoB 19262-1	CTD-16	8	1458	1.3
GeoB 19262-1	CTD-16	9	1438	1.7
GeoB 19262-1	CTD-16	10	1418	1.6
GeoB 19262-1	CTD-16	11	1560	1.5
GeoB 19262-1	CTD-16	12	1555	2.0
GeoB 19262-1	CTD-16	13	1550	1.7
GeoB 19262-1	CTD-16	14	1545	2.0
GeoB 19262-1	CTD-16	18	1535	2.0
GeoB 19262-1	CTD-16	19	1525	1.6
GeoB 19262-1	CTD-16	20	1515	2.0
GeoB 19262-1	CTD-16	21	1505	1.7
GeoB 19262-1	CTD-16	23	1485	1.8
GeoB 19262-1	CTD-16	25	1465	1.6
GeoB 19262-1	CTD-16	28	1445	1.6
GeoB 19265-1	CTD-17	1	1601	125.1
GeoB 19265-1	CTD-17	2	1596	125.7
GeoB 19265-1	CTD-17	3	1591	171.6
GeoB 19265-1	CTD-17	4	1586	125.4
GeoB 19265-1	CTD-17	5	1576	83.7
GeoB 19265-1	CTD-17	6	1566	41.7
GeoB 19265-1	CTD-17	7	1556	9.6
GeoB 19265-1	CTD-17	8	1546	3.0
GeoB 19265-1	CTD-17	9	1526	1.9
GeoB 19265-1	CTD-17	10	1506	1.8
GeoB 19265-1	CTD-17	11	1486	4.1
GeoB 19265-1	CTD-17	12	1599	88.9
GeoB 19265-1	CTD-17	13	1594	81.5
GeoB 19265-1	CTD-17	14	1589	74.4
GeoB 19265-1	CTD-17	18	1584	85.5
GeoB 19265-1	CTD-17	20	1564	9.2
GeoB 19265-1	CTD-17	21	1554	17.1
GeoB 19265-1	CTD-17	23	1534	8.6
GeoB 19265-1	CTD-17	25	1514	2.6
GeoB 19265-1	CTD-17	28	1494	1.7

Table S1. Methane concentrations in the water column. PART VIII

Station	CTD	Niskin	Water depth	CH4 [nM]
GeoB 19271-1	CTD-18	1	1598	3.9
GeoB 19271-1	CTD-18	2	1593	4.7
GeoB 19271-1	CTD-18	3	1588	5.3
GeoB 19271-1	CTD-18	4	1583	9.5
GeoB 19271-1	CTD-18	5	1573	7.0
GeoB 19271-1	CTD-18	6	1563	6.1
GeoB 19271-1	CTD-18	7	1553	5.0
GeoB 19271-1	CTD-18	8	1543	4.2
GeoB 19271-1	CTD-18	9	1523	4.9
GeoB 19271-1	CTD-18	10	1503	4.2
GeoB 19271-1	CTD-18	11	1483	4.0
GeoB 19271-1	CTD-18	12	1597	5.1
GeoB 19271-1	CTD-18	13	1592	5.1
GeoB 19271-1	CTD-18	14	1587	5.4
GeoB 19271-1	CTD-18	18	1582	6.7
GeoB 19271-1	CTD-18	19	1572	5.5
GeoB 19271-1	CTD-18	20	1562	2.4
GeoB 19271-1	CTD-18	21	1552	2.8
GeoB 19271-1	CTD-18	23	1542	2.0
GeoB 19271-1	CTD-18	25	1522	2.0
GeoB 19271-1	CTD-18	28	1502	2.0
GeoB 19281-1	CTD-23	1	1561	2.3
GeoB 19281-1	CTD-23	2	1555	2.3
GeoB 19281-1	CTD-23	3	1550	2.5
GeoB 19281-1	CTD-23	4	1545	3.2
GeoB 19281-1	CTD-23	5	1535	3.4
GeoB 19281-1	CTD-23	6	1525	3.5
GeoB 19281-1	CTD-23	7	1515	2.7
GeoB 19281-1	CTD-23	8	1505	2.8
GeoB 19281-1	CTD-23	9	1485	2.6
GeoB 19281-1	CTD-23	10	1465	2.2
GeoB 19281-1	CTD-23	11	1445	1.7
GeoB 19281-1	CTD-23	12	1554	2.3
GeoB 19281-1	CTD-23	13	1548	2.5
GeoB 19281-1	CTD-23	14	1543	2.4
GeoB 19281-1	CTD-23	18	1538	2.2
GeoB 19281-1	CTD-23	19	1528	2.3
GeoB 19281-1	CTD-23	20	1518	2.7
GeoB 19281-1	CTD-23	21	1508	2.6
GeoB 19281-1	CTD-23	23	1488	2.3
GeoB 19281-1	CTD-23	25	1468	2.1
GeoB 19281-1	CTD-23	28	1447	1.9

Table S1. Methane concentrations in the water column. PART IX

Station	CTD	Niskin	Water depth	CH4 [nM]
GeoB 19288-1	CTD-24	1	1635	27.3
GeoB 19288-1	CTD-24	2	1630	24.9
GeoB 19288-1	CTD-24	3	1624	27.4
GeoB 19288-1	CTD-24	4	1620	29.0
GeoB 19288-1	CTD-24	5	1610	49.3
GeoB 19288-1	CTD-24	6	1600	31.3
GeoB 19288-1	CTD-24	7	1590	5.9
GeoB 19288-1	CTD-24	8	1580	3.1
GeoB 19288-1	CTD-24	9	1570	14.3
GeoB 19288-1	CTD-24	10	1561	18.1
GeoB 19288-1	CTD-24	11	1551	2.8
GeoB 19288-1	CTD-24	12	1541	1.9
GeoB 19288-1	CTD-24	13	1531	1.8
GeoB 19288-1	CTD-24	14	1521	1.8
GeoB 19288-1	CTD-24	18	1510	1.7
GeoB 19288-1	CTD-24	19	1500	2.5
GeoB 19288-1	CTD-24	20	1490	2.6
GeoB 19288-1	CTD-24	21	1480	5.5
GeoB 19288-1	CTD-24	23	1470	2.7
GeoB 19288-1	CTD-24	25	1460	1.9
GeoB 19288-1	CTD-24	28	1440	1.9